Università degli studi di Firenze
Dipartimento di Fisica

Dottorato di ricerca in Fisica - XVII Ciclo

Search for new physics in events with high-p_t leptons at HERA

Tesi di Dottorato di Ricerca in Fisica di
Chiara Genta

Supervisore: Dott. Giuseppe Barbagli

Coordinatore: Prof. Alessandro Cuccoli

Firenze, 31 Gennaio 2005

Contents

List of Figures

List of Tables

Acknowledgements

The results achieved in this thesis have been made possible thanks to the efforts of the ZEUS collaboration and of the HERA machine group.

I would like to thank Giuseppe Barbagli for his continuous support during these years. I am also especially grateful to Elisabetta Gallo for sharing with me her physical knowledge and experience, and for helping and encouraging me during my work. I am very thankful to Lorenzo Bellagamba for the teamwork and for the precious physics discussions and suggestions. I would like to thank Katarzyna Klimek, Alex Tapper and Enrico Tassi for their enthusiastic coordination of the High-Q^2 group, and Alessia Bruni for her advices and collaboration on the multi-muon analysis. I also acknowledge the EOTW team for the heroic efforts in the visual scan of the events.

I am grateful to the ZeVis team, especially to Rainer Mankel and Oliver Gutsche, for introducing me to the inner structure of ZeVis. I would like to thank Pawel Luzniak and Yuji Yamazaki for providing me with the technical details of the BAC detector and the ZEUS trigger.

I would like also to thank all my DESY friends, especially Alessandro Montanari, Ada Solano, Amita Raval, Davide Boscherini, Massimo Corradi, Alessandro Polini, Andrea Longhin, Monica Turcato.

My special thanks to my family which encouraged me during my studies and to Luigi for his patience and continuous support in the last (almost) seven years.

Introduction

Since ancient times the philosophers tried to simplify and derive the multiplicity of phenomena of the world from few principles. This strong human wish is still present in modern physics in which a lot of effort has been made to reduce all the forces of nature to few fundamental interactions and the matter to few elementary constituents. Nowadays two kinds of elementary particles – quarks and leptons – and four kinds of fundamental forces – gravity, electromagnetic, weak and strong forces – are known. The Standard Model (SM) successfully describes the behavior of the last three interactions. Each force is mediated by a gauge boson; the carrier of the electromagnetic interactions is the photon, γ, the quanta of the weak forces are the Z^0 and the $W^{\pm}$ bosons, and the carriers of the strong force are the gluons, g. However the Standard Model is not a complete theory since it still leaves many questions open:

- there is no theoretical explanation for the existence of three families of leptons and quarks;
- the mass spectrum of the known particles is not calculable within the SM but it has to be determined experimentally;
- the existence of the Higgs boson, introduced to explain the mass of the particles, has not yet been experimentally proved; moreover, the gap between the energy scale of the SM particles and the Planck mass (hierarchy problem) leads to corrections to the mass of the Higgs larger than the Higgs mass itself;
- gravity is not included in the SM.

Moreover, astrophysical observations suggest that most of the matter in the universe is not constituted by SM particles (dark matter). More recent observations have outlined the existence of a uniformly distributed energy (dark energy), whose origin has not been yet established. For these reasons new theories which can solve, at least partially, the SM problems have been proposed.

The H1 and ZEUS experiments at the HERA collider performed several searches for new particles and for new interactions. The analyses on data collected during

the first phase of data taking, HERA I, are completed in almost all sectors of new physics searches. Although data and Standard Model predictions generally agree, several discrepancies were found at HERA I in events with one or more high-momentum isolated leptons in the final state [1, 2, 3].

In this thesis work an analysis on events with high-momentum muons and τ leptons in the final state has been performed. The search focused on interactions that violate lepton flavor. All ZEUS data taken during the years 1994–2000, corresponding to the whole HERA I statistics, have been analyzed and no evidence of lepton-flavor violation (LFV) was found. A leptoquark model was used to set limits on LFV interactions. The obtained limits resulted competitive and, especially for $e - \tau$ transitions, better with respect to limits from other experiments.

An analysis on events with two or more isolated muons in the final state with high invariant mass has been also performed. The analysis and its results are shown in Appendix A.

In the last years I have been the responsible of the data quality monitor for the high-Q^2 physics group and I have been involved in the development of the new ZEUS event display, ZeVis.

This thesis is organized as follows. The first chapter gives a theoretical overview of the physics of ep collisions. The processes which are relevant for the analysis are then described, focusing on the events with high-momentum isolated leptons. In the last part an overview of LFV which would produce events with isolated leptons in the final state is given. The second chapter describes the HERA collider and the ZEUS detector. In the third chapter a general description of the Monte Carlo generators used to simulate the SM background and the LFV signal is given. Chapter 4 describes how the variables used in the analysis are reconstructed. The search for lepton-flavor-violating interactions in $e - \mu$ and $e - \tau$ transitions is described in chapters 5 and 6. In the seventh chapter the results of the analysis, the limit setting procedure and the comparison of the limits with other experiment constraints are described. In the chapter 8 an overview of the HERA and ZEUS upgrade is given. The implementation of a component of the detector in the new ZEUS event display and the data quality monitor for the high-Q^2 group are then summarized. In the last chapter the conclusions are drawn.

Chapter 1

Theoretical overview

The first section of this chapter contains a brief introduction to lepton-nucleon interactions, with a particular emphasis on *ep* collisions at HERA. The last two sections focus on events with high transverse momentum leptons which are the main topic of this thesis. Standard Model processes that produce high transverse momentum leptons in the final state will be described. In the last years several discrepancies between HERA data and Standard Model predictions were found in events with high transverse momentum leptons. The results will be briefly described. Several theories beyond Standard Model predict processes with high-momentum leptons in the final state. This chapter will concentrate on theories which predict lepton-flavor violation.

1.1 Lepton-nucleon interactions

In the Standard Model (SM) lepton-nucleon interactions proceed through the exchange of an electroweak vector boson (γ, Z^0, $W^{\pm}$). Neutrinos, due to their neutral charge, can only exchange a Z^0 or $W^{\pm}$ bosons. Processes involving γ or Z^0 bosons are called neutral current (NC), see Fig. 1.1(a): in this case the lepton is left unchanged by the interaction. Charged current (CC) interactions, mediated by a $W^{\pm}$, convert an electron into a neutrino and *vice-versa* as it can be seen in Fig. 1.1(b), where the interaction between an electron and a proton is schematically shown. The point-like nature of the leptons and the fact that electroweak interactions are well understood makes the lepton-nucleon scattering a powerful tool to study the nucleon structure. It was an experiment at SLAC in the '60s that uncontroversially established the point-like partonic substructure of the nucleon [4]. That experiment measured the spectrum of electrons scattered off a nucleon target. Since then a lot of progress has been made in understanding the proton structure. The electron-proton collider HERA, with an energy of $\sim 320\,\text{GeV}$ available in the center of mass,

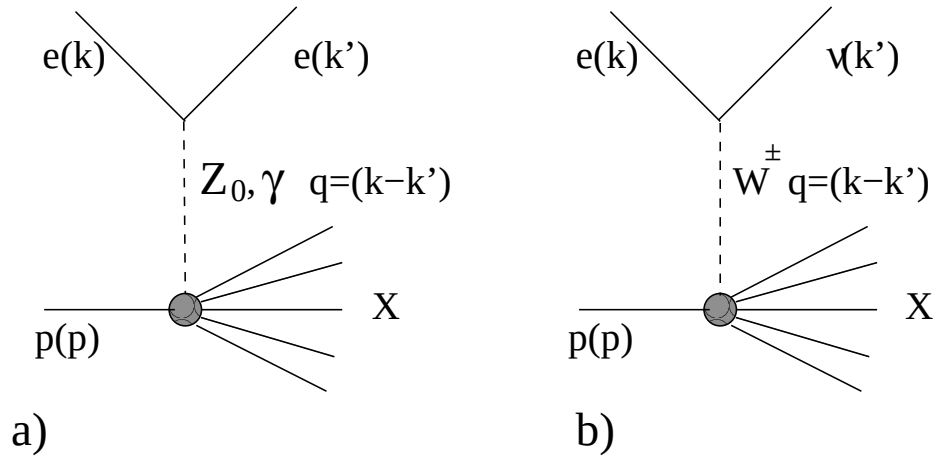

Figure 1.1: Deep inelastic electron- (or positron-) proton scattering: (a) neutral current process; (b) charged current process.

extends the accessible kinematic region by several orders of magnitude with respect to previous fixed-target experiments.

In the following the definition of the Lorentz invariants used in lepton-nucleon scattering is given. Denoting with k, k', P the four-momentum of the initial- and final-state lepton, and of the incoming nucleon, respectively, the kinematic variables Q^2, x and y are defined as:

$$\begin{aligned} Q^2 &= -q^2 = -(k-k')^2, \\ x &= \frac{Q^2}{2P\cdot q}, \\ y &= \frac{P\cdot q}{P\cdot k}. \end{aligned} \tag{1.1}$$

If the nucleon mass is negligible with respect to its momentum, as for example at HERA, these three invariants obey to the following relation:

$$Q^2 = xys. \tag{1.2}$$

The Q^2 variable represents the negative four-momentum squared transferred at the interaction vertex, while y quantifies the inelasticity of the process and $0 < y < 1$ by definition. The last two statements can be easily understood in the proton rest frame, where $y = 1 - \frac{E'}{E}$, with E and E' being the energy of the initial- and final-state electron, respectively. Another useful variable is the invariant mass of the virtual-boson proton system:

$$W^2 = (P+q)^2 = m^2 - Q^2 + 2P\cdot q, \tag{1.3}$$

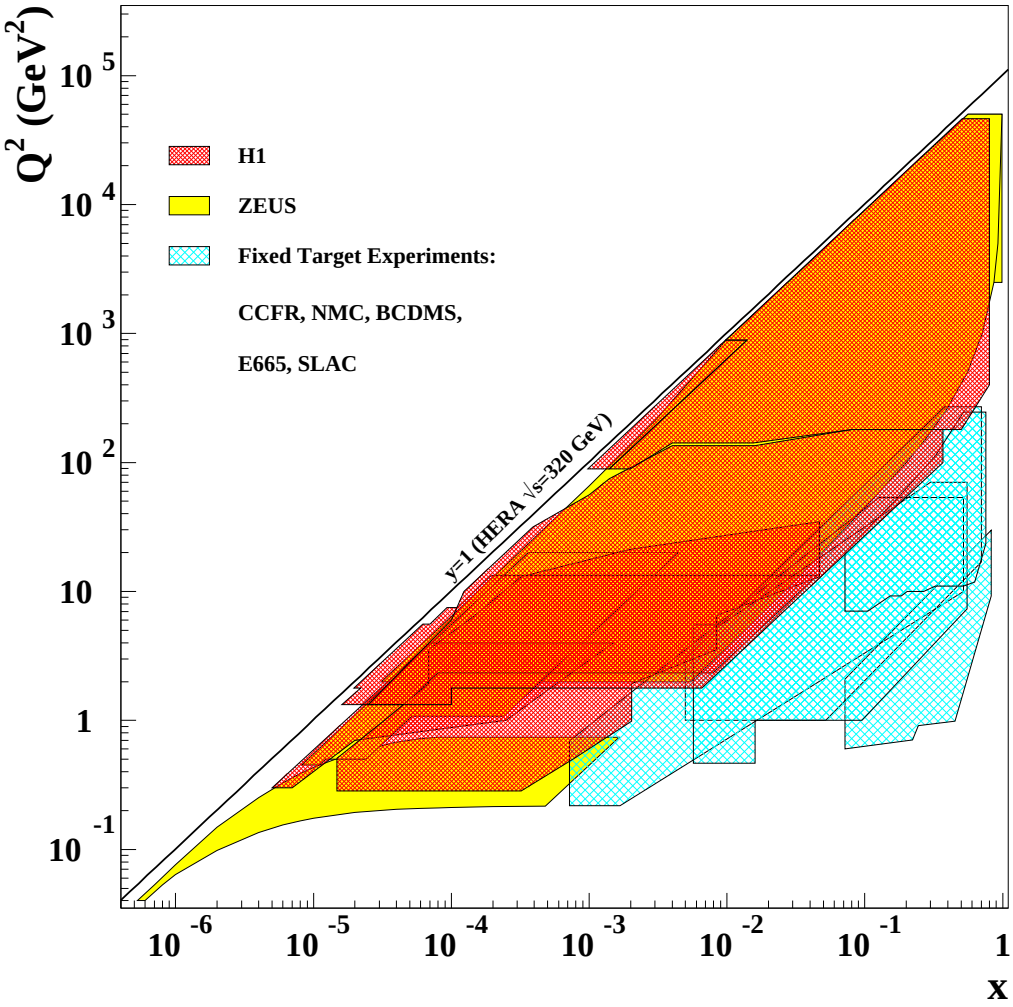

Figure 1.2: The HERA kinematic available $x - Q^2$ plane, as compared to fixed-target experiments.

where m is the nucleon mass. Therefore x, called the Bjorken variable, can be re-written using W:

$$x = \frac{Q^2}{W^2 - m^2 + Q^2}. \tag{1.4}$$

Since necessarily $W^2 \geq m^2$, it follows that $0 < x < 1$. In Fig. 1.2 the HERA kinematic available $x - Q^2$ plane as compared to fixed-target experiments is shown. The ranges covered by HERA span almost six orders of magnitudes in x, from 10^{-6} to ~ 1, and in Q^2 from $10^{-1}\,\mathrm{GeV}^2$ to more then $10^4\,\mathrm{GeV}^2$.

1.1.1 The parton model and the scale invariance

The parton model was introduced [5, 6] to explain the total cross section for the scattering of electrons or neutrinos on a proton target. In this model the measured cross section is interpreted as a sum of incoherent interactions between the electron or neutrino and the proton constituents. The nucleon constituents are assumed massless, point-like and non interacting. These assumptions can be justified with the fact that, in the nucleon "infinite momentum" frame ($P \gg m$), the interaction time between the electron or the neutrino and the quark can be estimated to be $t_i \sim 2m_q/Q^2$, where m_q is some effective parton mass. The time t_i is much smaller than the parton lifetime, which is $t_q \sim \sqrt{Q^2}/m_q^2$ due to the relativistic time dilatation. Therefore, in the deep inelastic scattering (DIS) at high Q^2 the interaction between partons can be neglected. The partons were later identified with the quarks of the Gell-Mann model [7], introduced to explain the quantum numbers of the observed hadrons. In the quark parton model (QPM) the Bjorken-x defined in Eq. (1.1) coincides with the fraction of the proton momentum z, carried by the quark interacting with the electron. If p' is the four-momentum of the final-state quark:

$$(p')^2 = (zP + q)^2 = 2zP \cdot q - Q^2 = 0, \tag{1.5}$$

where we have neglected the quark mass ($(p')^2 = (zP)^2 = 0$) as dictated by the QPM. From Eq. (1.1) it can be seen that $x \equiv z$.

The double differential ep neutral current cross section, neglecting the Z^0 contribution (this is valid as long as $Q^2 \ll M_{Z^0}^2$), can be written as:

$$\frac{d^2\sigma^{NC}}{dxdQ^2} = \frac{4\pi\alpha^2}{xQ^4}\left(\frac{y^2}{2}2xF_1(x,Q^2) + (1-y)F_2(x,Q^2)\right). \tag{1.6}$$

In the parton model the proton structure functions F_1 and F_2 depend only on the internal structure of the proton and, at fixed x, they do not depend on the scale Q^2. This behavior as a function of the Bjorken-x variable is called "scaling". Expressing the deep inelastic cross section as the sum of the incoherent contributions from the scattering of the electron on point-like quarks of flavor i, and given $q_i(x)$, the probability of finding a quark inside the proton with fraction of proton momentum x, the following relations between F_1 and F_2 and the quark density functions q_i can be derived:

$$\begin{aligned} F_1(x) &= \frac{1}{2}\sum_i c_i^2 q_i(x), \\ F_2(x) &= \sum_i c_i^2 x q_i(x). \end{aligned} \tag{1.7}$$

For low Q^2 and in the QPM the c_i coefficients are equal to the quark charges and the Callan-Gross relation $2xF_1(x) = F_2(x)$ holds.

1.1.2 Scaling violation and QCD evolution of the parton densities

If the nucleons were formed only by non-interacting quarks, the sum over all the parton momenta should be equal to the nucleon momentum. Experimentally it was observed that the sum of the momenta of all the charged particles is about half of the proton momentum. The remaining nucleon momentum must be carried by neutral constituents, the gluons. According to the theory of quantum cromodynamics (QCD), gluons are the massless carriers of the strong force. Perturbative QCD can be successfully applied to the deep inelastic scattering, exploiting the fact that the strong coupling constant, α_s, becomes much weaker at high Q^2:

$$\alpha_s(Q^2) = \frac{12\pi}{(33 - 2n_f)\ln(Q^2/\Lambda^2)}, \tag{1.8}$$

where n_f is the number of quark flavors and Λ an energy cutoff parameter. This behavior, opposite to what happens in quantum electrodynamics (QED), can be explained by the non-abelian nature of the strong force.

QCD was very successful in interpreting the scaling violation observed experimentally. Gluons can emit quark-antiquark couples that have a softer x distribution. For higher Q^2 values it is possible to resolve more details of the proton structure, so that an increase of the quark density functions with Q^2 for low x values is expected, leading to a violation of the scaling. On the other hand when a high-x quark emit a gluon, it decreases its momentum thus causing a depletion of the high-x region whit increasing Q^2. In Fig. 1.3 the measured F_2 is shown as a function of Q^2 for different values of x. The scaling violation is particularly evident at low x.

Unfortunately the parton density functions (PDF) cannot be calculated from first principles, and they have to be determined experimentally. However the factorization theorem [8] states that it is possible to separate the long range effects, which are non-perturbative (such as the PDF), from the hard process which can be treated with perturbative QCD. It is therefore possible, once the parton densities have been determined from a given process, to use them to make predictions for other processes.

The DGLAP equations [9] describe the evolution of the parton densities with the scale Q^2:

$$\frac{\partial}{\partial \ln Q^2}\begin{pmatrix} q \\ g \end{pmatrix} = \frac{\alpha(Q^2)}{2\pi}\begin{bmatrix} P_{qq} & P_{qg} \\ P_{gq} & P_{gg} \end{bmatrix} \otimes \begin{pmatrix} q \\ g \end{pmatrix}, \tag{1.9}$$

where P_{ij} are called splitting functions and represent the probability of finding a parton i inside a parton j with a given fraction of the parton j momentum. By definition:

$$f \otimes h = \int_x^1 \frac{dz}{z} f\left(\frac{x}{z}\right) h(z). \tag{1.10}$$

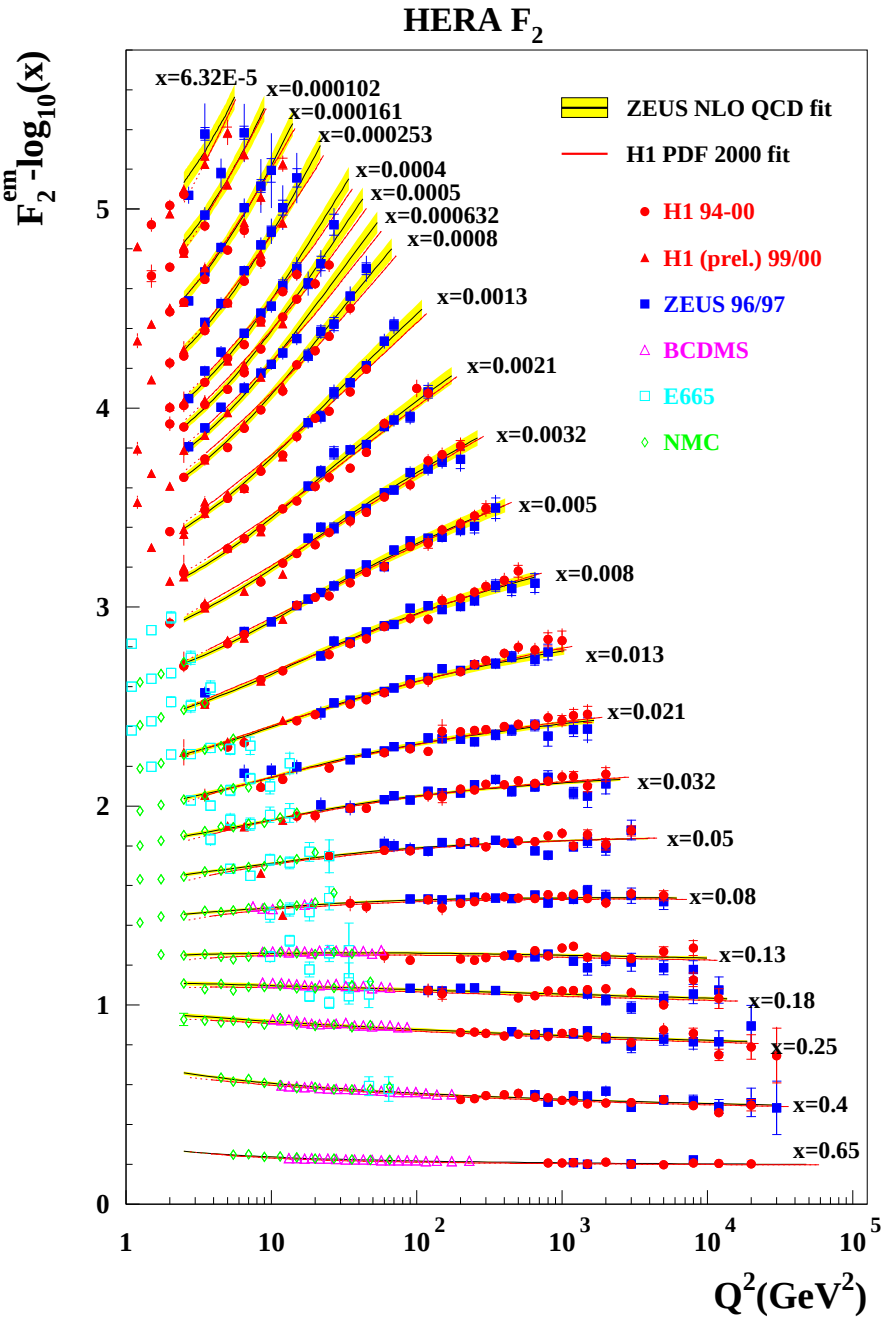

Figure 1.3: The structure function F_2 versus Q^2 at fixed values of x compared to a fit based on DGLAP evolution equation [9]. The violation of the scaling can be observed, especially in the low x region.

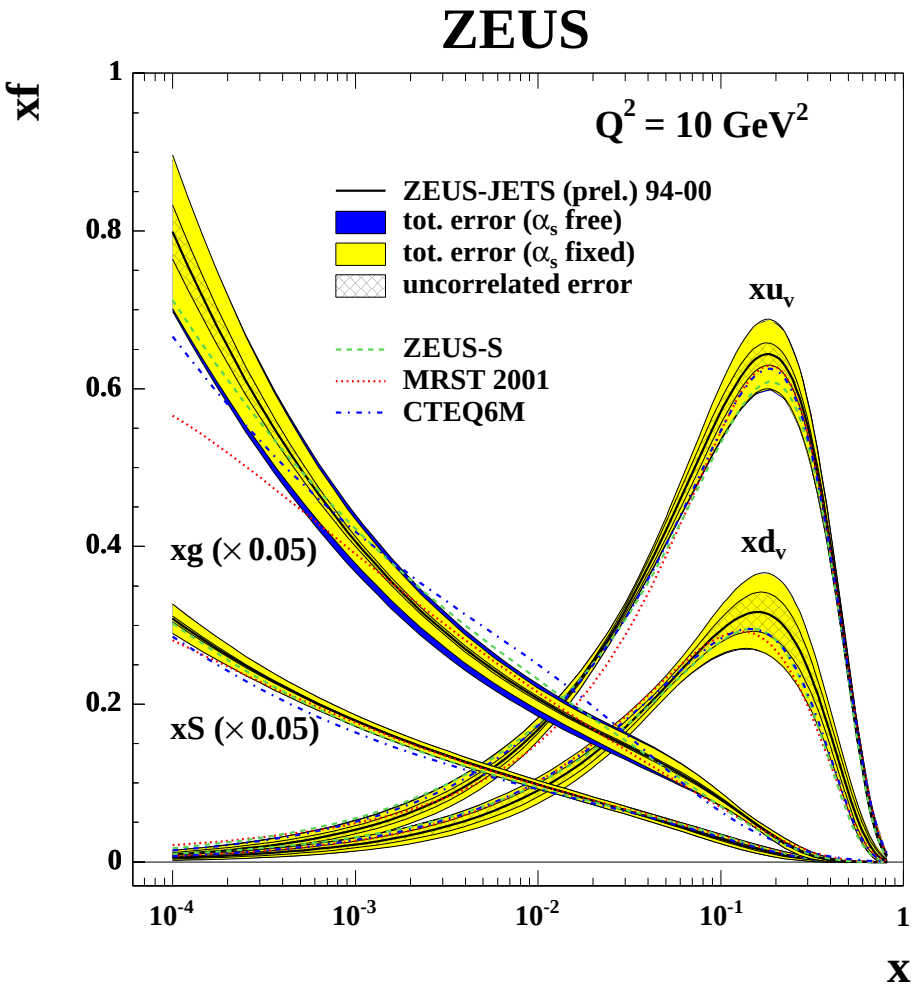

Figure 1.4: The gluon, sea, u and d valence distribution extracted from ZEUS NLO QCD fit [10].

The functions P_{ij} can be expressed by a perturbative expansion:

$$P(\alpha_s, z) = \frac{\alpha_s}{2\pi} P_{ij}^{\mathrm{LO}}(z) + (\frac{\alpha_s}{2\pi})^2 P_{ij}^{\mathrm{NLO}}(z) + ... \tag{1.11}$$

where LO is the leading order and NLO is the next to leading order. Figure 1.4 shows the parton density functions of the proton as obtained from a NLO QCD fit using ZEUS data [10], compared to the sets of parton-density functions determined by the CTEQ6 [11] and MRST [12] groups. As can be seen from the figure, at high x the valence quark, u and d, densities dominate, while the gluon and the sea quark

densities dominate at low x and have a very steeply increasing distribution with decreasing x.

In perturbative QCD the quantity $F_2 - 2xF_1$, called longitudinal structure function, F_L, is different from zero. Spin 1/2 massless quarks absorbing longitudinal polarized photons in head-on collisions would not conserve the helicity, H, or the angular momentum, J, so that in the naïve QPM $F_L = 0$, as expected. On the other hand, if the quark radiates a gluon or a gluon splits into a quark-antiquark pair, both H and J can be conserved and F_L is non-zero. Therefore F_L is sensitive to the gluon content of the proton and it can be used to extract the gluon density.

1.1.3 Deep inelastic scattering cross sections

The double differential NC DIS cross section, including also the Z^0 exchange term, can be written as:

$$\frac{d^2\sigma_{NC}^{e^{\mp}p}}{dxdQ^2} = \frac{2\pi\alpha^2}{xQ^4}\Big(Y_+F_2(x,Q^2) - y^2F_L(x,Q^2) \pm Y_-xF_3(x,Q^2)\Big), \tag{1.12}$$

where $Y_\pm = 1 \pm (1-y)^2$. The structure function xF_3 represents the parity violating term and its effect is to increase the cross section in e^-p scattering and to decrease the cross section in the e^+p case at very high Q^2 for unpolarized electron beam. The contribution of F_L at high Q^2 is negligible. In the general case F_2 and F_3 include the Z^0 contribution and depend on the polarization of the electron beam, $\mathcal{P}$, defined as:

$$\mathcal{P} = \frac{N_L - N_R}{N_L + N_R} \tag{1.13}$$

where N_L and N_R are the number of left-handed and right-handed electron (or positrons), respectively. The structure function F_2 and F_3 can be expressed in in terms of the parton density functions:

$$\begin{aligned} F_2(x,Q^2) &= x\sum_i C_2^{q_i}(Q^2)(q_i(x,Q^2) + \bar{q}_i(x,Q^2)), \\ xF_3(x,Q^2) &= x\sum_i C_3^{q_i}(Q^2)(q_i(x,Q^2) - \bar{q}_i(x,Q^2)). \end{aligned} \tag{1.14}$$

The coefficients C_2 and C_3 depend on Q^2 and can be written in terms of the vector, v_f, and the axial, a_f, couplings, and of the polarization, $\mathcal{P}$:

$$\begin{aligned} C_2^q(Q^2) &= e_q^2 - 2e_qv_q(v_e + \mathcal{P}a_e)\chi_Z + (v_q^2 + a_q^2)(v_e^2 + a_e^2 + 2v_ea_e\mathcal{P})\chi_Z^2, \\ C_3^q(Q^2) &= -2e_qv_q(a_e + \mathcal{P}v_e)\chi_Z + (2v_qa_q)(\mathcal{P}v_e^2 + \mathcal{P}a_e^2 + 2v_ea_e)\chi_Z^2, \end{aligned} \tag{1.15}$$

where e_q is the absolute value of the quark charge in units of positron charge. The vector and axial coupling for a fermion f are given by:

$$\begin{aligned} v_f &= (T_3^f - 2e_f \sin^2\theta_W), \\ a_f &= T_3^f, \end{aligned} \tag{1.16}$$

with θ_W the weak mixing angle, T_3^f the third component of the weak isospin and e_f the electric charge in units of positron charge. The factor χ_Z is given by:

$$\chi_Z = \frac{1}{4\sin^2\theta_W \cos^2\theta_W} \cdot \frac{Q^2}{Q^2 + M_Z^2}, \tag{1.17}$$

where M_Z is the Z^0 mass. As it can be seen from Eqs. (1.15) and (1.17) the effects of the electron polarization are visible only at high Q^2. At low Q^2, since $\chi_Z \to 0$, the parity violating term $C_3^q(Q^2)$ can be neglected and $C_2^q(Q^2) = e_q^2$ as anticipated in Sec. 1.1.1 (Eq. (1.7)).

In the charged current reaction the difference between e^+p and e^-p is more evident since electrons are sensitive to an up-type quark, while positrons are sensitive to a down-type quark (the latter has a lower density in the proton). The double differential CC DIS cross section for e^+p and e^-p collisions can be written in the form:

$$\begin{aligned} \frac{d^2\sigma_{CC}^{e^+p}}{dxdQ^2} = \frac{G_F^2}{4\pi x}\frac{M_W^4}{(Q^2+M_W^2)^2}\Big(&Y_+ x(d(x,Q^2) + s(x,Q^2) + \bar{u}(x,Q^2) + \bar{c}(x,Q^2)) + \\ &- Y_- x(d(x,Q^2) + s(x,Q^2) - \bar{u}(x,Q^2) - \bar{c}(x,Q^2))\Big)(1+\mathcal{P}), \end{aligned} \tag{1.18}$$

$$\begin{aligned} \frac{d^2\sigma_{CC}^{e^-p}}{dxdQ^2} = \frac{G_F^2}{4\pi x}\frac{M_W^4}{(Q^2+M_W^2)^2}\Big(&Y_+ x(u(x,Q^2) + c(x,Q^2) + \bar{d}(x,Q^2) + \bar{s}(x,Q^2)) + \\ &+ Y_- x(u(x,Q^2) + c(x,Q^2) - \bar{d}(x,Q^2) - \bar{s}(x,Q^2))\Big)(1-\mathcal{P}), \end{aligned} \tag{1.19}$$

where G_F is the Fermi weak constant, M_W is the mass of the W bosons and $q(x,Q^2)$ and $\bar{q}(x,Q^2)$, with $q = u, d, c, s$, are the quark and anti-quark densities in the proton, respectively. The CC interactions are more sensitive to the polarization of the electron beam due to the nature of the weak force. Since neutrinos are left-handed the CC cross section is expected to be zero for right-handed electrons (the opposite holds for positrons). Fig. 1.5(a) shows the total charged current DIS cross

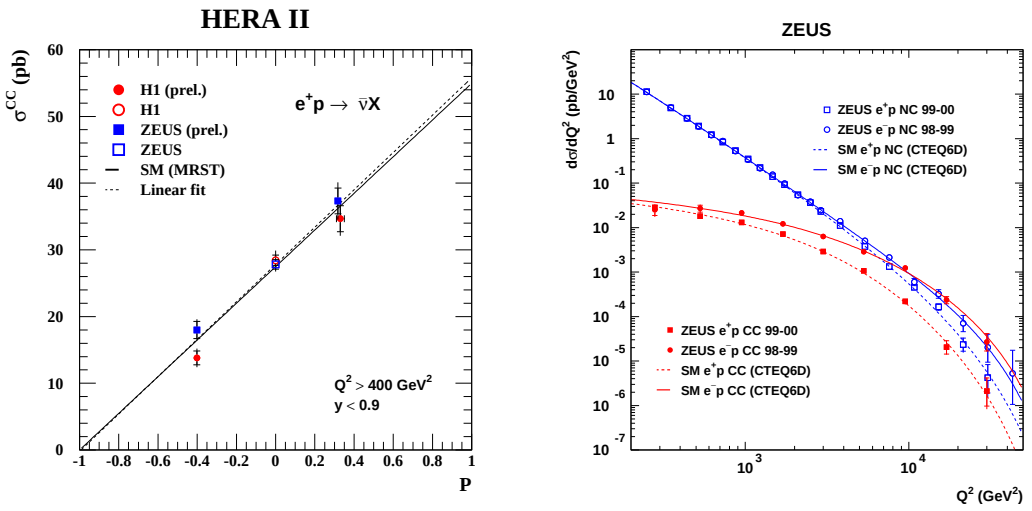

(a) (b)

Figure 1.5: (a) Charged current DIS cross section with three different values of the positron beam polarization ($\mathcal{P} < 0$, $\mathcal{P} = 0$ and $\mathcal{P} > 0$) as measured by the ZEUS and H1 experiments (symbols) with the first e^+p data collected during the new operation phase of HERA (HERA II). As expected from the SM the cross section increases for positive values of the polarization and decreases for negative values. The line represents the Standard Model prediction; (b) neutral current and charged current DIS cross sections at $\mathcal{P} = 0$ as a function of Q^2 as measured by the ZEUS experiment (symbols). The lines are the SM prediction.

section for positron beams as a function of the polarization as measured by the H1 and ZEUS experiments [13].

In Fig. 1.5(b) the NC and CC current cross section, as measured by the ZEUS experiment at HERA with $\mathcal{P} = 0$, are shown as a function of Q^2. The neutral current and charged current cross sections become of similar strength at high Q^2, i.e. when $Q^2 \simeq M_{Z^0}^2$.

1.1.4 Photoproduction

The HERA accelerator is also a tool to study photon-proton interactions. Another way to describe the electron-proton scattering is to decompose it into two processes: the emission of a virtual photon by the electron and the subsequent interaction of the photon with the proton. If the photon is quasi-real ($Q^2 \ll 1\,\mathrm{GeV}^2$) the process is called photoproduction (PhP). This process has a very high cross section at

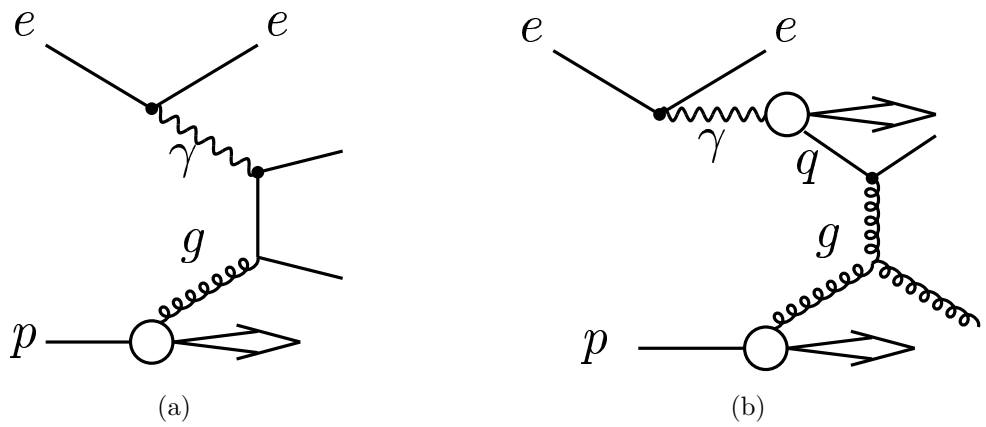

Figure 1.6: (a) Direct photoproduction process; (b) resolved photoproduction process.

HERA ($\sim$ 150 μb) and it is therefore a very important source of background to high-Q^2 DIS processes and to searches for new phenomena. Two different regimes of photoproduction can be distinguished as shown in Fig.1.6. The process is called "direct" when the photon behaves as a point-like particle; "resolved" when the photon fluctuates into a quark-antiquark pair and one of the quarks interacts with the proton.

1.2 Events with high transverse momentum leptons at HERA

In the Standard Model the processes that lead to the production of high transverse momentum leptons are well known. Moreover leptons, especially electrons and muons, are relatively easy to tag experimentally; therefore a deviation from the Standard Model prediction would be a clear sign of new physics. In the last years the two general purpose experiments installed on the HERA ring, H1 and ZEUS, found some discrepancies between data and SM predictions in events with high-p_t leptons. In the following sections a brief description of the SM processes that produce high transverse momentum leptons in the final state at HERA will be given, together with the puzzling results found by ZEUS and H1.

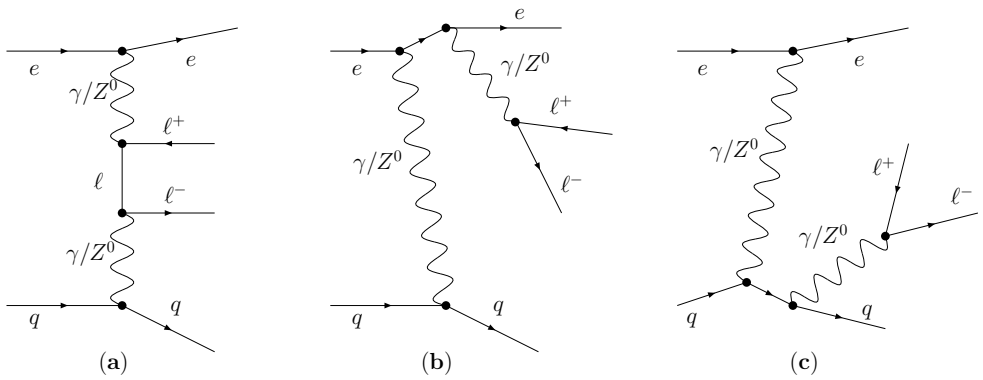

Figure 1.7: Some of the possible Feynman diagrams for di-lepton production at HERA: (a) Bethe-Heitler process; (b) QED Compton or Z^0 on/off shell production; (c) di-lepton production through a photon or a Z^0 radiated from a quark line.

1.2.1 Lepton-pair production

Charged-lepton pair production occurs at HERA through vector-meson resonance production or through an electroweak non-resonant process. The latter is the dominant contribution to the total di-lepton cross section. In Fig. 1.7 three of the possible graphs for electroweak di-lepton production are shown. Three types of processes contribute: the two-photon process or Bethe-Heitler [14] shown in Fig. 1.7(a), the QED Compton-like radiation of a lepton pair from the initial- or final-state electron, also called Cabibbo-Parisi (Fig. 1.7(b)), and the radiation of a lepton pair from a quark or from the proton (Fig. 1.7(c)).

In the first diagram a quasi-real photon radiated by the electron interacts with a photon emitted by the quark (Fig. 1.7(a)); the cross section falls with the transverse momentum of the final-state leptons. The process is called elastic if the proton remains intact in the interaction, quasi-elastic if a proton resonance is formed and it subsequently decays into a proton and pions, inelastic if the proton breaks into the struck quark, which produces a jet in the final state, and into a proton remnant. In the QED Compton processes a photon or a Z^0 radiated by the electron produces a pair of leptons. The cross section peaks at low values of the invariant mass of the two leptons and at the mass of the Z^0. In the last topology, shown in Fig. 1.7(c), the photon that produces the pair of leptons is radiated by the proton or by a quark (Drell-Yan process). This process in ep collisions has a much lower cross section compared to the other channels.

		Electrons		Muons		Taus	
	P_T^X	Data	SM	Data	SM	Data	SM
H1	$P_T^X > 25\,\text{GeV}$	4	1.49	6	1.44	0	0.53
	$P_T^X > 40\,\text{GeV}$	3	0.54	3	0.55	0	0.22
ZEUS	$P_T^X > 25\,\text{GeV}$	2	2.90	5	2.75	2	0.20
	$P_T^X > 40\,\text{GeV}$	0	0.94	0	0.95	1	0.07

Table 1.1: Summary of isolated lepton searches performed by H1 and ZEUS in the first phase of HERA.

1.2.2 W production

The $W^{\pm}$ production occurs at HERA through the processes $ep \to eW^{\pm}X$ and $ep \to \nu W^{\pm}X$, where X is the hadronic final state. The W can then decay into a charged lepton and a neutrino (in 32% of the cases). The first of the two processes has a higher cross section [15] and the diagrams that contribute to it are shown in Fig. 1.8. In all the diagrams, except in the processes shown in Fig. 1.8(d) and Fig. 1.8(e), a real W is produced in the final state. The study of W is useful not only because it is a possible source of SM background for searches for new phenomena, but also because it permits the investigation of the $WW\gamma$ and WWZ^0 vertices that are less known in the Standard Model. Since the graphs where the electron interacts through a photon exchange give the main contribution to W production, the cross sections of the processes $e^+p \to eW^{\pm}X$ and $e^-p \to eW^{\pm}X$ are nearly equal.

1.2.3 Excess of events with high-p_t leptons at HERA

Isolated leptons

H1 found in e^+p data an excess of events characterized by an isolated lepton, high missing transverse momentum and high transverse momentum of the hadronic system, P_T^X. In Table 1.1 the H1 and ZEUS results on isolated lepton search are summarized [1, 2, 16, 17]. In particular H1 found 6 events with isolated muons or electrons with $P_T^X > 40\,\text{GeV}$, whereas only ~ 1 event was expected from SM predictions, mainly from the process $ep \to eWX$. ZEUS did not confirm such excess; on the contrary it found two isolated τ candidates with high missing transverse momentum. The number of events expected from the Standard Model with an isolated τ decaying into hadrons and $P_T^X > 25\,\text{GeV}$ was 0.20.

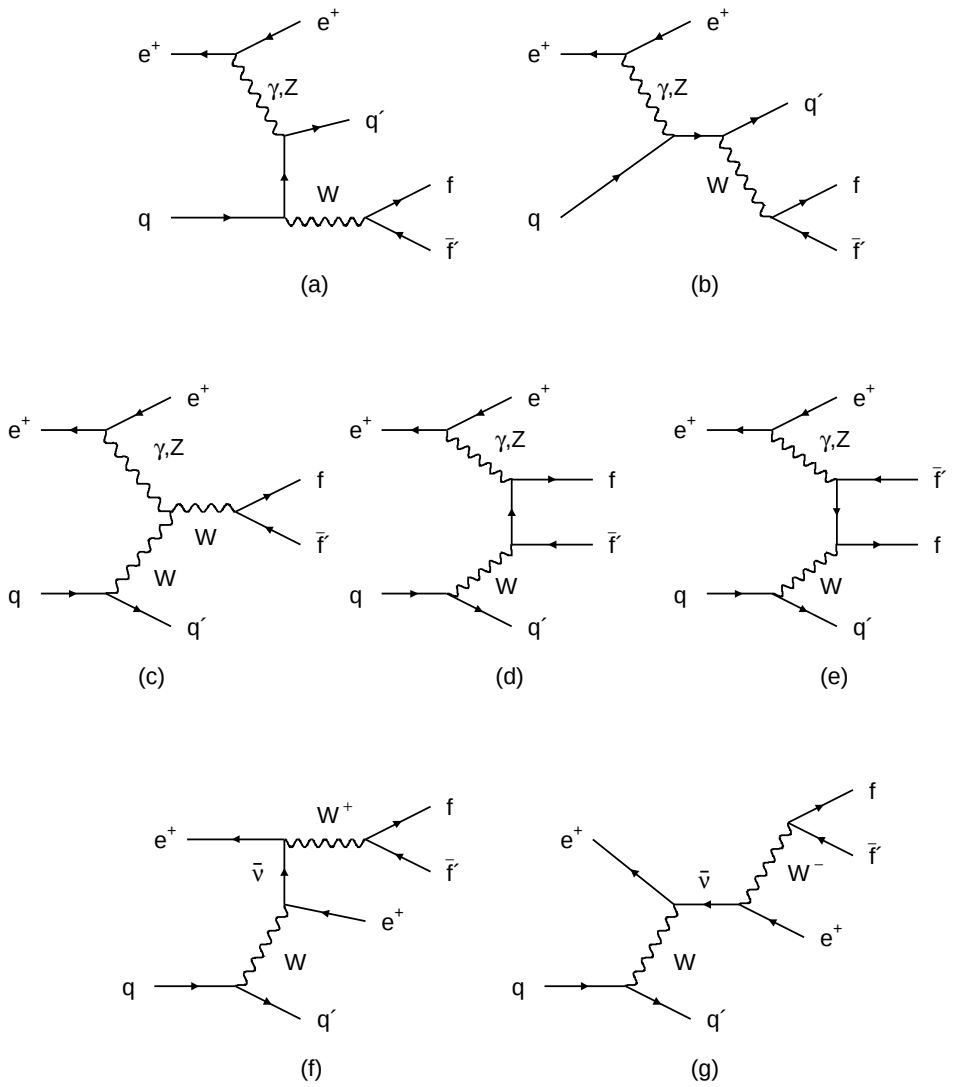

Figure 1.8: Possible Feynman diagrams of the process $e^+p \rightarrow e^+W^{\pm}X$ at HERA.

Multi electron events

Both the H1 and ZEUS collaborations performed an analysis on multi-lepton production. ZEUS found an overall agreement with the Standard Model prediction [18], while H1 found an excess of events with two or three electrons with high invariant mass ($> 100\,\mathrm{GeV}$) [3] as shown in Table 1.2.

	$2e$		$3e$	
	Data	**SM**	**Data**	**SM**
H1	3	0.30±0.04	3	0.23±0.04
ZEUS	2	0.77±0.08	0	0.37±0.04

Table 1.2: Summary of the di-electron and tri-electron events with high invariant mass found by H1 and ZEUS.

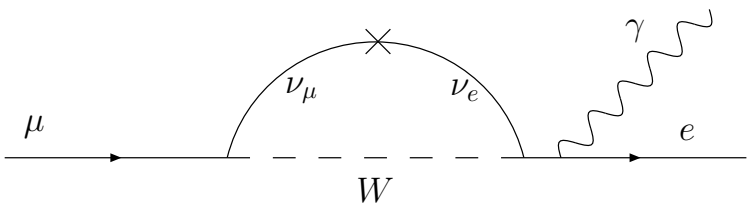

Figure 1.9: Possible loop leading to $\mu \to e$ transitions in the minimal extension of the SM which accounts for the neutrino flavor mixing.

The analysis on multi-muon production [18] has been part of this thesis work and it will be described in Appendix A.

These intriguing results have encouraged further analyses [19, 20, 21, 22] aiming at understanding the origin of these excesses, whether they are due to statistical fluctuations or they are signals of new physics.

1.3 Lepton-flavor violation

In the Standard Model the lepton number is conserved separately for each family of leptons. However, as far as we know, lepton flavor is not a universal symmetry; this has recently become evident with the discovery of neutrino oscillations [23, 24]. Lepton-flavor violation (LFV) in the charged lepton sector induced by the neutrino oscillations, as shown for example in Fig. 1.9, would occur with a too low rate to be detected at the existing experiments [25]. Nevertheless there are several extensions of the Standard Model like supersymmetric models [26] and grand unification theories [27], that predict LFV in the charged lepton sector at higher rates.

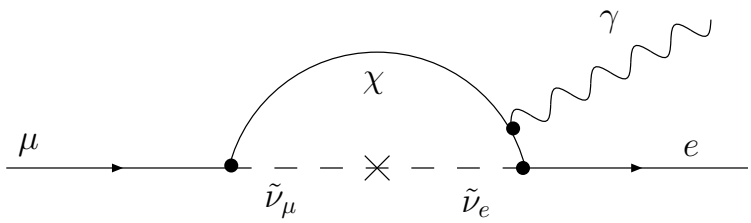

Figure 1.10: Possible loop leading to $\mu \to e$ transitions in SUSY models. The process can also proceed via a loop involving the charged sleptons, $\tilde{\mu}$ and $\tilde{e}$, and a neutralino, χ^0, instead of a chargino.

1.3.1 Neutrino oscillations

For many years solar neutrino experiments observed a lower flux of neutrinos [28, 29, 30, 31, 32, 33] with respect to the flux predicted by solar models [34, 35]. This fact was explained with a possible transition of electron-type neutrinos, produced by nuclear reactions in the Sun, into ν_μ or ν_τ. The experimental confirmation of such hypothesis came only in the last years with the measurement performed by the SNO collaboration of the flux of solar neutrinos from neutral current ($\nu_\ell d \to \nu_\ell pn$) [36] or elastic ($\nu_\ell e^- \to \nu_\ell e^-$) [23] scattering. NC scattering does not depend on neutrino oscillation while the elastic channel has a different dependence with respect to the CC channel ($\nu_e d \to e^- pp$). The measurement of the flux of atmospheric neutrinos made earlier by Super Kamiokande [24] showed that also muon-type neutrinos oscillate into neutrinos of different flavor.

The minimal extension of the Standard Model required to explain neutrino oscillations predicts the existence of right-handed neutrino isosinglets that allow for Dirac mass terms. Majorana mass terms are also possible if the lepton number conservation is not assumed and they could explain, via the see-saw mechanism [37], the smallness of the neutrino masses with respect to the fermion masses.

1.3.2 Supersymmetry

Supersymmetry (SUSY) is one of the most promising candidate theories for extending the Standard Model. It relates the properties of the fermions and of the bosons introducing a bosonic supersymmetric partner for each fermion and *vice-versa*. Moreover, SUSY models solve the hierarchy problem and locally supersymmetric theories naturally incorporate gravity. Since the supersymmetric partners of the SM particles have not been observed at the energy reached up to now, supersymmetry, if it does exist, must be broken at some level. The breaking of

supersymmetry implies the existence of new free parameters that are not predicted by the theory. Therefore, from an experimental point of view, it is necessary to make some assumptions in order to reduce the number of parameters.

In the Minimal Supersymmetric Standard Model (MSSM) the quantum number R-Parity, defined as $R_p = (-1)^{3B+L+2S}$, where B is the baryon number, L the lepton number and S the spin, is conserved. The R-Parity is equal to $+1$ for SM particles and to -1 for their supersymmetric partners; therefore, in this model, non-SM particles can be produced only in pairs and ultimately they decay into the lightest supersymmetric particle (LSP), which is stable. A stable weak interacting massive particle (WIMP) is required also in cosmological models [38] in order to solve the problem of the dark matter. In the MSSM LFV can occur via loops involving sleptons (the supersymmetric partners of the leptons) and charginos (mixed states composed by the supersymmetric partners of the W and of the charged Higgs bosons) or neutralinos (mixed states composed by the supersymmetric partners of the photon, of the Z^0 and of the neutral Higgs boson). Such processes can arise because the slepton mass eigenstates are not necessarily aligned to the lepton ones. An example of lepton-flavor-violating process $\mu \to e\gamma$ in SUSY is shown in Fig. 1.10.

The HERA collider is more sensitive to supersymmetric models that allow for R_p violation. In ep collision the term that describe the R_p violating interactions is $\lambda'_{ijk} L^i_L Q^j_L \bar{D}^k_R$ [39], where λ'_{ijk} is the coupling constant, i, j and k are generation indices and L^i_L, Q^j_L and $\bar{D}^k_R$ denote the left-handed lepton, the quark doublet and the right handed d-quark singlet chiral superfields, respectively. The Lagrangian for this term can be written as:

$$\begin{aligned}\mathscr{L} =& \lambda'_{ijk}(\tilde{\nu}^i_L d^j_L \bar{d}^k_R + \nu^i_L \tilde{d}^j_L \bar{d}^k_R + (\bar{\nu}^i_L)^c d^j_L (\tilde{d}^k_R)^* - \tilde{e}^i_L u^j_L \bar{d}^k_R - e^i_L \tilde{u}^j_L \bar{d}^k_R + \\ & - (\bar{e}^i_L)^c u^j_L (\tilde{d}^k_R)^*) + c.h.\end{aligned} \tag{1.20}$$

A squark can be produced as a resonance with the process $e^+ d \to \tilde{u}^j \to \ell^+ d^k$ or $e^- u \to \tilde{d}^k \to \ell^- u^j$ where ℓ is a charged lepton; d-type squarks have also the $\tilde{d}^k \to \nu^i d^j$ decay mode. If the final-state lepton is a μ or a τ lepton flavor is not conserved. Squarks can also decay via R-Parity conserving interactions into supersymmetric particles like gauginos, that, ultimately, decay into SM particles.

1.3.3 The leptoquark model

Leptoquarks (LQs), predicted by many beyond Standard Model (BSM) theories, are scalar ($S = 0$) or vector ($S = 1$) bosons carrying both baryonic and leptonic numbers. Such particles can be produced at HERA as resonances in the s-channel, as shown in Fig. 1.11(a), if their mass is lower than the HERA center-of-mass energy, $\sqrt{s}$. If the LQ mass exceeds $\sqrt{s}$ the electron and a quark of the proton can exchange

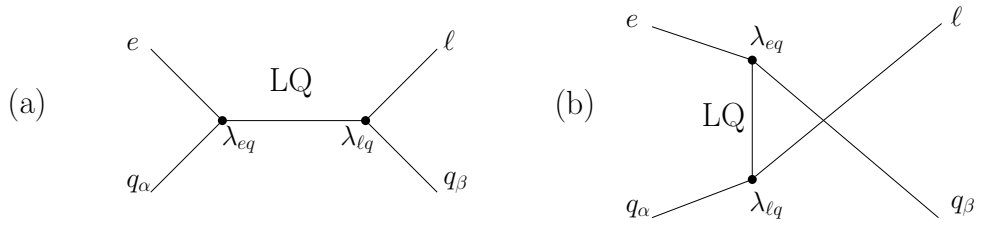

Figure 1.11: (a) s-channel and (b) u-channel diagrams contributing to LFV processes. The subscripts α and β denote the quark generations, and ℓ is either a μ or a τ.

a virtual leptoquark and also the u-channel, shown in Fig. 1.11(b) contributes to the total cross section. In this thesis only the Buchmüller-Rückl-Wyler (BRW) phenomenological leptoquark model [40] will be considered. This model implies a minimal number of assumptions:

- the Lagrangian is invariant under the SM symmetry $SU(3)_C \otimes SU(2)_L \otimes U(1)_Y$;
- LQs of the same $SU(2)$ weak-isospin multiplet are degenerate in mass;
- leptoquarks couple either to left-handed or right-handed lepton but not to both[1].

There are 14 different types of LQs that satisfy these condition, seven are scalar LQs and seven are vector LQs. Using the Aachen [41] notation, scalar (vector) leptoquarks are indicated with S_T^χ (V_T^χ) where χ is the chirality of the lepton that couples with the LQ and T is the weak isospin; when two different states of hypercharge (Y) are admitted, the second one is denoted with a tilde. The different LQ types are reported in Table 1.3 together with their relevant features and quantum numbers: the fermionic number F, defined as $F = 3B + L = 0, \pm 2$; the third component of the weak isospin T_3 which is related to the charge (Q) and the hypercharge by $Q = T_3 + Y/2$; the formation and decay processes of the LQs in the case of an electron beam; the coupling λ and the branching ratio β. From Table 1.3 it can be seen that in the e^-p process LQs with $|F| = 2$ ($F = 0$) can be produced by the fusion of the electron and a valence (sea) quark. The opposite holds for e^+p processes.

As already stated, if the LQ mass is below the center-of-mass energy, $\sqrt{s}$, the s-channel resonance gives the dominant contribution to the cross section at HERA.

[1] LQs that couple to both left-handed and right-handed leptons would lead to forbidden meson decays that are already well constrained by experiments.

Since the mass of the LQ satisfies $M_{\rm LQ} = \sqrt{xs}$, masses greater than 140 GeV at $\sqrt{s} = 318\,\text{GeV}$ require an $x > 0.19$. Therefore the cross section for low-mass LQs is dominated by the valence quarks and $e^- p$ collisions are more sensitive to $|F| = 2$ LQs which can be produced by electron-valence-quark fusion; the opposite is true for $e^+ p$ data.

For small values of the Yukawa coupling λ_{eq}, the resonance is narrow and the s-channel Breit Wigner can be approximated with a δ-function. With this approximation, called narrow width approximation (NWA), the cross section can be expressed in the form:

$$\sigma^{\rm NWA}_{T_3}(s, M_{\rm LQ}) = (J+1)\frac{\pi\lambda^2_{eq_1}}{4s}\sum_{T_3=-T}^{T} C_{T_3} q_1\left(x = \frac{M^2_{\rm LQ}}{s}, Q^2_0\right) B(\text{LQ} \rightarrow l q_j), \quad (1.21)$$

where C_{T_3} is the square of the relevant $SU(2)$ Clebsch-Gordan coefficient and $q_1(x, Q^2_0)$ is the valence-quark density evaluated at the scale $Q^2_0 = M^2_{\rm LQ}$.

If $M_{\rm LQ} > \sqrt{s}$ both the s- and u-channel diagrams contribute (see Fig. 1.11). If $M_{\rm LQ} \gg \sqrt{s}$ the contact interaction formalism can be used: the LQs propagator is approximated with $(\lambda_{1q_\alpha}\lambda_{\ell q_\beta}/M^2_{\rm LQ})^2$, where α and β are the quark generation indices and ℓ is the final-state lepton. The cross section for $F = 0$ LQs in $e^+ p$ collisions in this high-mass approximation (HMA) can be written as:

$$\sigma^{\rm HMA} = \frac{s}{32\pi}\left(\frac{\lambda_{eq_\alpha}\lambda_{\ell q_\beta}}{M^2_{\rm LQ}}\right)^2 \left(\int dx\ dy\ x q_\alpha(x, \hat{s}) f(y) + \right. \\ \left. + \int dx\ dy\ x \bar{q}_\beta(x, -\hat{u}) g(y)\right), \quad (1.22)$$

with:

$$f(y) = \begin{cases} 1/2 & \text{scalar LQ} \\ 2(1-y)^2 & \text{vector LQ} \end{cases}, \qquad g(y) = \begin{cases} (1-y)^2/2 & \text{scalar LQ} \\ 2 & \text{vector LQ} \end{cases}, \quad (1.23)$$

where $\hat{s} = xs$ and $\hat{u} = sx(y-1)$ are the scale at which the quark densities are calculated. The first and the second integrals represent the s- and u-channel contributions, respectively. Equation 1.22 holds also in the $|F| = 2$ case, replacing q with $\bar{q}$ and *vice-versa*.

LQ	F	T_3	Y	Q	Process	Coupling constant	β
S_0^L	2	0	1/3	-1/3	$e_L^- u_L \to l^- u$	λ_L	1/4
					$e_L^- u_L \to \nu_l d$	$-\lambda_L$	1/4
S_0^R	2	0	1/3	-1/3	$e_R^- u_R \to l^- u$	λ_R	1/2
$\widetilde{S}_0^R$	2	0	4/3	-4/3	$e_R^- d_R \to l^- d$	λ_R	1/2
S_1^L	2	0		-1/3	$e_L^- u_L \to l^- u$	$-\lambda_L$	1/4
					$e_L^- u_L \to \nu_l d$	$-\lambda_L$	1/4
		-1		-4/3	$e_L^- d_L \to l^- d$	$-\sqrt{2}\lambda_L$	1/2
$V_{1/2}^L$	2	-1/2		-4/3	$e_L^- d_R \to l^- d$	λ_L	1/2
$V_{1/2}^R$	2	1/2	5/6	-1/3	$e_R^- u_L \to l^- u$	λ_R	1/2
		-1/2		-4/3	$e_R^- d_L \to l^- d$	λ_R	1/2
$\widetilde{V}_{1/2}^L$	2	-1/2		-1/3	$e_L^- u_R \to l^- u$	λ_L	1/2
V_0^L	0	0	2/3	-2/3	$e_L^- \bar{d}_R \to l^- \bar{d}$	λ_L	1/4
					$e_L^- \bar{d}_R \to \nu_l \bar{u}$	λ_L	1/4
V_0^R	0	0	2/3	-2/3	$e_R^- \bar{d}_L \to l^- \bar{d}$	λ_R	1/2
$\widetilde{V}_0^R$	0	0	5/3	-5/3	$e_R^- \bar{u}_L \to l^- \bar{u}$	λ_R	1/2
V_1^L	0	0		-2/3	$e_L^- \bar{d}_R \to l^- \bar{d}$	$-\lambda_L$	1/4
					$e_L^- \bar{d}_R \to \nu_l \bar{u}$	$-\lambda_L$	1/4
		-1		-5/3	$e_L^- \bar{u}_R \to l^- \bar{u}$	$\sqrt{2}\lambda_L$	1/2
$S_{1/2}^L$	0	-1/2		-5/3	$e_L^- \bar{u}_R \to l^- \bar{u}$	λ_L	1/2
$S_{1/2}^R$	0	1/2	7/6	-2/3	$e_R^- \bar{d}_R \to l^- \bar{d}$	$-\lambda_R$	1/2
		-1/2		-5/3	$e_R^- \bar{u}_L \to l^- \bar{u}$	λ_R	1/2
$\widetilde{S}_{1/2}^L$	0	-1/2		-2/3	$e_L^- \bar{d}_L \to l^- \bar{d}$	λ_L	1/2

Table 1.3: The table shows the 14 different LQ types following the Aachen notation. For each LQ, the fermionic number F, the third component of the weak isospin T_3, the hypercharge Y, the charge Q, the production and decay processes with an electron beam, the coupling and the branching ratio β are indicated. The production process with a positron beam can be obtained applying the charge conjugation operator.

Chapter 2

Experimental setup

In this chapter an overview of the HERA accelerator and of the ZEUS detector will be given. The detector will be described the way it was in its 1994–2000 configuration when the data used in this analysis were taken. During the 2000 shutdown both the accelerator and the detector underwent a substantial upgrade. More details on the HERA upgrade and on the newly installed ZEUS components will be given in Chapter 8. The two phases of data taking before and after the upgrade are referred to as HERA I and HERA II.

2.1 The HERA collider

HERA (Hadron-Elektron Ring Anlage), the first electron-proton collider, is located at the DESY (Deutsches Elektronen Synchroton) laboratory in Hamburg, Germany (Fig. 2.1(a)). The machine, which has operated since 1992, can accelerate positrons and electrons up to an energy of 27.5 GeV and protons up to an energy of 920 GeV. The achievable energy in the center of mass of the electron-proton system, 318 GeV, is much greater than the typical energies of fixed target experiments. The ring is 6.3 km long and it consists of four circular sectors and four straight sectors (Fig. 2.1(b)), where the experimental halls are located. Proton and electron or positron beams are stored and accelerated in two separated rings, and brought into collision at zero crossing angle in the North and South halls, where the H1 and ZEUS experiments are situated. The electron and proton beams consist of up to 210 bunches of about 10^{10} particles, spaced in time by 96 ns. Several bunches are left unfilled and the resulting unpaired bunches (pilot bunches) are used for background studies.

The HERMES experiment, located in the East hall, is a fixed target experiment and it uses only the electron beam. The longitudinally polarized electrons are scattered on an internal polarized gas target to study the spin structure of the nucleons.

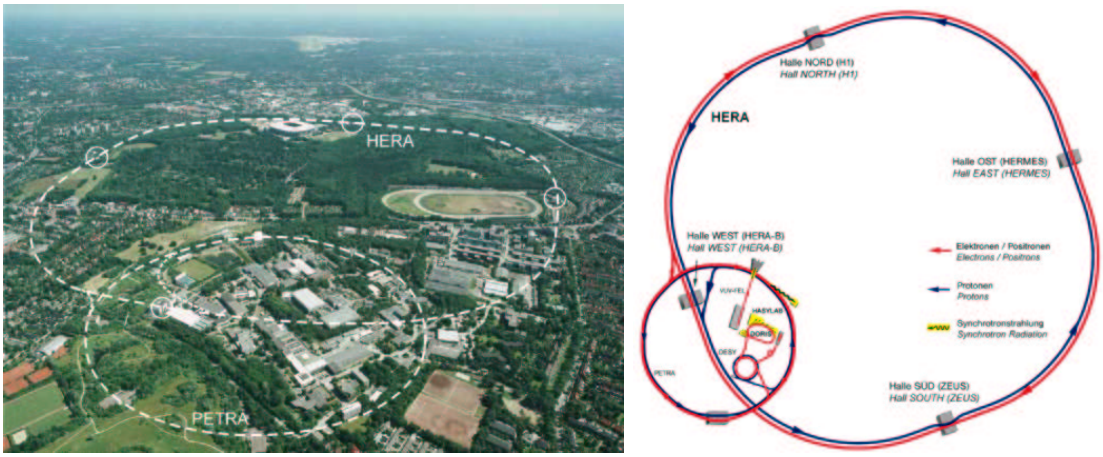

(a) (b)

Figure 2.1: (a) View of DESY from an airplane. The position of PETRA and HERA are marked with dashed lines. The ZEUS hall is located outside the DESY site on the right in the picture; (b) schematic view of the HERA collider.

The HERA-B experiment was situated in the West hall and it was designed to study the CP violation in the $B - \bar{B}$ system exploiting the collisions of the HERA proton beam halo on a wire target. This experiment was operated till 2003.

In this thesis only data collected during the HERA I period (1994–2000) have been analyzed. However in chapter 8 an overview of the HERA II period and of the ZEUS upgrade will be given, together with the first look at exotic events in 2003–2004 data.

The event rate, R, for a specific process a and its cross section, σ_a, are proportional:

$$R_a = \mathcal{L}\sigma_a, \tag{2.1}$$

and the proportionality factor, $\mathcal{L}$, is called luminosity. At a collider the luminosity can be written in the form:

$$\mathcal{L} = f\frac{n_1 n_2}{4\pi\sigma_x\sigma_y}, \tag{2.2}$$

where n_1 and n_2 are the number of particles in the two bunches, f the collision frequency and σ_x and σ_y describe the x and y dispersion of the beams. The beam size depends on two parameters: the transverse emittance, ϵ, and the amplitude function, β:

$$\pi\sigma^2 = \beta\epsilon. \tag{2.3}$$

The amplitude function is a characteristic of the collider optics, while the transverse emittance is a quantity that reflects the beam quality. The instantaneous luminosity

Year	Collisions	$\mathbf{E_e}$ (GeV)	$\mathbf{E_p}$ (GeV)	$\sqrt{\mathbf{s}}$ (GeV)	L ($\mathbf{pb^{-1}}$)
1994	e^+p	27.5	820	300	2.71
1995					6.32
1996					10.8
1997					27.8
1994–1997	e^+p	27.5	820	300	47.7
1998	e^-p	27.5	920	318	4.60
1999					12.1
1998–1999	e^-p	27.5	920	318	16.7
1999	e^+p	27.5	920	318	19.6
2000					45.4
1999–2000	e^+p	27.5	920	318	65.1

Table 2.1: Type of collision, electron (E_e) and proton (E_p) energy, and energy available in the center of mass $\sqrt{s}$ of the ep system in different periods during HERA I data taking. In the last column the integrated luminosity gated by ZEUS and usable for analysis is reported.

reached by HERA during the 1994–2000 years was $1.4 \cdot 10^{31}$ cm^{-2}s^{-1}. For practical reasons, in this thesis the term luminosity will refer to the integrated luminosity over time:

$$L = \int \mathcal{L}(t)dt. \tag{2.4}$$

In Table 2.1 the type of collision, and the center-of-mass energy $\sqrt{s}$ and the luminosity collected by ZEUS in 1994–2000 years are summarized. Figs. 2.2(a) and 2.2(b) show the integrated luminosity delivered by HERA and the luminosity (usable for analysis) gated by ZEUS in the 1993–2000 period.

2.2 The ZEUS detector

The ZEUS detector [42] is a general-purpose high-energy-physics detector with a nearly hermetic coverage, designed to study different kinds of physics in ep scattering.

The ZEUS coordinate system is a right-handed system with the vertex in the nominal interaction point, the Z axis aligned with the proton direction (referred to as the forward direction), the X axis pointing to the center of HERA and the Y axis pointing upwards. The θ and ϕ angles are measured from the Z and X axes, respectively. Due to the large momentum imbalance of the two beams, most of the

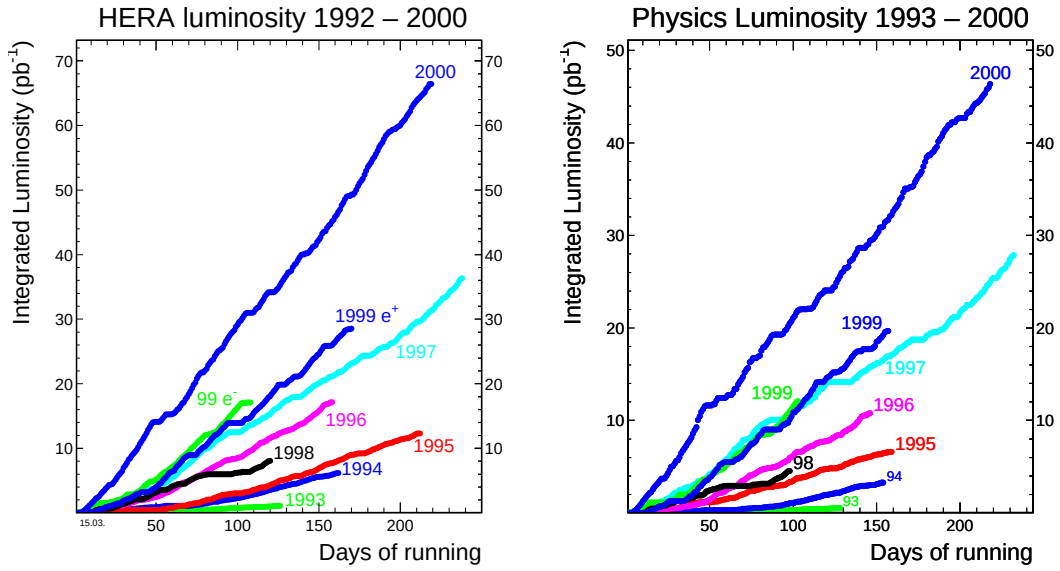

(a) (b)

Figure 2.2: Integrated luminosity (a) delivered by HERA and (b) gated by ZEUS during HERA I.

particles are boosted into the forward direction; therefore the detector (Fig. 2.3) has a forward-backward asymmetry.

In 1995 the innermost detector was the vertex detector (VTX) that was removed during the 1995–1996 shutdown. Therefore during the 1996–2000 period the reconstruction of the interaction vertex relied essentially on the central tracking detector (CTD). The CTD, immersed in a magnetic field of 1.43 T provided by a superconducting solenoid, is used to reconstruct the charged particle tracks and to measure their momentum. The track reconstruction for forward particles is complemented by the forward detector (FDET). The rear region is covered by the rear tracking detector (RTD).

The ZEUS uranium-scintillator calorimeter (CAL), designed to measure the energy of both electrons and hadrons with high resolution, is placed between the solenoid and the iron yoke, which provides the return path for the magnetic flux. The yoke is instrumented with the backing calorimeter (BAC), which can detect muons and hadron showers that are not completely contained in the main calorimeter. Muons are detected also by the forward (FMUON), barrel (BMUON) and rear (RMUON) muon chambers, that are located inside and outside the yoke. The luminosity monitor (LUMI) was placed at $Z = -107$ m. In the following sections

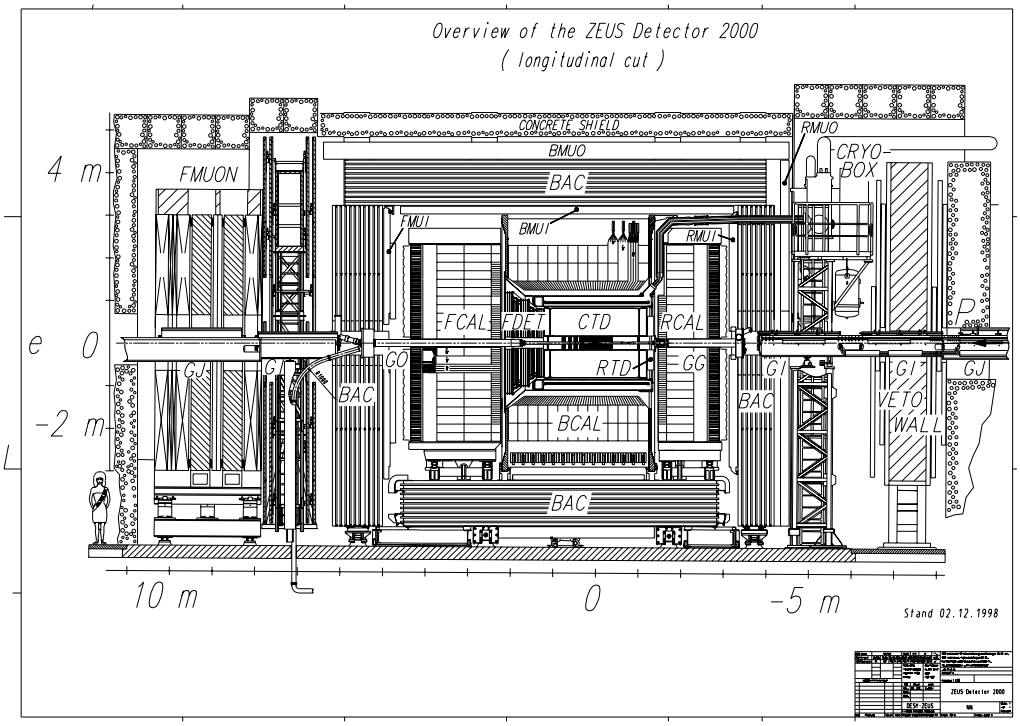

Figure 2.3: Schematic view of the ZEUS detector in the ZR projection.

a more complete description of the detector components that are relevant for this thesis will be given.

2.3 The central tracking detector

The CTD [43] is a drift chamber designed to measure the momentum and the direction of the charged tracks. Moreover, from the measurement of the energy loss dE/dx, a particle identification is possible. The chamber, 2.05 m long with an inner radius of 18.2 cm and an outer radius of 79.4 cm, has a polar angle coverage of $15° < \theta < 164°$. The CTD is made of 9 superlayers: each superlayer consists of 8 wire layers. Figure 2.4(a) shows the $X - Y$ section of a CTD octant. The 4608 sense wires included in the chamber are arranged in 576 cells. The 8 sense wires in a CTD cell are surrounded by field wires tilted of 45° with respect to the radial direction, in order to compensate for the Lorentz angle due to the electric and magnetic fields. The superlayers are conventionally numbered starting from the inner one. In the odd superlayers wires run in the Z direction while in the even ones they have a small stereo angle of $\pm 5°$ to permit the reconstruction of the Z

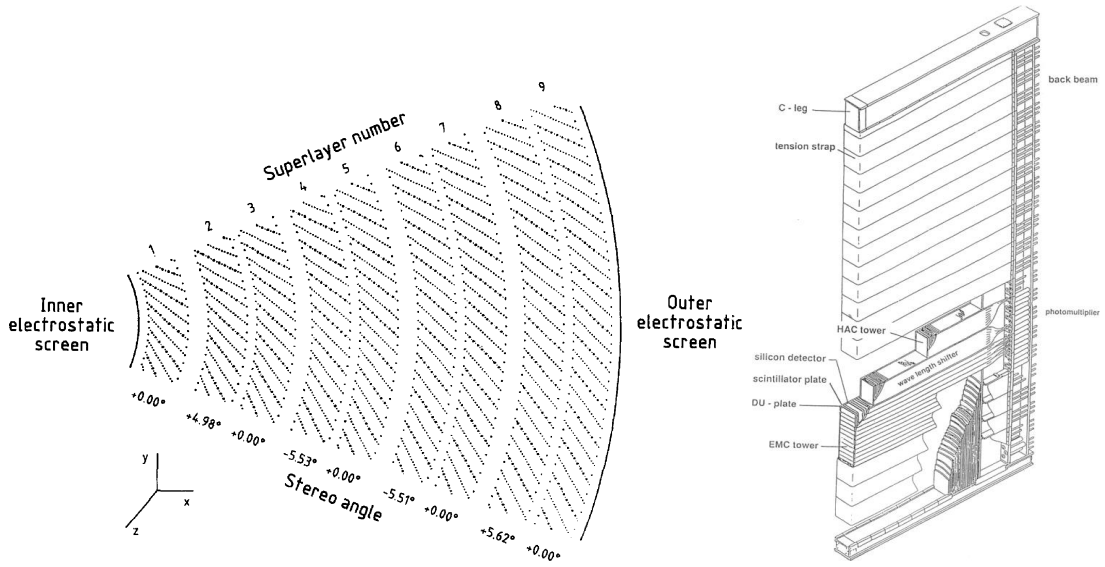

(a) (b)

Figure 2.4: (a) CTD octant in the XY projection; (b) schematic view of an FCAL module.

coordinate.

The detector is filled with a mixture of $Ar/CO_2/C_2H_6$ in the proportion 83:5:12. A charged particle crossing the CTD produces a ionization in the gas. The electron cloud starts to drift towards the sense wires that are positive while the positive ions drift in the negative field wire direction. The avalanche effect that occurs near the sense wires produces a multiplication of the signal by a factor of $10^4 - 10^5$. The spatial resolution is about 200 μm in the $r - \phi$ plane and $\sim$ 2 mm in the Z direction. The magnetic field of 1.43 T provided by the superconducting solenoid assures a transverse momentum p_T resolution of:

$$\sigma(p_T)/p_T = 0.0058 \cdot p_T(\,\mathrm{GeV}) \oplus 0.0065 \oplus 0.0014/p_T(\,\mathrm{GeV}),$$

at $\theta = 90°$. The first term comes from the hit position resolution, the second and the third are due to the multiple scattering inside the chamber and in the material before the CTD.

The interaction vertex is reconstructed with a typical resolution of 0.4 cm along the beam and 0.1 cm in the transverse direction with respect to the beam.

2.4 The calorimeter

The main component of the ZEUS detector is the high resolution uranium-scintillator sampling calorimeter (UCAL) [44]. The detector consists of 3.3 mm thick absorber plates made of depleted uranium (98.1% ^{238}U, 1.7% Nb, 0.2% ^{235}U) alternated with 2.6 mm thick organic scintillators (SCSN-38 polystyrene) as active material. The calorimeter is designed to optimize the resolution of the measurement of the hadronic energy. The uranium absorber permits the compensation of the signal from hadronic showers so that the response of the detector to hadronic showers and electromagnetic showers of the same energy is nearly equal. The achieved resolution is $\frac{\sigma(E)}{E} = \frac{18\%}{\sqrt{E}} \oplus 2\%$ for electromagnetic showers and $\frac{\sigma(E)}{E} = \frac{35\%}{\sqrt{E}} \oplus 1\%$ for hadronic showers, where E is the shower energy measured in GeV.

The ZEUS calorimeter is subdivided into three parts: the forward calorimeter (FCAL), the barrel calorimeter (BCAL) and the rear calorimeter (RCAL). The FCAL and the BCAL consist of two hadronic sections (HAC) and one electromagnetic section (EMC). The HAC cells in FCAL have a section of 20×20 cm^2 and have an interaction length λ of 3.1, while the dimension of the EMC cells is 20×5 cm^2 and $26X_0$ in length, where X_0 is the radiation length. In Fig. 2.4(b) an FCAL module is shown. In BCAL the cells have different lengths: 2.0λ for the hadronic cells and $21X_0$ for the electromagnetic ones. The RCAL has only one electromagnetic and one hadronic section: the cells have the same dimension as the FCAL ones, with the exception of the section of EMC cells which is 20×10 cm^2.

The scintillation light is converted to a measurable signal using photomultipliers coupled to the scintillator through wavelength shifters. Each cell has two photomoltiplier tubes, called left and right. The energy imbalance of each cell is defined as $|\frac{E_l - E_r}{E_l + E_r}|$, where E_l (E_r) is the energy measured in the left (right) photomultiplier. The imbalance is close to zero when both photomultipliers work correctly.

The calorimeter also provides an accurate timing resolution of about 1 ns for energy deposits larger than 1 GeV, which is used for triggering purposes and to reject background events.

The calibration of the photomultipliers and of the electronics is performed with lasers and charge pulses, and by using the small signal ("uranium noise") from the depleted uranium.

2.5 The backing calorimeter

The main purpose of the backing calorimeter [42], shown in Fig. 2.5, is to measure the energy of those particle showers that are not fully contained in the main high-resolution calorimeter and to measure the position of the muons. Muons produced in the HERA *ep* collisions are at minimum ionization, thus they release only a small

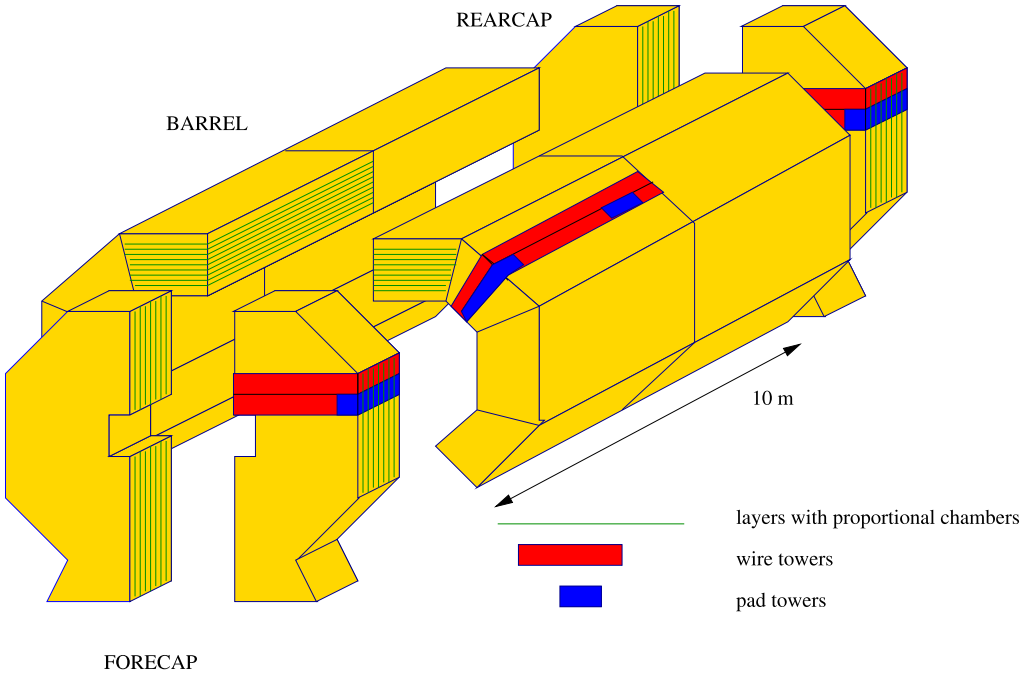

Figure 2.5: Schematic view of the backing calorimeter.

energy in the main calorimeter and they can be detected by the BAC and by the muon chambers. The measurements of the BAC complement those coming from the muon detectors, especially in the lower part of ZEUS where the muon chambers are not available. The BAC, which is installed in the yoke outside the calorimeter, consists of aluminum proportional chambers, filled with a mixture of Ar/CO_2 in the proportion 9:1. The chambers, typically 5 m long, are made of 7 or 8 cells each with a 15×11 mm^2 section and are arranged in layers: 9 in the forward cap, 8 in the barrel region and 7 in the rear cap. In the barrel region the anode wires are parallel to the beam axis, while in the forward and rear cap they are parallel to the X axis. The cathode pads cover each cell on the top. In order to reconstruct the third coordinate the cathodes are segmented along the Z coordinate in the barrel region and along the X axis in the forward and rear caps. The cathode pads on top of three or four adjacent layers of chambers are called pad towers. The typical transverse dimension of a pad tower is 50×50 cm^2. The energy resolution of the BAC is approximately $110\%\sqrt{E(\,\mathrm{GeV})}$.

More details can be found in Sec. 8.3.2.

2.6 The muon detectors

The design of the muon chambers had to take into account the boost into the forward direction of the particles coming from the interaction point. Therefore, as in other detectors, the forward muon chambers have a different structure with respect to the barrel and rear muon chambers.

2.6.1 The forward muon detector

The forward muon chambers [42], shown in Fig. 2.6, are made of four streamer-tube trigger planes (LT1÷LT4) and four drift-chamber planes (DC1÷DC2). One of the streamer-tube planes and one of the drift-chamber planes are placed between the BAC and the UCAL. The measurement of the muon momentum is made possible by two toroidal iron magnets which provide a magnetic field of 1.7 T. Larger polar angles, $15° < \theta < 35°$, are covered by two additional planes of limited streamer tubes (LW1,LW2).

The streamer tubes are used by the trigger to suppress the background; they employ a mixture of $Ar/CO_2/C_4H_{10}$ in the proportions 3%/89%/8%. Each plane consists of two layers; the signal from the streamer tubes is read out by two planes of copper strips that provide the measurement of the distance from the beam axis ρ and of the azimuthal angle ϕ. In order to reduce the inefficiency, the signal from the two planes is put into logical OR.

Each plane of the drift chambers is made of 8 chambers with a trapezoidal shape; each chamber consist of 32 cells, each of them containing four sense wires. The spatial resolution of the drift chambers is 200 μm.

The FMUON detector allows for a muon momentum measurement up to 100 GeV with a resolution of 25% for high momentum muons.

2.6.2 Barrel and rear muon chambers

The barrel and rear muon detectors [45] cover an area of two thousands m^2 and have a modular structure. The basic element is the chamber. The chambers in the barrel and rear part, placed between the CAL and the BAC, are called BMUI and RMUI, respectively, whereas the outer chambers are denoted as BMUO and RMUO. In Fig. 2.7 the chambers that constitute the BMUON detector are shown. Each chamber is made of a structure of aluminum honeycomb bearing the weight with two planes of limited streamer tubes at each side. Each tube contains eight cells with one (anode) sense wire inside. The distance between two sense wires is 1 cm. The two streamer tube planes are displaced by half cell to permit a good reconstruction of particle tracks even if they pass near the cell border. The inner

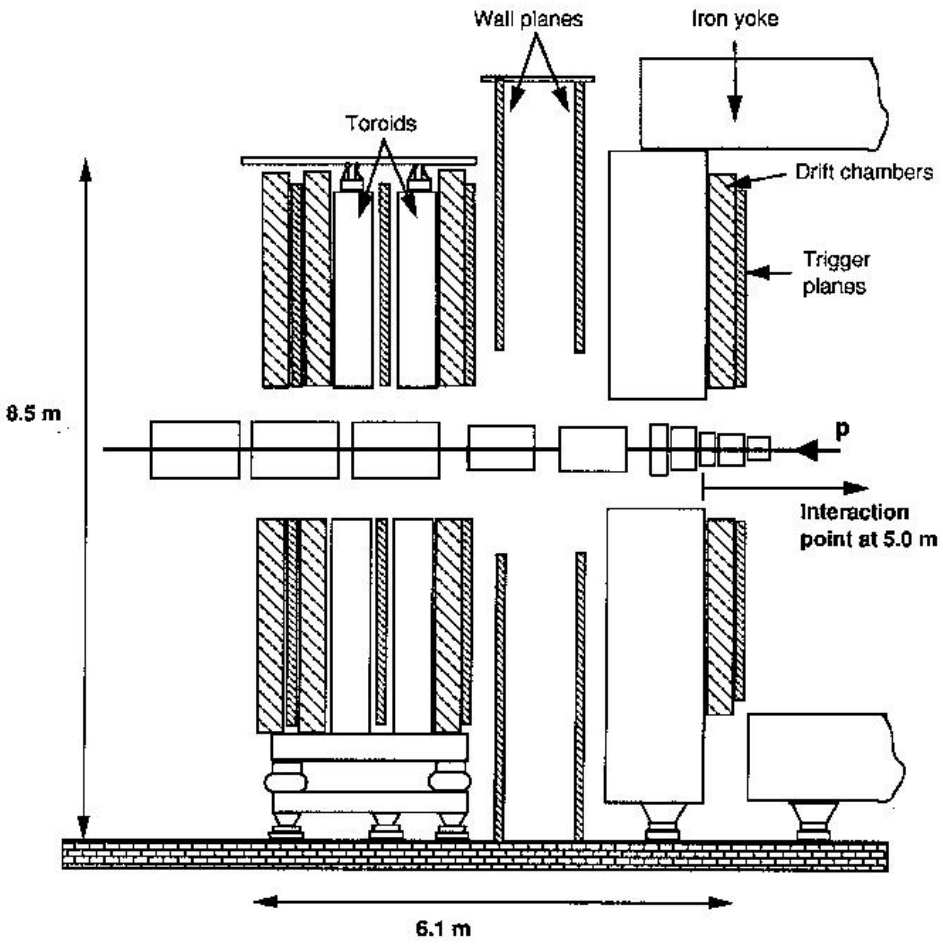

Figure 2.6: Schematic view of the FMUON detector.

walls of the cells, covered by graphite, act as cathodes. On one of the outer walls, conductive strips orthogonal to the wires spaced by 1.5 cm are placed, so that it is possible to reconstruct the position of the particles. The spatial resolution is about 1 mm. The cells are filled with a mixture of CO_2/C_4H_{10}.

In BMUON the wires are parallel to the beam axis, while in RMUON the wires are aligned in the X direction.

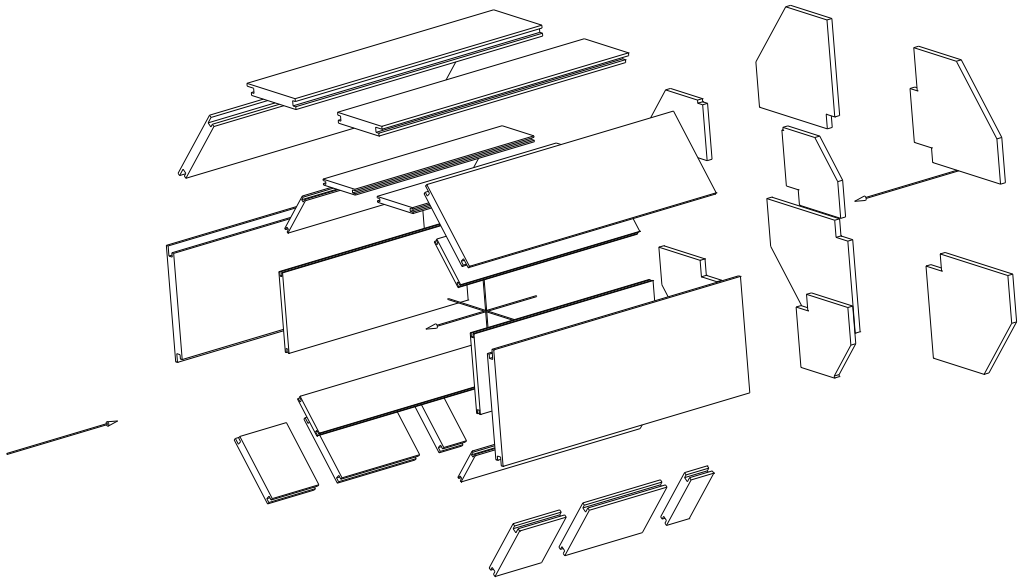

Figure 2.7: Schematic view of the BMUON detector.

2.7 The luminosity monitor

Luminosity is measured by ZEUS using the bremsstrahlung process $ep \to ep\gamma$ [14]. The cross section of this process is very high, of the order of 20 mb, and it is known with an accuracy of 0.5%. The rate of photons produced with an angle smaller than 0.5 mrad with respect to the electron direction is measured by a lead-scintillator electromagnetic calorimeter located at $Z = -107$ m from the nominal interaction point. The calorimeter is shielded from the synchrotron radiation by a carbon-lead filter. The energy resolution is $\sigma(E)/E = 23\%/\sqrt{E/\,\mathrm{GeV}}$. The main source of background is the bremsstrahlung of the electron in the residual gas present in the beam pipe: the importance of this effect can be estimated using the pilot bunches. The overall uncertainty on the luminosity measurement is in the range $1.5 - 2\%$.

2.8 The trigger

In HERA the distance between two bunch crossings is 0.096 μs, but the total interaction rate is 10–100 kHz. The aim of the trigger system [42, 46] is to reduce this rate to less than 10 Hz in order to be able to write events on tape with the minimum loss of physically interesting events. The ZEUS trigger is organized in three levels, as described in the following sections.

2.8.1 The first level trigger

The first level trigger (FLT) is a hardware trigger that permits to reduce the event rate down to 500 Hz. Every component has its own trigger which has 0.25 μs time to decide whether the event is good and to send the information to the global first level trigger (GFLT), which makes a decision in the following 1.9 μs. The overall time taken by the FLT is hence about 4.4 μs, which corresponds to 46 HERA beam crossings. During the FLT decision data are stored in pipelines and only if the event is accepted, the information is sent to the second level trigger.

Due to the required processing speed, the FLT makes use of only a fraction of the event information. Events with a reconstructed vertex outside the detector are rejected. The calorimeter first level trigger, CFLT calculates global sums of energy and transverse energy, and searches for patterns compatible with an electron or a muon. Most of the beam gas related background is rejected at this level and the output rate is of the order of few hundred Hz.

2.8.2 The second level trigger

The second level trigger, SLT, is software based and it uses a network of transputers. Each component has its own SLT processor that sends its response to the global second level trigger, GSLT. The identification of the calorimeter clusters and of the CTD tracks allows an approximate reconstruction of the events already at this level, and also a much more effective selection of physics events with respect to the background. The output rate of the SLT is about 50–100 Hz.

2.8.3 The third level trigger

The events passing the SLT are reconstructed using the event builder, EVB and then sent to the third level trigger, TLT. In order to classify each event, the TLT uses a computer farm with a software very similar to the one used in the offline analysis. The events are finally written on tape at a frequency of 3–5 Hz.

Chapter 3

Simulation of the signal processes and the background

The complexity of particle physics interactions and of the detector response makes the analytic treatment of the entire physical process and of the detector efficiency and acceptance impossible. Monte Carlo (MC) generators are used to simulate the processes on the basis of statistical methods. Their output consists of the final-state particles and their four-momenta. This information is then passed to a subsequent program that simulates the detector response.

The simulation of the process involves different steps. The first step is the simulation of the hard process, that, in *ep* collision, means the interaction between the electron/positron or the photon and the parton inside the proton. The simulation has then to take into account the initial- and final-state QCD radiation that can be calculated perturbatively. The last and non trivial step is to go from the parton level to final-state hadrons; this step is called hadronization.

In this chapter a description of the different methods used by the MC generators to treat the QCD radiation and the hadronization will be given. Then the event generators used to simulate the SM background and the signal will be described. Finally the detector response simulation will be summarized.

3.1 QCD radiation

The QCD initial- or final-state radiation in DIS accounts for events with two or three jets in the final state. The most common approaches to describe the QCD radiation are the Color Dipole Model (CDM) and the Matrix Element Parton Shower Model (MEPS).

In the CDM method [47] the radiation is assumed to be emitted by independently radiating dipoles (see Fig. 3.1(a)). In *ep* scattering case, the first dipole is made

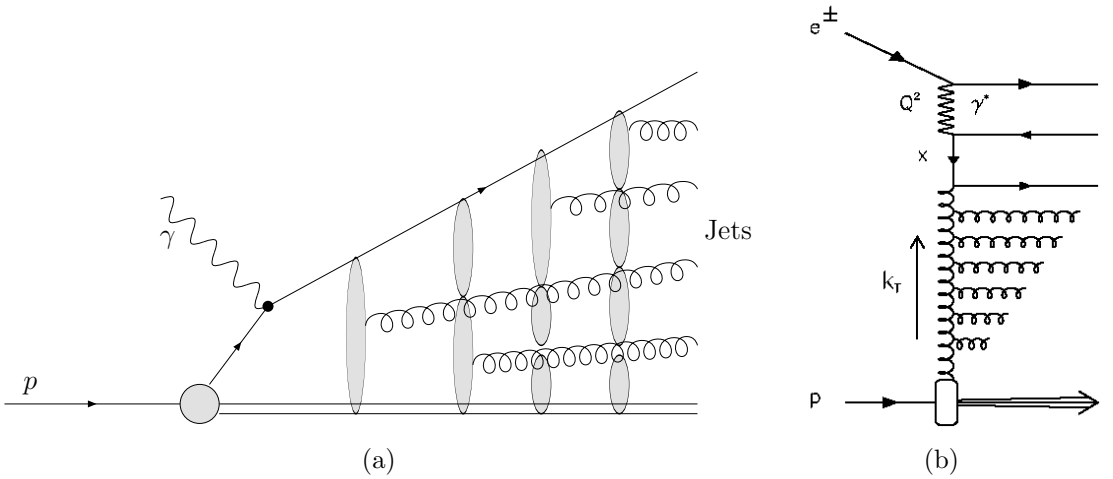

Figure 3.1: (a) Gluon emission by color dipoles in the CDM; (b) angular ordering in the parton shower models.

up by the struck quark and the proton remnant. The gluon radiated by the first dipole is itself, together with the struck quark and the proton remnant, a source of dipoles that can emit softer gluons.

In the MEPS model, the radiation corresponds to higher orders in perturbative QCD; the higher order terms are all summed up using the DGLAP "leading log approximation". A parton shower is generated and the splitting processes are calculated using the Altarelli-Parisi splitting functions [9]. The angular ordering (see Fig. 3.1(b)) is imposed for the final radiation: considering, for example the branching $q_0 \rightarrow qg$, the original color charge is inherited by the gluon while q and g share a color-anticolor pair. A gluon emitted at large angles corresponds to a large wavelength and it is not able to resolve the qg pair, but it feels only the color charge of q_0. Therefore such soft gluon can be thought of as being emitted by q_0 rather then by the qg system.

3.2 Hadronization

Perturbative QCD describes how the partons evolve, but in the detector, owing to the color confinement, we can observe only colorless hadrons. The process that leads to the formation of hadrons starting from partons is non-perturbative and not well understood yet. There are two widely used models that describe the complex process of hadronization: the Lund string model [48] and the Cluster fragmentation

model [49].

In the former the color field between a $q\bar{q}$ pair moving apart is parametrized as a string with constant energy density (of the order of 1 GeV/fm), to take into account the self-interactions of the gluons. As the distance between $q\bar{q}$ increases, the potential energy of the string becomes high enough to produce another $q\bar{q}$ couple. The process continues with the formation of smaller strings and ends when the energy of the initial $q\bar{q}$ couple is exhausted.

The Cluster fragmentation model exploits the concept of pre-confinement of color. Gluons are non-perturbatively split into quark-antiquark pairs. Each jet consists of a set of outgoing $q\bar{q}$ couples. Color singlet clusters are then considered. Due to the color pre-confinement the invariant mass and the size of the clusters peak to low values and they are asymptotically independent of the hard subprocess and the energy scale. Clusters subsequently decay into pairs of colorless hadrons or, if they are too light, they decay into the lightest hadrons of their flavor, exchanging four-momentum with the neighboring clusters to adjust the mass.

In the generators used in this analysis the parameters of the hadronization models were set to the values that had been tuned according to previous LEP and HERA data.

3.3 Simulation of the LFV signal

In order to optimize the cuts for the signal search and to estimate the signal selection efficiency, a particular beyond-Standard-Model signature was used: the leptoquark formation with lepton-flavor violation (see diagrams of Fig. 1.11), as in the Buchmüller-Rückl-Wyler model (described in Sec. 1.3.3). The generator LQGENEP (LeptoQuark GENerator for *ep* scattering) [50] was used to simulate the signal. It is assumed that one of the 14 LQ types dominates. The final state lepton and the initial- and final-state quark generation and the leptoquark type can be chosen by the user. Charged-current like interactions, where the final state lepton is a neutrino, are not considered by the generator, although they are possible for some LQ types. The initial- or final-state quark can be u, d, s, c or b. The combinations with a top quark are not considered since they would give a negligible contribution to the cross section. The QCD cascade and the final hadron formation were simulated with PYTHIA [51].

LFV transitions mediated by leptoquarks with masses between 140 and 300 GeV were simulated in 20 GeV steps. Moreover, LQs with a mass above $\sqrt{s}$, chosen to be $M_{\mathrm{LQ}} = 600\,\mathrm{GeV}$, were simulated for the 14 different LQ types and for all the permitted initial- and final-state quark combinations.

The characteristics of LFV events mediated by a leptoquark are very similar

to NC DIS, except that a μ or a τ lepton is present in the final state instead of the scattered electron. In $e-\mu$ transitions the events are characterized by missing transverse momentum as measured by the calorimeter, due to the fact that muons release only a small amount of their energy in the detector. The missing transverse momentum is therefore in the direction of the muon.

In $e-\tau$ transitions the τ decays too close to the interaction vertex to be detected; therefore only its decay products can be detected. The τ decays in the 17.4% of the cases into $\tau \rightarrow \mu\nu_\tau\nu_\mu$, in the 17.8% of the cases into $\tau \rightarrow e\nu_\tau\nu_e$ and in the other cases into $\tau \rightarrow$ hadrons ν_τ. Due to the presence of at least a neutrino in all the decay channels, also $e-\tau$ transitions are characterized by missing transverse momentum. Since the τ lepton coming from a heavy particle decay has a large momentum, all the particles from the decay are expected to be emitted in the original τ direction. Therefore for the τ decaying into a muon and neutrinos the event topology is very similar to the $e-\mu$ transition. Events with a $\tau \rightarrow e\nu_\tau\nu_e$ are characterized by an electron in the missing transverse momentum vector direction. Finally, if the τ lepton decays into hadrons and ν_τ, a collimated jet is observed in the original τ direction.

3.4 Simulation of background events

3.4.1 Photoproduction

Photoproduction has already been described in Sec. 1.1.4. As already stated, the cross section of these processes is very high; therefore they usually represent a large source of background for beyond-Standard-Model processes. Although the event topology of these events is very different from LFV events, they can contain leptons from the decays of particles inside the jets. Moreover, missing transverse momentum can arise from the finite energy resolution, especially in high transverse energy events.

In order to take into account the photoproduction background contribution in the analysis, both direct and resolved PhP processes were simulated using Herwig 5.9 and Herwig 6.1 [52]. The parton density parametrization CTEQ4D [53] and GRV-G LO [54] were used for the proton and the photon, respectively. Partonic processes and initial- and final-state parton showers were simulated using leading-order matrix elements. The hadronization was simulated using the Cluster model. The signal events have a high transverse energy in the final state. Therefore, in order to reduce the amount of events to be processed, events with low P_t^{hard}, defined as the lower value of the momentum of the two outgoing partons of the hard process, are discarded at the parton level (before the hadronization). The number of final events is further reduced requiring a minimum transverse energy, E_t,

MC sample	Beam $\sqrt{s}$ (GeV)	Cross section (pb)	N. of events	L (pb^{-1})
Direct PhP $P_t^{hard} > 10\,\text{GeV}$ $E_t > 40\,\text{GeV}$	e^+p 300	618.7	100K	161.6
Direct PhP $P_t^{hard} > 2.5\,\text{GeV}$ $E_t > 20\,\text{GeV}$	e^-p 318	1536	120K	78.12
Direct PhP $P_t^{hard} > 20\,\text{GeV}$ $E_t > 40\,\text{GeV}$	e^+p 318	157.8	40K	253.5
Resolved PhP $P_t^{hard} > 10\,\text{GeV}$ $E_t > 40\,\text{GeV}$	e^+p 300	829.1	100K	120.6
Resolved PhP $P_t^{hard} > 2.5\,\text{GeV}$ $E_t > 20\,\text{GeV}$	e^-p 318	7867	420K	53.39
Resolved PhP $P_t^{hard} > 20\,\text{GeV}$ $E_t > 40\,\text{GeV}$	e^+p 318	173.3	40K	230.8

Table 3.1: Monte Carlo samples used for the simulation of photoproduction events.

defined as the scalar sum of the transverse momentum of the final state particles after the hadronization. In Table 3.1 the cross section, the number of events and the integrated luminosity used to simulate photoproduction for the different data samples are reported.

3.4.2 Deep inelastic scattering

Neutral current DIS events are a source of background for the search for LFV $e-\tau$ transitions. Electrons produce a deposit in the calorimeter that can be misidentified with the narrow jets coming from the hadronic τ decays. Moreover, the $\tau \to e\nu_e\nu_\tau$ channel gives events with a topology very similar to NC events except for the missing transverse momentum.

Charged current events are characterized by missing transverse momentum due to the undetected neutrino. They constitute therefore a significant source of back-

MC sample	Beam $\sqrt{s}$ (GeV)	Cross section (pb)	N. of events	L (pb^{-1})
NC $Q^2 > 400\,\mathrm{GeV}^2$	e^+p 300	1097	120K	109.4
NC $Q^2 > 400\,\mathrm{GeV}^2$	e^-p 318	1197	80K	66.83
NC $Q^2 > 400\,\mathrm{GeV}^2$	e^+p 318	1167	120K	102.8
CC $Q^2 > 100\,\mathrm{GeV}^2$	e^+p 300	34.7	20K	576
CC $Q^2 > 100\,\mathrm{GeV}^2$	e^-p 318	71.5	10K	140
CC $Q^2 > 100\,\mathrm{GeV}^2$	e^+p 318	38.1	30K	787

Table 3.2: Monte Carlo samples used for the simulation of neutral current and charged current DIS events.

ground for LFV events.

Neutral current and charged current DIS events were simulated using the generator Lepto 6.5.1 [55] interfaced to Heracles 4.6.1 [56, 57] via Djangoh 1.1 [58]. The initial- and final-state QCD radiation was modeled with Ariadne 4.08 [59] which is based on CDM already described in Sec. 3.1. The hadronization was simulated using Jetset 7.410 [60]. The parton densities were taken from the CTEQ4D [53] parametrization. The NC and CC DIS samples were generated with $Q^2 > 400\,\mathrm{GeV}^2$ and $Q^2 > 100\,\mathrm{GeV}^2$, respectively, as only events at high E_t, i.e. at high Q^2, constitute a background to LFV searches. The used samples are listed in Table 3.2.

3.4.3 Lepton-pair production

Since di-lepton events (see Sec. 1.2.1) contain high momentum leptons in the final state, they also are a source of background for LFV events. Moreover, within this thesis work, an analysis on multi-muon events with high invariant mass has been performed (see Appendix A). The events found in data have been compared with the SM expectations for μ- and τ-pair production.

The MC generator used to simulate the lepton-pair production was Grape-Dilepton 1.1 (GRAce-based generator for Proton-Electron collisions) [61]. The

Process	Cross section (pb)	N. of events	L (pb^{-1})
Elastic e^+e^-	12.6	30000	$2.38 \cdot 10^3$
Quasi-elastic (1) e^+e^-	5.55	10000	$1.80 \cdot 10^3$
Quasi-elastic (2) e^+e^-	0.195	3000	$1.54 \cdot 10^4$
DIS (1) e^+e^-	32.0	40000	$1.25 \cdot 10^3$
DIS (2) e^+e^-	7.91	12000	$1.52 \cdot 10^3$
DIS (3) e^+e^-	6.19	10000	$1.62 \cdot 10^3$
DIS (4) e^+e^-	3.56	5000	$1.40 \cdot 10^3$
Elastic $\mu^+\mu^-$	9.65	30000	$3.12 \cdot 10^3$
Quasi-elastic (1) $\mu^+\mu^-$	4.76	10000	$2.10 \cdot 10^3$
Quasi-elastic (2) $\mu^+\mu^-$	0.146	3000	$2.05 \cdot 10^4$
DIS (1) $\mu^+\mu^-$	12.2	20000	$1.64 \cdot 10^3$
DIS (2) $\mu^+\mu^-$	2.38	5000	$2.10 \cdot 10^3$
DIS (3) $\mu^+\mu^-$	2.16	5000	$2.31 \cdot 10^3$
DIS (4) $\mu^+\mu^-$	1.12	3000	$2.67 \cdot 10^3$
Elastic $\tau^+\tau^-$	5.99	10000	$1.67 \cdot 10^3$
Quasi-elastic (1) $\tau^+\tau^-$	3.41	3000	$8.80 \cdot 10^2$
Quasi-elastic (2) $\tau^+\tau^-$	$9.08 \cdot 10^{-2}$	5000	$5.51 \cdot 10^5$
DIS (1) $\tau^+\tau^-$	4.68	10000	$2.14 \cdot 10^3$
DIS (2) $\tau^+\tau^-$	0.856	3000	$3.50 \cdot 10^3$
DIS (3) $\tau^+\tau^-$	0.818	3000	$3.67 \cdot 10^3$
DIS (4) $\tau^+\tau^-$	0.412	3000	$7.28 \cdot 10^3$

Table 3.3: Monte Carlo samples used for the simulation of lepton pair production in e^+p interactions at 300 GeV center-of-mass energy.

generator, which uses the general tool GRACE to generate the FORTRAN code to calculate the Feynman amplitudes, permits to calculate the di-lepton cross section with the exact matrix elements in the electroweak theory. The calculated processes, $\gamma\gamma$ (Bethe-Heitler), γZ^0, Z^0Z^0, QED Compton and Z^0 on/off shell production, have already been described in Sec. 1.2.1. In the case of the e^+e^- channel, interference effects with the scattered electron are taken into account. Both initial- and final-state radiation can be included. The calculation of the cross section is done by dividing the process into three kinematic regions: elastic, quasi-elastic and DIS. In the elastic events, the proton does not break up: there is no proton remnant and the final state is constituted only by the two final leptons. In quasi-elastic events the proton breaks up into a low-mass state; in DIS the proton breaks up and the

Process	Cross section (pb)	N. of events	L (pb^{-1})
Elastic e^+e^-	13.4	14000	$1.04 \cdot 10^3$
Quasi-elastic (1) e^+e^-	0.219	3000	$1.37 \cdot 10^4$
Quasi-elastic (2)e^+e^-	5.77	6000	$1.04 \cdot 10^3$
DIS (1) e^+e^-	33.3	34000	$1.02 \cdot 10^3$
DIS (2) e^+e^-	8.02	8500	$1.06 \cdot 10^3$
DIS (3) e^+e^-	6.43	6500	$1.01 \cdot 10^3$
DIS (4) e^+e^-	3.70	4000	$1.08 \cdot 10^3$
Elastic $\mu^+\mu^-$	10.2	11000	$1.08 \cdot 10^3$
Quasi-elastic (1) $\mu^+\mu^-$	0.167	3000	$1.80 \cdot 10^4$
Quasi-elastic (2) $\mu^+\mu^-$	4.97	5000	$1.01 \cdot 10^3$
DIS (1) $\mu^+\mu^-$	13.0	14000	$1.08 \cdot 10^3$
DIS (2) $\mu^+\mu^-$	2.66	3000	$1.12 \cdot 10^3$
DIS (3) $\mu^+\mu^-$	2.36	3000	$1.27 \cdot 10^3$
DIS (4) $\mu^+\mu^-$	1.22	3000	$2.46 \cdot 10^3$
Elastic $\tau^+\tau^-$	6.35	6500	$1.02 \cdot 10^3$
Quasi-elastic (1) $\tau^+\tau^-$	0.105	3000	$2.86 \cdot 10^4$
Quasi-elastic (2) $\tau^+\tau^-$	3.56	4000	$1.12 \cdot 10^3$
DIS (1) $\tau^+\tau^-$	5.24	5500	$1.05 \cdot 10^3$
DIS (2) $\tau^+\tau^-$	1.04	3000	$2.88 \cdot 10^3$
DIS (3) $\tau^+\tau^-$	0.950	3000	$3.16 \cdot 10^3$
DIS (4) $\tau^+\tau^-$	0.479	3000	$6.26 \cdot 10^3$

Table 3.4: Monte Carlo samples used for the simulation of lepton pair production in e^-p interactions at 318 GeV center of mass energy.

scattered electron or positron is visible in the detector. The Lorentz invariants used to discriminate between the three regions are the negative four-momentum transfer squared at the proton vertex, Q_p^2 and the invariant mass of the hadronic system, M_{had}:

$$\begin{aligned} Q_p^2 &\equiv -(k - (k' + p_{\ell^+} + p_{\ell^-}))^2, \\ M_{\mathrm{had}}^2 &\equiv ((k + P) - (k' + p_{\ell^+} + p_{\ell^-}))^2, \end{aligned} \tag{3.1}$$

where k, k' and P are the four-momenta of the initial- and final-state electron and of the incoming proton and $p_{\ell^\pm}$ denotes the momentum of one of the final state leptons. The elastic and quasi-elastic processes are defined by:

- $M_{\mathrm{had}}^2 = M_p$ (elastic),

Process	Cross section (pb)	N. of events	L (pb^{-1})
Elastic e^+e^-	13.4	27000	$2.01 \cdot 10^3$
Quasi-elastic (1) e^+e^-	0.219	3000	$1.37 \cdot 10^4$
Quasi-elastic (2) e^+e^-	5.77	12000	$2.08 \cdot 10^3$
DIS (1) e^+e^-	32.7	66000	$2.02 \cdot 10^3$
DIS (2) e^+e^-	8.27	17000	$2.06 \cdot 10^3$
DIS (3) e^+e^-	6.48	13000	$2.01 \cdot 10^3$
DIS (4) e^+e^-	3.64	7500	$2.06 \cdot 10^3$
Elastic $\mu^+\mu^-$	10.2	21000	$2.06 \cdot 10^3$
Quasi-elastic (1) $\mu^+\mu^-$	0.167	3000	$1.80 \cdot 10^4$
Quasi-elastic (2) $\mu^+\mu^-$	4.97	10000	$2.01 \cdot 10^3$
DIS (1) $\mu^+\mu^-$	13.0	26000	$2.00 \cdot 10^3$
DIS (2) $\mu^+\mu^-$	2.68	5500	$2.05 \cdot 10^3$
DIS (3) $\mu^+\mu^-$	2.37	5000	$2.11 \cdot 10^3$
DIS (4) $\mu^+\mu^-$	1.21	3000	$2.48 \cdot 10^3$
Elastic $\tau^+\tau^-$	6.35	13000	$2.05 \cdot 10^3$
Quasi-elastic (1) $\tau^+\tau^-$	0.105	3000	$2.86 \cdot 10^4$
Quasi-elastic (2) $\tau^+\tau^-$	3.56	7500	$2.11 \cdot 10^3$
DIS (1) $\tau^+\tau^-$	5.23	11000	$2.10 \cdot 10^3$
DIS (2) $\tau^+\tau^-$	1.05	3000	$2.86 \cdot 10^3$
DIS (3) $\tau^+\tau^-$	0.951	3000	$3.15 \cdot 10^3$
DIS (4) $\tau^+\tau^-$	0.478	3000	$6.28 \cdot 10^3$

Table 3.5: Monte Carlo samples used for the simulation of lepton pair production in e^+p interactions at 318 GeV center of mass energy.

- $Q_p^2 < Q_{\mathrm{min}}^2$ or $M_p + M_{\pi^0} < M_{\mathrm{had}} < M_{\mathrm{cut}}$ (quasi-elastic).

The variables M_p and M_{π^0} are the masses of the proton and of the π^0; Q_{min}^2 is set to $1\,\mathrm{GeV}^2$ and M_{cut} to 5 GeV in the generated samples. These two processes differ only in the treatment of the proton vertex [61] and in the simulation of the hadronic final state. The DIS processes, defined by the kinematic region $Q_p^2 > Q_{\mathrm{min}}^2$ and $M_{\mathrm{had}} > M_{\mathrm{cut}}$, are simulated using the parton density CTEQ5L [62] at the Q_p^2 scale. The simulation of the proton remnant, of the final-state radiation and of the hadronization is performed by PYTHIA [51] using the parton shower model and the Lund string model. The Drell-Yan process is not included in the simulation, as it gives a negligible contribution.

In Tables 3.3, 3.4 and 3.5 the di-lepton MC generated events are listed.

3.5 Detector response simulation

In order to compare the MC with data it is necessary that the generated MC events are passed through the simulation of the ZEUS detector. This is done by the MOZART program, based on the GEANT 3.13 [63] package. MOZART simulates the response of the different detector components taking into account the geometric acceptance and the effect of dead material. The simulation of each component was initially optimized during test-beam measurements, but the program is continuously updated and improved with performance studies of the ZEUS running experiment. The output of MOZART is passed to ZGANA, which simulates the trigger behavior. The same program ZEPHYR is used to reconstruct both Monte Carlo and real events. ZEPHYR contains the event reconstruction routines for the different components, including the calibration corrections. The final events (both MC and data) are then organized using the ADAMO [64] data management system. The same analysis program used to analyze the data, is also used to study the Monte Carlo events.

Chapter 4

Reconstruction

In this chapter the description of the reconstruction of the physical objects (tracks, electrons, muons, jets and τ leptons) is given. This information was partly obtained using standard ZEUS libraries and partly it has been implemented in the analysis framework.

4.1 Track and vertex reconstruction

Tracks are reconstructed from CTD hits [65]. The vertex is reconstructed from the information on the fitted tracks. Tracks too far from the vertex are discarded; the surviving tracks are constrained to pass through the reconstructed vertex and their parameters are then re-calculated. The charge of the tracks is determined from the sign of their curvature. Only tracks with transverse momentum $p_t^{\rm trk} > 100$ MeV were considered in the analysis.

4.2 The calorimeter variables

The global calorimeter variables are calculated starting from the information regarding the cells. Isolated cells with energy below the noise thresholds, i.e. 80 MeV for electromagnetic cells and 140 MeV for hadronic cells, are discarded. Other corrections are included by removing the known noisy cells and applying to isolated cells a cut on the energy imbalance from the two photomultipliers (see Sec. 2.4). The energy scale of the calorimeter is calibrated requiring a transverse energy balance between the scattered electron and the jet in NC high Q^2 events. The energy responses in data and MC are then compared and additional corrections, due to inaccuracy of the dead material simulation, are applied. The correction factors, summarized in Table 4.1, depend on the calorimeter sector and on the cell type and

CAL sector	Cell type	Correction 1994–1997	Correction 1998–2000
FCAL	EMC	4%	2.4%
	HAC	−5%	−6%
BCAL	EMC	4%	5%
	HAC	8%	10%
RCAL	EMC	2.2%*	2.2%*
	HAC	2.2%*	2.2%*

Table 4.1: Energy scale corrections for different calorimeter regions. The corrections for the 1994–1997 and 1998–2000 running periods differ slightly. The correction factor for RCAL (denoted with a $*$) is an average value since the correction is done cell by cell.

they are applied only to data. After the corrections the uncertainty on the energy scale is 1% in FCAL, and 2% in BCAL and RCAL.

The energy measured in the calorimeter is lower with respect to the real value, because of the energy loss in the inactive material in front of the calorimeter, which corresponds to $1 \div 3$ radiation lengths, depending on the region. Further sources of error in the energy measurement are the non uniformity of the cell response and the "backsplash" due low-energy neutral particles emitted by high-energy showers in FCAL and detected in BCAL or RCAL. Such effects are taken into account in the reconstruction of the calorimeter variables.

Given E_i the energy measured in the i^{th} cell of the calorimeter after corrections, the total calorimeter four-momentum (E, P_X, P_Y, P_Z) can be defined as:

$$\begin{aligned} E &= \sum_i E_i \\ P_X &= \sum_i E_i \sin\theta_i \cos\phi_i \\ P_Y &= \sum_i E_i \sin\theta_i \sin\phi_i \\ P_Z &= \sum_i E_i \cos\theta_i, \end{aligned} \tag{4.1}$$

where θ_i and ϕ_i are the cell angles in a spherical coordinate system, centered in the reconstructed event vertex. The calorimeter transverse momentum, can be therefore written as $P_t = \sqrt{P_X^2 + P_Y^2}$.

Another variable widely used at HERA is $E - P_Z = \sum_i E_i(1 - \cos\theta_i)$ which, in the initial state, is equal to $2E_e$, E_e being the energy of the incoming electron

beam. For energy conservation, if all the particles in the final state are detected by the calorimeter, $P_t \simeq 0$ and $E - P_Z \simeq 55\,\mathrm{GeV}$. The quantity $E - P_Z$ is not sensitive to particles escaping the forward beam pipe, like the proton remnant. On the other hand if the electron is scattered off at small angle and it is, thus, not detected in the calorimeter, as it happens in photoproduction events, $E - P_Z$ has low values.

The total transverse energy, E_T is defined as the scalar sum of the transverse energies of the calorimeter cells: $E_T = \sum_i E_i \sin\theta_i$.

4.3 Electron identification

The scattered electron identification is based on the fact that electrons or positrons, after being detected in the tracking detectors, release all their energy in the electromagnetic calorimeter. Here and later the term electron will refer to both electron and positrons, as the analysis does not distinguish between the two.

In this analysis the electron identification was performed using the EM electron-finder [66]. The algorithm consists of three steps.

First of all, cells with a local energy maximum are found and grouped to form a "cluster" together with the surrounding cells which have an energy deposit above the noise. Each cluster is treated as an electron candidate. The center of the cluster is obtained by weighting each tower of the cluster with a logarithmic function of the energy deposit. The polar angle of the cluster is calculated using the reconstructed vertex as center of the coordinate system. If the candidate electron is within the CTD acceptance, a matching track with $p_T^{\mathrm{trk}} > 0.1\,\mathrm{GeV}$ and distance of closest approach (DCA) to the beam line less then 2 cm is required. The DCA between the cluster and the extrapolation of the track to the calorimeter has to be lower than 50 cm.

In the second step, seven variables are calculated for each electron candidate. Four of them are related to the calorimeter energy deposit: the fraction of energy in the HAC layers, two parameters related to the lateral energy profiles, and the total energy of the calorimeter cells not associated with the cluster but lying within a cone in pseudo-rapidity η and azimuthal angle ϕ of radius $R = \sqrt{(\Delta\eta)^2 + (\Delta\phi)^2} = 0.8$, centered on the cluster. The last three parameters, which are used for the matching with the track, are the polar and azimuthal difference between the track and the cluster position and the quantity $1/E_{\mathrm{clu}} - 1/p^{\mathrm{trk}}$, being E_{clu} the energy of the cluster and p^{trk} the track momentum.

Finally, for each of the seven variables, a sub-probability is derived. The probabilities are then combined into a global probability, P_e, assuming that the variables are non correlated. If the electron candidate is outside the CTD acceptance or if it has no matching track, only the calorimeter variables are taken into account to

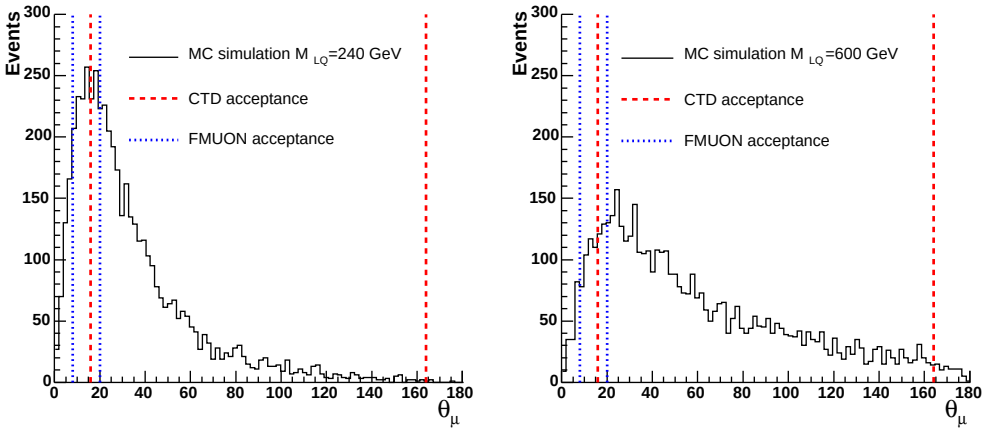

Figure 4.1: Simulated polar angle distribution of the muons from a LFV interaction mediated by a scalar LQ with (a) $M_{LQ} = 240\,\text{GeV}$ and (b) $M_{LQ} = 600\,\text{GeV}$. The region between the dashed lines and the dotted lines represents the CTD and the FMUON acceptance, respectively.

calculate the P_e. The global probability has values between 0 and 1 and it is higher for real electron candidates.

The electron energy is taken to be equal to the cluster energy since the CAL energy resolution is better than the CTD momentum resolution for tracks with $p^{\text{trk}} > 10\,\text{GeV}$. The electron candidate polar and azimuthal angles are determined from the associated track or, in absence of it, from the calorimeter cluster position.

4.4 Muon identification

Muons, unlike electrons and hadrons, release only a small quantity of their energy in the calorimeter and are detected in the muon chambers. There are several muon-finding algorithms based on the matching between the CTD track and the muon chamber track or between the CTD track and an energy deposit in the calorimeter compatible with a minimum ionizing particle (MIP).

Since LFV events with a muon in the final state have a topology much different as compared to the Standard Model processes, the background for this search is expected to be very low. Therefore an algorithm which gives a high efficiency even with a lower purity was employed. The muon identification used two different methods, in two different angular regions, for the final-state μ candidate.

The first method was used in the polar angle range $15° < \theta < 164°$, which corresponds to the CTD acceptance, and it is based on the matching between a

CTD track with $p_T^{trk} > 2\,\text{GeV}$ and a MIP deposit in the calorimeter. The track is required to have a distance of closest approach less then 30 cm to the MIP and no other track has to be found with a DCA lower than 100 cm to the MIP. The momentum and the direction of the muon were obtained from the CTD track.

This method was also used in the multi-muon search described in Appendix A.

As it can be seen in Fig. 4.1, especially when the LQ is produced as a resonance, a considerable fraction of the muons lies outside the CTD acceptance. The forward region is not covered by the CTD; moreover, since most of the particles are boosted into the proton direction, it is more difficult to isolate the muon energy deposit in the calorimeter. Therefore, very forward muons ($8^\circ < \theta < 20^\circ$) were identified requiring a reconstructed track in the FMUON detector with hits in at least 5 detector planes.

4.5 The jet finder algorithm

Jets were identified in this analysis using the so called inclusive k_T-cluster algorithm [67] which is the jet algorithm most used at HERA. Such algorithm consists of the following steps:

1. the starting point is a list of calorimeter objects; calorimeter cells above an energy threshold of 100 MeV for the electromagnetic section and 150 MeV for the hadronic section are used;

2. for each object i, the distance from the direction of the proton beam defined as $d_i = E_{Ti} \cdot R_0$ is calculated; the quantity R_0 is usually set to 1 and $E_{Ti} = E_i \sin\theta_i$;

3. the distance d_{ij} between two objects is evaluated as:

$$d_{ij} = \min[E_{Ti}, E_{Tj}] \cdot ((\eta_i - \eta_j)^2 + (\phi_i - \phi_j)^2);$$

4. if the smallest of all the d_i and d_{ij} quantities is a d_{ij}, the two objects i and j are grouped into a new object k with E_{Tk}, η_k, ϕ_k following the sum criteria:

$$\begin{aligned} E_{Tk} &= E_{Ti} + E_{Tj}, \\ \eta_k &= \frac{E_{Ti}\eta_i + E_{Tj}\eta_j}{E_{Ti} + E_{Tj}}, \\ \phi_k &= \frac{E_{Ti}\phi_i + E_{Tj}\phi_j}{E_{Ti} + E_{Tj}}; \end{aligned} \tag{4.2}$$

5. if the smallest of all the d_i and d_{ij} quantities is a d_i, the i object is removed from the list of particles and added to the list of jets;

6. the procedure ends when no particle is left in the list of objects.

The transverse energy, the pseudo-rapidity and the azimuthal angle of the jets are defined as:

$$\begin{aligned} E_T^{jet} &= \sum_i E_{Ti}, \\ \eta^{jet} &= \frac{\sum_i E_{Ti}\eta_i}{\sum_i E_{Ti}}, \\ \phi^{jet} &= \frac{\sum_i E_{Ti}\phi_i}{\sum_i E_{Ti}}. \end{aligned} \tag{4.3}$$

Only jets in the pseudo-rapidity range $-1 < \eta_{\text{jet}} < 2.5$ and with a transverse energy of at least 5 GeV were considered.

The energy of the jets, as measured in the calorimeter, is usually lower than the true energy of the jet reconstructed from the hadrons at the generator level. This loss of energy is mainly due to the presence of dead material before the CAL. Correction factors were applied to the transverse energy of the jet both for data and Monte Carlo. The correction factors depend on the E_T and on the η of the jet and are obtained from a study of jets in simulated CC DIS events comparing the calorimeter reconstructed energy with the sum of the energies of the hadrons of the jets at the generator level [68].

4.6 The τ finder

Tau identification is usually more critical with respect to the other charged leptons. Unlike the muon, the τ lepton, because of its mass of 1776.99 MeV, can decay into hadrons. The leptonic decay channels ($\tau \to e\nu_e\nu_\tau$ and $\tau \to \mu\nu_\mu\nu_\tau$) represent only the 35% of the τ decays. In almost 65% of the cases the τ decays into one (1-prong), three (3-prong) charged hadrons ($\pi^\pm$ or $K^\pm$), a ν_τ and zero or more neutral hadrons (mainly π^0 or K^0). The mean life time of the τ is $\tau_\tau = 290.6 \times 10^{-15}$ s and corresponds to $c\tau = 87.11$ μm. The secondary vertex produced by the decay of the τ is therefore too close to the primary interaction vertex to be resolved by the ZEUS detector.

Hadrons from τ decays can be observed as a jet in the calorimeter. In order to identify the τ leptons, an algorithm which distinguishes between the jets coming from hadronic τ decays and the QCD jets coming from quark or gluon radiation was employed. The algorithm exploits the fact that high-energy QCD jets usually

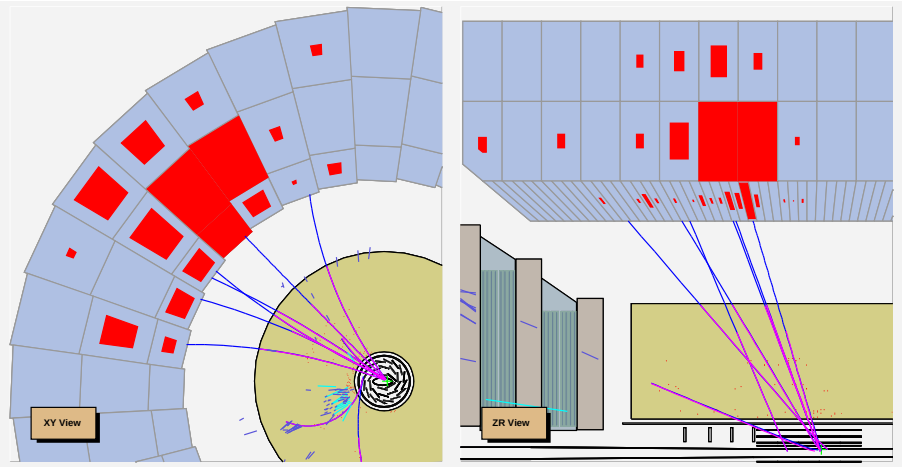

Figure 4.2: Event display of a charged current DIS event from data, showing a QCD jet.

have higher multiplicity and a larger internal transverse momentum than those from the decay products of the τ. If the τ lepton has a high momentum, which is the case of this analysis, its decay products are boosted into the τ direction. Moreover, the color neutrality of the τ inhibits the quark and the gluon radiation. Therefore the energy deposits in the calorimeter are expected to have a narrow shape. On the other hand, QCD jets can radiate gluons in the fragmentation phase and are connected by the color charge to the rest of the event, leading to a greater spread of the energy deposit in the calorimeter. In Fig. 4.2 a QCD jet from a CC DIS data event is shown. A simulated jet arising from a hadronic τ decay is shown in Fig. 4.3.

4.6.1 Jet observables

The k_T-cluster algorithm in the inclusive mode was used to identify jets. The jet transverse energy was corrected for losses due to the dead material, as described in the previous section. The observables used to discriminate jets are based on the jet shape and rely only on the calorimeter energy and position measurements. The following quantities are used:

- the first moment of the radial extension of the jet:

$$R_{\text{mean}} = \langle R \rangle = \frac{\sum_i E_i \cdot R_i}{\sum_i E_i},$$

  where the sums run over the calorimeter cells associated to the jet and E_i is

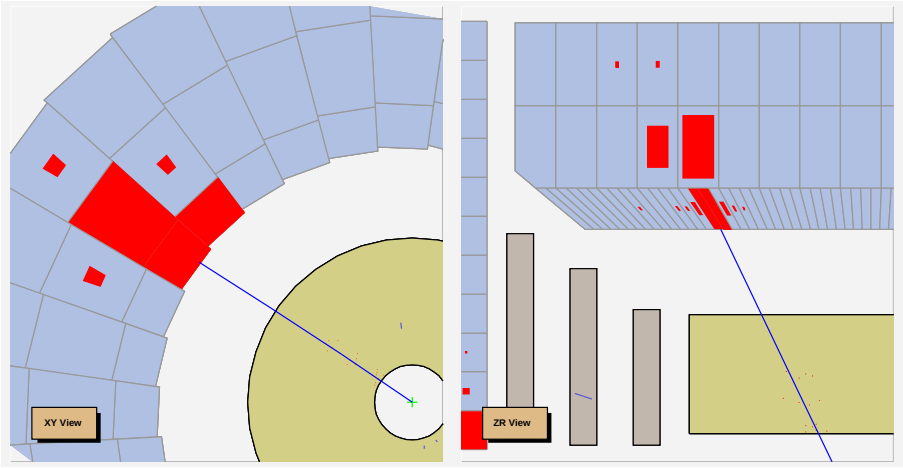

Figure 4.3: Event display of a simulated event in ZEUS showing the response to a jet arising from a hadronic decay of a τ. The event comes from the simulation of a LFV interaction, mediated by a LQ with mass of 240 GeV.

the energy of the i^{th} cell; the variable R_i is defined as $R_i = \sqrt{(\Delta\phi_i)^2 + (\Delta\eta_i)^2}$, where $\Delta\phi_i$ ($\Delta\eta_i$) is the difference between the azimuthal angle (pseudo-rapidity) of the i^{th} calorimeter cell, and the jet axis;

- the second moment of the radial extension of the jet:

$$R_{\text{rms}} = \sqrt{\frac{\sum_i E_i(\langle R\rangle - R_i)^2}{\sum_i E_i}},$$

- the first moment of the projection of the jet onto its axis:

$$L_{\text{mean}} = \langle L\rangle = \frac{\sum_i E_i \cdot \cos\alpha_i}{\sum_i E_i},$$

where α_i is the angle between the cell i and the jet axis;

- the second moment of the projection of the jet onto its axis:

$$L_{\text{rms}} = \sqrt{\frac{\sum_i E_i(\langle L\rangle - \cos\alpha_i)^2}{\sum_i E_i}},$$

- the number of sub-jets (N_{subj}) within the jet resolved with a resolution-criterion y_{cut} of $5 \cdot 10^{-4}$ [69, 70]; the number of sub-jets is evaluated using the k_T-cluster algorithm: the smaller the y_{cut}, the higher the resolution power and the more sub-jets can be resolved in a jet;

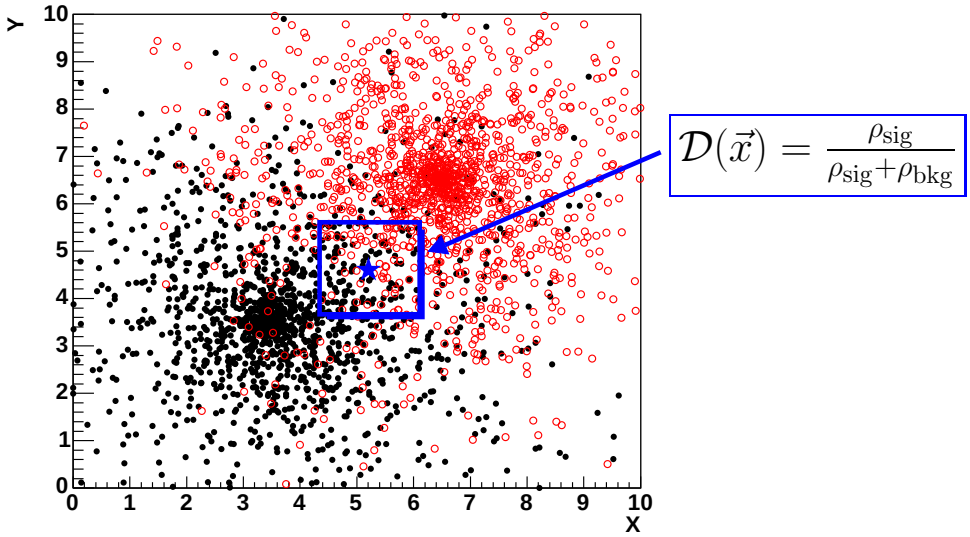

Figure 4.4: Example of discriminant calculation in a 2-dimensional space (X,Y). Dots (•) and open dots (○) represent the two classes of events to be classified.

- the invariant mass ($M_{\rm jet}$) of the jet calculated from the calorimeter cells associated with the jet; the particles of the jets are assumed to be massless.

4.6.2 Discriminant

A technique for τ identification [71] was developed for a previous study [2] in which a small number of isolated τ events were found in a data set identical to that used in this work. In order to separate the signal from the background, the six variables described in the previous section were combined into a discriminant $\mathcal{D}$, given, for any point in the phase space $\vec{x}(\log(R_{\rm mean}), \log(R_{\rm rms}), \log(1 - L_{\rm mean}), \log(L_{\rm rms}), N_{\rm subj}, M_{\rm jet})$, by:

$$\mathcal{D}(\vec{x}) = \frac{\rho_{\rm sig}(\vec{x})}{\rho_{\rm sig}(\vec{x}) + \rho_{\rm bkg}(\vec{x})}, \tag{4.4}$$

where $\rho_{\rm sig}$ and $\rho_{\rm bkg}$ are the density functions of the signal and the background, respectively. Figure 4.4 shows an example of discriminant calculation for a 2-dimensional case. The $\rho_{\rm sig}$ and $\rho_{\rm bkg}$ densities, sampled with MC simulations, were calculated using a method based on range searching [72, 73]. A binary tree structure was used to store the information about the quantities employed to calculate the discriminant for the signal and the background samples. Lepton-flavor-violating events in which the final-state τ decays into hadrons and a neutrino were used to

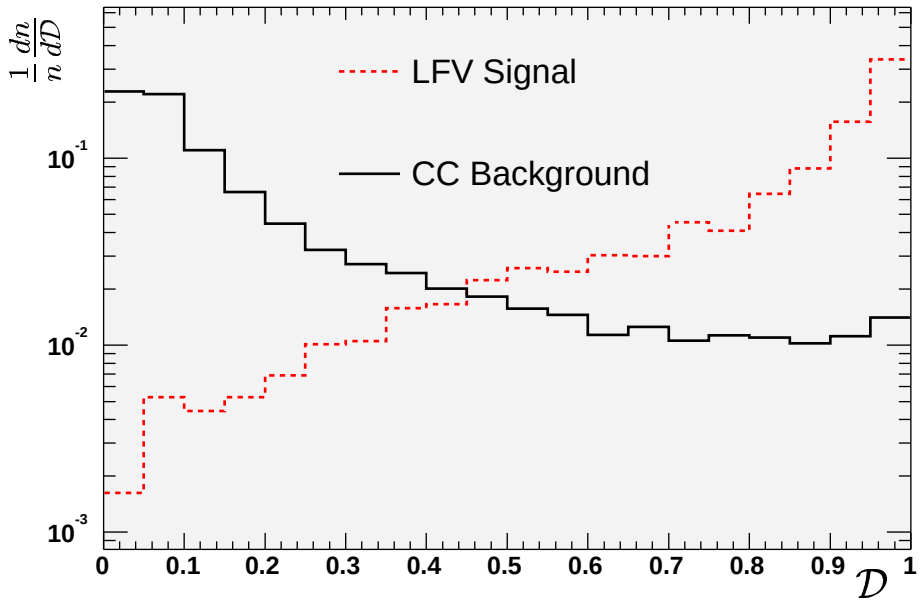

Figure 4.5: Comparison between the $\mathcal{D}$ value for CC DIS jets and for signal jets. For each event only the jet with maximum value of $\mathcal{D}$ is considered. The MC used for the signal was LFV ($e \to \tau$) mediated by LQ with $M_{\mathrm{LQ}} = 240\,\mathrm{GeV}$. Only events with τ decaying into hadrons and in the CTD acceptance ($15° < \theta < 164°$) were considered as signal.

simulate the signal. The background simulation was based on CC DIS MC events. For the signal, only jets coming from the τ decays were considered. Jets outside the CTD acceptance, $15° < \theta < 164°$, were not included in the binary tree. Further requirements on the characteristics of the jets and of the events, based on the selection cuts used in the analysis, were added in order to decrease the number of jets to be considered. For any given jet with phase space coordinates $\vec{x}$, the signal and the background densities were evaluated from the number of corresponding simulated signal and background jets in a 6-dimensional box of fixed size centered around $\vec{x}$. The τ signal tends to have a large discriminant value ($\mathcal{D} \to 1$) while the CC DIS background has a low discriminant value ($\mathcal{D} \to 0$) as it can be seen in Fig. 4.5. In order to obtain a better discrimination the boxes have to be sufficiently small. On the other hand, in order to classify the jet, a statistically significant number of MC events inside the box is needed. It is therefore critical to have enough MC statistics. In this analysis $\sim$ 40K signal and background events were used. Jets with a box containing less than 15 events were not classified. The use of logarithmic variables minimizes the amount of regions which are rarely populated.

Chapter 5

Search for $e \longrightarrow \mu$ transitions

This chapter contains the description of the search strategy for lepton-flavor-violating events in which the final-state lepton is a muon. The search is sensitive to any process with a final-state topology where the scattered electron of ep NC DIS is replaced by a μ. However, in the final selection the cuts were optimized for LFV processes mediated by a LQ.

After applying trigger requirements and additional cuts to reject non-ep background, the analysis consists of a preselection and a final selection. The first is designed to select events with high-momentum isolated muons and, thus, to reduce the background to a very low level. In the final selection cuts obtained by optimization studies were applied. The same cuts were applied to both data and Monte Carlo simulations.

5.1 Trigger requirements and rejection of non-ep background

Trigger level selection

The signature of $e-\mu$ LFV events is an isolated muon with high transverse momentum, which is balanced by that of a jet in the transverse plane. An apparent missing transverse momentum, measured by the calorimeter, due to the penetrating muon is expected. The missing transverse momentum is a characteristic also of CC DIS events, where the final-state neutrino is undetected. Therefore, the trigger used in this analysis is the same as the charged current trigger (so called DST bit 34). Such trigger is based on a cut on $\not{P}_t$ with a threshold lower than that used in the offline analysis; in particular it is required that $\not{P}_t > 7\,\mathrm{GeV}$ and $P_t^{\mathrm{ex1IR}} > 6\,\mathrm{GeV}$, where P_t^{ex1IR} is the missing momentum measured in the calorimeter cells that are not in

the inner ring of FCAL. This requirement is needed to avoid the inclusion of proton beam-gas events, which usually deposit a big amount of energy in FCAL close to the beampipe region. In addition a reconstructed vertex is required to suppress non-ep events (so called DST bit 10).

A detailed description of the DST34 and DST10 trigger bits is given in Appendix B.

Cosmic rejection

Events triggered by high-energy muons passing through the detector contain usually two high-energy tracks with an opening angle of almost 180°. In order to exclude such background, events with less than 10 tracks and with any two tracks satisfying the condition $\cos\Omega < -0.997$, where Ω is the opening angle between the two tracks, were rejected.

Cosmics events can be excluded also exploiting the timing information from the calorimeter. The cells in the CAL provide timing information with a resolution of approximately 1 ns. All the cells are calibrated so that, for particles coming from the nominal interaction point, the timing is around 0 ns. Events with $|t_b| > 5$ ns, where t_b is the average timing in BCAL are excluded. This cut was applied if the total energy measured in BCAL exceeded a threshold of 4 GeV. Since the timing is not well simulated in the Monte Carlo, this cut was imposed only on data events.

Beam-gas rejection

Events originating from proton-beam-gas interactions usually have a large number of low-energy tracks associated to secondary vertices. Therefore the events were selected if at least 5% of the recontructed tracks comes from the interaction vertex and has a transverse momentum $p_t^{\mathrm{trk}} > 0.3\,\mathrm{GeV}$.

5.2 Preselection

As anticipated in Sec. 4.4, the muon identification comprises two different methods, in two different angular regions, for the final-state μ candidate. For muon candidates in the polar-angle range $15° < \theta < 164°$, the following additional conditions were required:

- $D_{\mathrm{trk}} > 0.5$ and $D_{\mathrm{jet}} > 1$ where D_{trk} (D_{jet}) is the distance in the $\eta - \phi$ plane between the track associated with the candidate muon and the closest track (jet) to the candidate; only tracks with a $p_t^{\mathrm{trk}} > 0.2\,\mathrm{GeV}$ and associated to a vertex were considered; this cut was applied to select well isolated muons;

		Events
MC	Di-μ	22.8±0.8
	Di-τ	1.5±0.2
	Photoproduction	1.6±0.7
	Total expected	25.9±1.1
DATA		20

Table 5.1: Number of events expected from SM process simulations after the preselection compared with the events remaining in the data sample.

- candidate muons in the polar-angle region $115^\circ < \theta < 130^\circ$ were excluded to eliminate background from electrons that lose much of their energy in the dead material at the transition between BCAL and RCAL; these electrons could give missing P_t and could be misidentified as muons.

The second method was used for very forward muons ($8^\circ < \theta < 20^\circ$) and required a reconstructed track in the FMUON detector as described in Sec. 4.4.

After the trigger requirements and the non-ep background related cuts described in the previous section, the following cuts were applied:

- a reconstructed vertex with $|Z_{\rm vtx}| < 50\,{\rm cm}$; this cut was used to reduce further non-ep background contribution;

- a missing transverse momentum $\not{P}_t > 15\,{\rm GeV}$; this cut reduces NC and photoproduction background;

- no electron candidate with energy larger than 10 GeV and $P_e > 0.01$ (defined in Sec. 4.3); this cut was used to suppress NC DIS processes in a region of potentially high background and negligible anticipated signal;

- a muon candidate (as described before) in the direction of the $\not{P}_t$ ($\Delta\phi < 20^\circ$, where $\Delta\phi$ is the difference between the azimuthal angles of the candidate muon and of the $\not{P}_t$ vector); this cut reduces NC and CC background, which have no muon in the final state, as well as di-muon events in which the candidate muon direction is not necessarily aligned with the $\not{P}_t$ vector.

After the preselection, the sample contained 20 data events, while 25.9 ± 1.1 were expected from SM MC, mainly from QED di-muon processes. In Table 5.1 the contribution to the background from the different SM processes, estimated from Monte Carlo simulation, are summarized. One of the events selected in data is shown in Fig. 5.1.

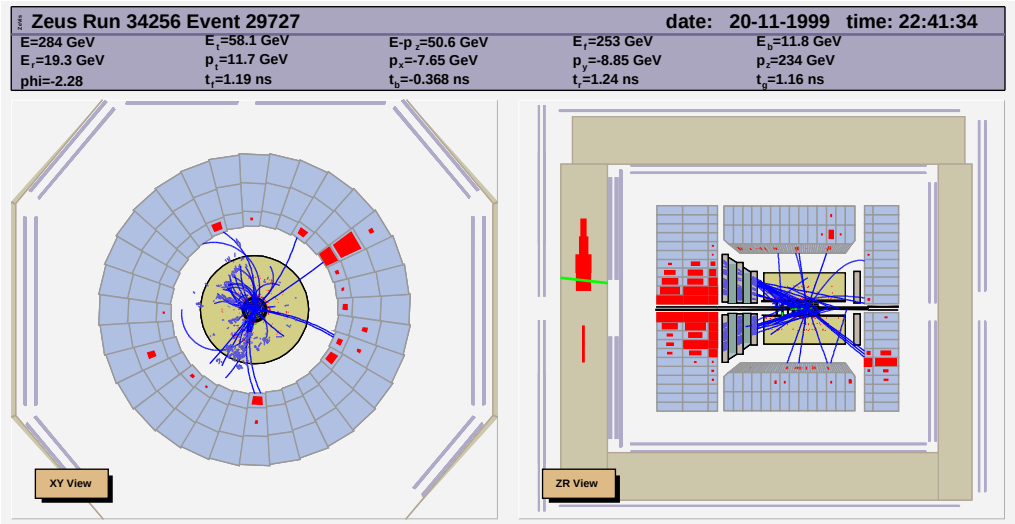

Figure 5.1: Example of event in 1999–2000 data selected by the preselection cuts.

5.3 Optimization of the cuts and final selection

The cuts for the final selection were designed by optimizing the sensitivity using signal and background simulations. In general, the tagging of lepton-flavor-violation interactions mediated by a LQ with $M_{\mathrm{LQ}} \gg \sqrt{s}$ has a lower efficiency with respect to low-mass LQ, especially when high generation quarks are involved in the initial- or final-state. For this reason a scalar LQ with a mass of 600 GeV, coupling to second generation quarks, was taken as signal in the cut optimization studies. Neutral current and charged current DIS, photoproduction and di-lepton MC for 1999–2000 e^+p data (see Tables 3.1–3.5) were used as background.

The following variables were used in the optimization studies:

- the missing transverse momentum, $\not{P}_t$;
- the quantity $\not{P}_t/\sqrt{E_t}$; this variable was chosen to reject high-E_t neutral current DIS and photoproduction events, where the small apparent $\not{P}_t$ can arise from the finite energy-measurement resolution;
- $E - P_Z + \Delta_\mu$, where $\Delta_\mu = \not{P}_t(1 - \cos\theta_\mu)/\sin\theta_\mu$, θ_μ being the polar angle of the candidate muon; the quantity Δ_μ represents the contribution to $E - P_Z$ carried by the muon, assuming that the transverse momentum of the muon is $\not{P}_t$; for signal events, where the $\not{P}_t$ arises only from the presence of final-state muon, this quantity should be peaked at about 55 GeV; this variable is used to reject di-muon events or events with a fake candidate muon.

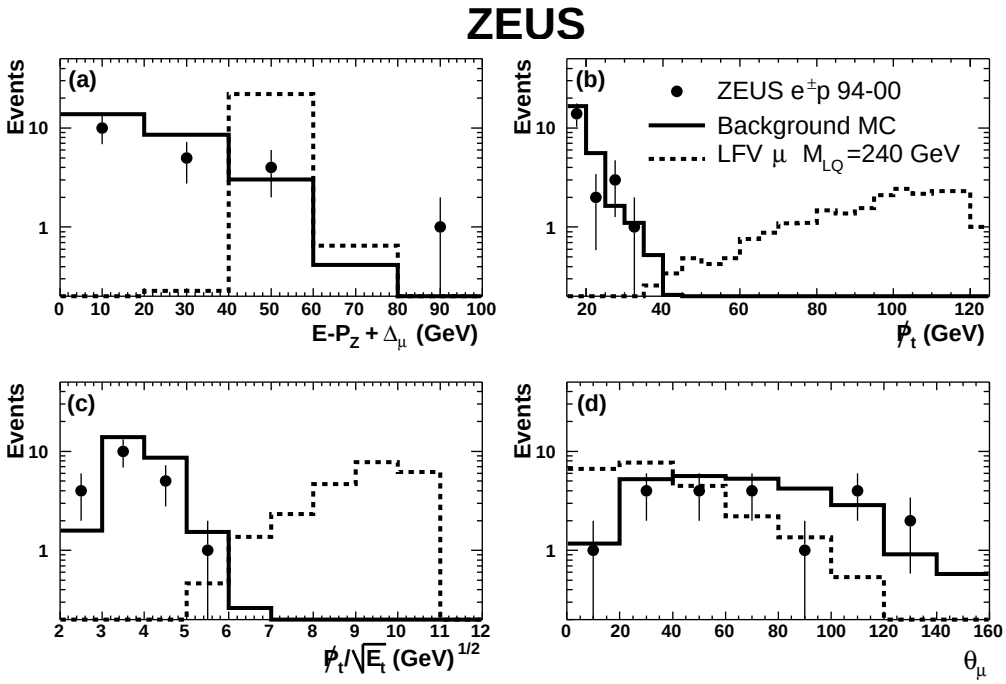

Figure 5.2: Comparison between data (dots) and SM MC (solid line): (a) $E - P_Z + \Delta_\mu$, (b) $\not{P}_t$, (c) $\not{P}_t/\sqrt{E_t}$ and (d) polar angle of the muon, θ_μ, after the μ-channel preselection. The dashed line represents the LFV signal with an arbitrary normalization.

Figure 5.2 shows the comparisons between data and MC expectations after the preselection for the variables used in the cut optimization and for the polar angle of the muon. The agreement between the data and SM background is good.

The optimization of the cuts is made by minimizing the Bayesian cross section upper limit for the signal in presence of background, assuming no signal [74]. If all the observed events $N_{\rm obs}$ are assumed to originate from the background, $N_{\rm obs}$ is expected to follow a Poisson distribution, $P(N_{\rm obs}, N_{\rm bkg})$, where $N_{\rm bkg}$ is the number of background events expected from a Monte Carlo simulation. The 95% confidence level (CL) upper limit on the signal, $N_{\rm lim}$, can be computed by numerical inversion of:

$$1 - \mathrm{CL} = \frac{e^{-N_{\rm lim}} \sum_{n=0}^{N_{\rm obs}} \frac{(N_{\rm bkg}+N_{\rm lim})^n}{n!}}{\sum_{n=0}^{N_{\rm obs}} \frac{N_{\rm bkg}^n}{n!}}. \tag{5.1}$$

The expectation value of $N_{\rm lim}$ is obtained by summing over all possible values of

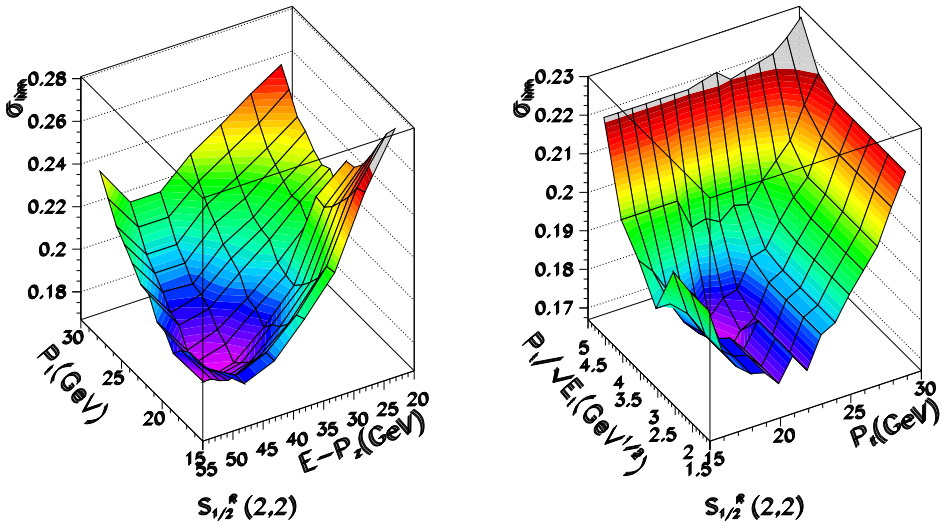

Figure 5.3: Values of $\langle\sigma_{\text{lim}}\rangle$ as a function of $\not{P}_t$ and $E - P_Z$ (left) and $\not{P}_t/\sqrt{E_t}$ and $\not{P}_t$ (right). A LFV interaction mediated by a $S^R_{1/2}$ LQ with $M_{LQ} = 600\,\text{GeV}$ and coupling to second generation quarks was taken as signal.

N_{obs}:

$$\langle N_{\text{lim}}\rangle = \sum_{N_{\text{obs}}=0}^{\infty} P(N_{\text{obs}}, N_{\text{bkg}}) \cdot N_{\text{lim}}(N_{\text{obs}}, N_{\text{bkg}}). \tag{5.2}$$

The expectation value of the cross section upper limit is then given by:

$$\langle\sigma_{\text{lim}}\rangle = \frac{\langle N_{\text{lim}}\rangle}{\varepsilon L}, \tag{5.3}$$

where ε is the signal selection efficiency and L is the integrated luminosity. The optimization was done by varying the cuts on the variables $\not{P}_t$, $\not{P}_t/\sqrt{E_t}$ and $E - P_Z + \Delta_\mu$. Both ε and N_{bkg} depend on the chosen cuts. In Fig. 5.3 the values of $\langle\sigma_{\text{lim}}\rangle$ as a function of $\not{P}_t$ and $E - P_Z$ (left), and $\not{P}_t/\sqrt{E_t}$ and $\not{P}_t$ (right) are shown. A minimum of $\langle\sigma_{\text{lim}}\rangle$ can be clearly seen in both the surfaces. The optimal values for the cuts in the final selection were:

- $\not{P}_t > 20\,\text{GeV}$;
- $\not{P}_t/\sqrt{E_t} > 3\sqrt{\text{GeV}}$;
- $E - P_Z + \Delta_\mu > 45\,\text{GeV}$.

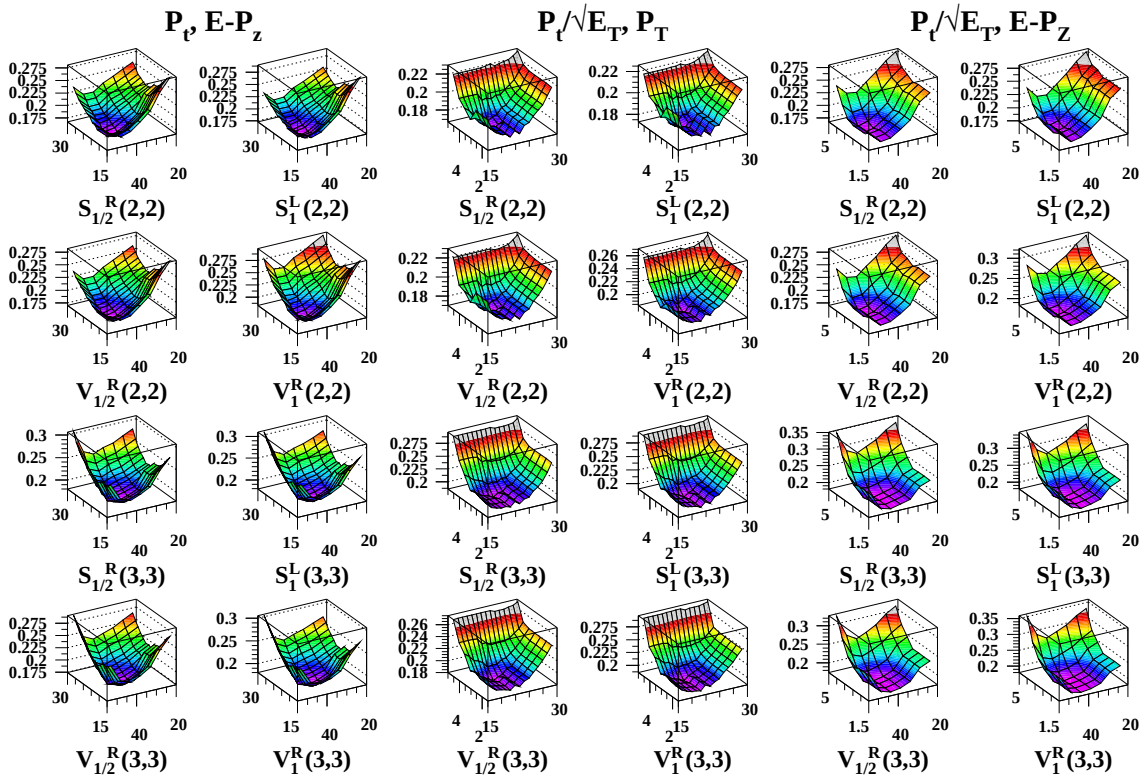

Figure 5.4: Values of $\langle \sigma_{\mathrm{lim}} \rangle$ as a function of $\not{P}_t$ and $E - P_Z$ (first two columns), of $\not{P}_t/\sqrt{E_t}$ and $\not{P}_t$ (3$^{\mathrm{rd}}$ and 4$^{\mathrm{th}}$ columns) and of $\not{P}_t/\sqrt{E_t}$ and $E - P_Z$ (5$^{\mathrm{th}}$ and 6$^{\mathrm{th}}$ columns). LFV interactions mediated by scalar (1$^{\mathrm{st}}$ and 3$^{\mathrm{rd}}$ rows) and vector (2$^{\mathrm{nd}}$ and 4$^{\mathrm{th}}$ rows) LQs with $M_{LQ} = 600\,\mathrm{GeV}$ and coupling to second- (1$^{\mathrm{st}}$ and 2$^{\mathrm{nd}}$ rows) or third-generation (3$^{\mathrm{rd}}$ and 4$^{\mathrm{th}}$ rows) quarks were taken as signal.

		Events
MC	Di-μ	0.77±0.15
	Di-τ	0.09±0.05
	Total expected	0.86±0.15
DATA		0

Table 5.2: Number of events expected from SM process simulations after the final selection.

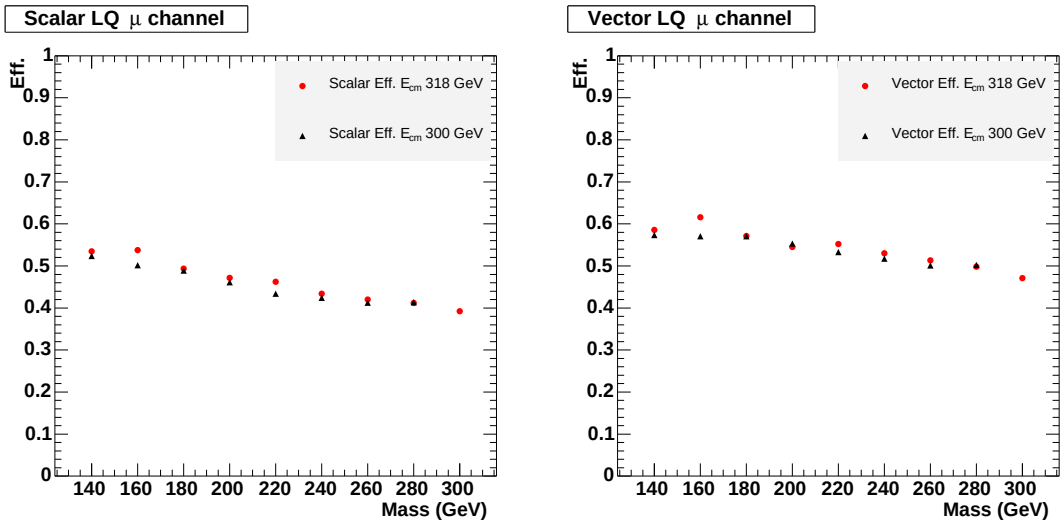

(a) (b)

Figure 5.5: Selection efficiencies for low-mass (a) scalar and (b) vector leptoquarks as a function of the mass. The efficiency for LQs produced in collisions with $\sqrt{s} = 300\,\text{GeV}$ is denoted with the triangles ▲, whereas the dots ● are used for $\sqrt{s} = 318\,\text{GeV}$.

A check was done using different LFV MC signal. Various high-mass scalar and vector LQ types, initial- and final-state quark generations were considered, as shown in Fig. 5.4, obtaining similar results.

After applying the optimized cuts, no event was found in data, while 0.86 ± 0.15 were expected from the simulation of the SM background. hi

5.4 Signal selection efficiencies

For LFV events mediated by resonant production of a leptoquark, the selection efficiency varies with the LQ mass. Since scalar and vector LQs give a different polar angle distribution for the final-state muon, they have a slightly different efficiency. The cross-section for low-mass LQs produced by the fusion of the electron and a sea quark is strongly suppressed because of the low sea quark density at high x (Fig. 1.4). Therefore, only LQs produced by electron-valence-quark fusion were considered: $F = 0$ LQs for the positron beam and $|F| = 2$ for the electron beam. Since in the analysis there are no requirements on the final-state-muon charge, the selection efficiency for LQs produced in e^+p and e^-p collisions is the same. The track of the candidate muons have a too high p_t^{trk} to permit the determination of the charge which, in any case, is not relevant for the selection. As shown in Fig. 5.5 the selection efficiency is very similar for LQs produced with 300 and 318 GeV of center-of-mass energy and it ranges from 39% to 54% for scalar LQs (Fig. 5.5(a)) and from 47% to 62% for vector LQs (Fig. 5.5(b)) with masses between 140 and 300 GeV.

For leptoquarks with mass much greater than the center-of-mass energy the efficiencies are almost independent of the LQ mass but depend on the generation of the initial- or final-state quark. Sea quarks, with softer Bjorken-x distribution than valence quarks, result in a lower momentum of the final-state lepton, leading to a lower signal efficiency. Overall, the selection efficiency for high-mass LQs is in the range $20-45\%$. In Tables 5.3 and 5.4 the selection efficiencies for high-mass LQs with $F = 0$ and $|F| = 2$, respectively, are shown. The energy available in the center of mass at HERA does not permit to be sensitive to the t quark. Therefore the cases, in which a t quark is involved, marked with $*$ in Tables 5.3 and 5.4, were not considered.

$\alpha\beta$	$S^L_{1/2}$	$S^R_{1/2}$	$\tilde{S}^L_{1/2}$	V^L_0	V^R_0	$\tilde{V}^R_0$	V^L_1
			e^+p $\sqrt{s} = 300\,\text{GeV}$				
1 1	0.44	0.44	0.40	0.36	0.36	0.41	0.39
1 2	0.45	0.45	0.35	0.39	0.39	0.43	0.43
1 3	*	0.36	0.36	0.39	0.39	*	0.39
2 1	0.28	0.30	0.38	0.30	0.30	0.38	0.27
2 2	0.21	0.29	0.30	0.32	0.32	0.26	0.25
2 3	*	0.26	0.29	0.26	0.26	*	0.26
3 1	*	0.26	0.26	0.25	0.25	*	0.25
3 2	*	0.25	0.25	0.26	0.26	*	0.26
3 3	*	0.20	0.20	0.21	0.21	*	0.21
			e^-p $\sqrt{s} = 318\,\text{GeV}$				
1 1	0.43	0.42	0.40	0.41	0.41	0.45	0.45
1 2	0.29	0.33	0.35	0.33	0.33	0.29	0.31
1 3	*	0.34	0.34	0.31	0.31	*	0.31
2 1	0.41	0.41	0.38	0.42	0.42	0.42	0.42
2 2	0.24	0.31	0.32	0.31	0.31	0.25	0.27
2 3	*	0.30	0.30	0.30	0.30	*	0.30
3 1	*	0.36	0.36	0.37	0.37	*	0.37
3 2	*	0.27	0.27	0.30	0.30	*	0.30
3 3	*	0.25	0.25	0.25	0.25	*	0.25
			e^+p $\sqrt{s} = 318\,\text{GeV}$				
1 1	0.47	0.46	0.42	0.42	0.42	0.45	0.44
1 2	0.42	0.43	0.43	0.40	0.40	0.44	0.43
1 3	*	0.42	0.36	0.37	0.37	*	0.37
2 1	0.28	0.31	0.34	0.36	0.36	0.30	0.32
2 2	0.24	0.28	0.31	0.32	0.32	0.24	0.27
2 3	*	0.31	0.31	0.30	0.30	*	0.30
3 1	*	0.30	0.30	0.33	0.33	*	0.33
3 2	*	0.27	0.27	0.30	0.30	*	0.30
3 3	*	0.24	0.24	0.26	0.26	*	0.26

Table 5.3: Selection efficiencies for high-mass $F = 0$ LQs inducing lepton-flavor-violating interactions (μ channel) for different lepton beams and center of mass energies. The first column indicates the quark generations coupling to LQ$-e$ and to LQ$-\mu$, respectively.

$\alpha\beta$	S_0^L	S_0^R	$\tilde{S}_0^R$	S_1^L	$V_{1/2}^L$	$V_{1/2}^R$	$\tilde{V}_{1/2}^L$
			e^+p $\sqrt{s} = 300\,\text{GeV}$				
1 1	0.41	0.41	0.37	0.38	0.36	0.38	0.39
1 2	0.26	0.26	0.31	0.30	0.33	0.30	0.28
1 3	*	*	0.24	0.30	0.26	0.26	*
2 1	0.41	0.41	0.37	0.38	0.44	0.43	0.44
2 2	0.21	0.21	0.30	0.27	0.32	0.29	0.26
2 3	*	*	0.22	0.22	0.26	0.26	*
3 1	*	*	0.33	0.33	0.34	0.34	*
3 2	*	*	0.22	0.22	0.26	0.26	*
3 3	*	*	0.17	0.17	0.21	0.21	*
			e^-p $\sqrt{s} = 318\,\text{GeV}$				
1 1	0.47	0.47	0.42	0.44	0.42	0.43	0.45
1 2	0.42	0.42	0.43	0.41	0.40	0.43	0.44
1 3	*	*	0.36	0.36	0.37	0.37	*
2 1	0.28	0.28	0.34	0.33	0.36	0.32	0.30
2 2	0.24	0.24	0.31	0.30	0.32	0.30	0.24
2 3	*	*	0.31	0.31	0.30	0.30	*
3 1	*	*	0.30	0.30	0.33	0.33	*
3 2	*	*	0.27	0.27	0.30	0.30	*
3 3	*	*	0.24	0.24	0.26	0.26	*
			e^+p $\sqrt{s} = 318\,\text{GeV}$				
1 1	0.43	0.43	0.40	0.40	0.41	0.44	0.45
1 2	0.29	0.29	0.35	0.34	0.33	0.31	0.29
1 3	*	*	0.34	0.34	0.31	0.31	*
2 1	0.41	0.41	0.38	0.40	0.42	0.42	0.42
2 2	0.24	0.24	0.32	0.31	0.31	0.29	0.25
2 3	*	*	0.30	0.30	0.30	0.30	*
3 1	*	*	0.36	0.36	0.37	0.37	*
3 2	*	*	0.27	0.27	0.30	0.30	*
3 3	*	*	0.25	0.25	0.25	0.25	*

Table 5.4: Selection efficiencies for high-mass $|F| = 2$ LQs inducing lepton-flavor-violating interactions (μ channel) for different lepton beams and center of mass energies. The first column indicates the quark generations coupling to LQ$-e$ and to LQ$-\mu$, respectively.

Chapter 6

Search for $e \to \tau$ transitions

This chapter describes the analysis on the search for lepton-flavor-violating interactions where the final-state lepton is a τ. As in the $e - \mu$ transition case, the signal was taken to be LFV processes mediated by LQs of any mass. All the τ decay channels were treated separately after a common preselection.

6.1 Common preselection

The characteristics of this type of events have already been described in Sec. 3.3. Due to the presence of at least one neutrino in all the τ-decay channels, a high value of $\not{P}_t$ is expected. Therefore, for all the channels, the CC DIS trigger (as described in Sec. 5.1 for the $e-\mu$ case) was used together with the following common preselection:

- a reconstructed vertex with $|Z_{\text{vtx}}| < 50\,\text{cm}$;
- $\not{P}_t > 15\,\text{GeV}$, in order to reject photoproduction and neutral current events.

In addition, the cuts described in Sec. 5.1 were applied in order to reject background from non-ep events.

6.2 Leptonic τ decay channels

For τ leptons decaying into muons ($\tau \to \mu\nu_\mu\nu_\tau$) the same selection cuts as described in Secs. 5.2 and 5.3 were applied, since the event topology is very similar to that of LFV with $e \to \mu$ transitions.

For the $\tau \to e\nu_e\nu_\tau$ channel the final state is characterized by a high-energy isolated electron in the $\not{P}_t$ vector direction. The following cuts were applied after the preselection:

		Events
MC	CC DIS $Q^2 > 100\,\mathrm{GeV}^2$	0.38±0.07
	Di-μ	0.016±0.016
	Di-τ	0.03±0.03
	Total expected	0.43±0.08
DATA		0

Table 6.1: Number of events expected from SM process simulations and found in data after the $\tau \to e\nu_e\nu_\tau$ decay channel final selection.

- $20 < E - P_Z < 52\,\mathrm{GeV}$;
- total energy deposit in RCAL less than 7 GeV;
- $\not{P}_t/\sqrt{E_t} > 2.5\sqrt{\mathrm{GeV}}$;
- an electron with energy larger than 20 GeV and probability $P_e > 0.001$ in the polar-angle region $8^\circ < \theta < 125^\circ$ and in the $\not{P}_t$ direction ($\Delta\phi < 20^\circ$);
- a jet with a transverse momentum above 25 GeV, back-to-back with respect to the electron ($\Delta\phi^{e-\mathrm{jet}} > 160^\circ$ where $\Delta\phi^{e-\mathrm{jet}}$ is the difference between the azimuthal angles of the jet and of the electron).

No event was found in data, while 0.43 ± 0.08 were expected from SM MC. Table 6.1 shows the contributions to the background from the different SM processes.

6.3 Hadronic τ decay channel

In the hadronic τ decay channel the τ finder described in Sec. 4.6 was employed.

6.3.1 Preselection

In addition to the common preselection cuts, the following cuts were applied in the preselection for the hadronic τ decay channel:

- no electron candidate with energy larger than 10 GeV and probability $P_e > 0.01$, in order to reject NC DIS events;
- $E_t > 45\,\mathrm{GeV}$;
- $15 < E - P_Z < 60\,\mathrm{GeV}$;

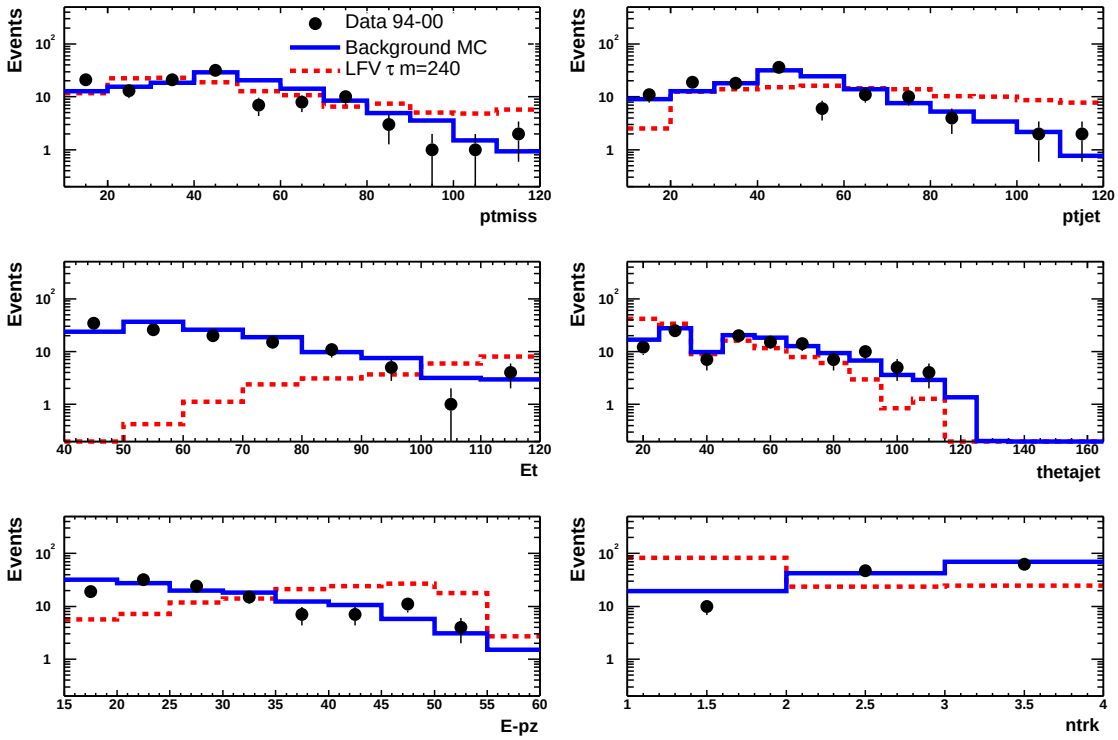

Figure 6.1: Comparison between data (dots) and SM MC (solid line) for some of the variables used in the preselection: $\not{P}_t$; the transverse momentum of the τ-jet candidate; the total transverse energy E_t; the polar angle of the τ-jet candidate; $E-P_Z$ and the number of tracks associated with the τ-jet candidate. The dashed line represents the LFV signal with an arbitrary normalization.

- total energy deposit in RCAL less than 7 GeV;
- a τ-jet candidate as described below.

The τ-jet candidate was chosen to be the jet with the higher value of the discriminant $\mathcal{D}$ (see Sec. 4.6) and it was required to have a transverse momentum greater than 15 GeV, to be within the CTD acceptance ($15^\circ < \theta < 164^\circ$) and to have between one and three tracks pointing to the CAL energy deposit associated with the jet. Events with τ-jet candidates in the region between FCAL and BCAL ($36^\circ < \theta < 42^\circ$) were removed. In order to reject electrons from NC events, a cut of 0.95 was applied to the electromagnetic energy fraction of the jet ($f_{\rm EMC}$). In addition the jet was required to satisfy the condition $f_{\rm LT} + f_{\rm EMC} < 1.6$, where $f_{\rm LT}$ (the leading track fraction) is defined as the ratio between the momentum of the

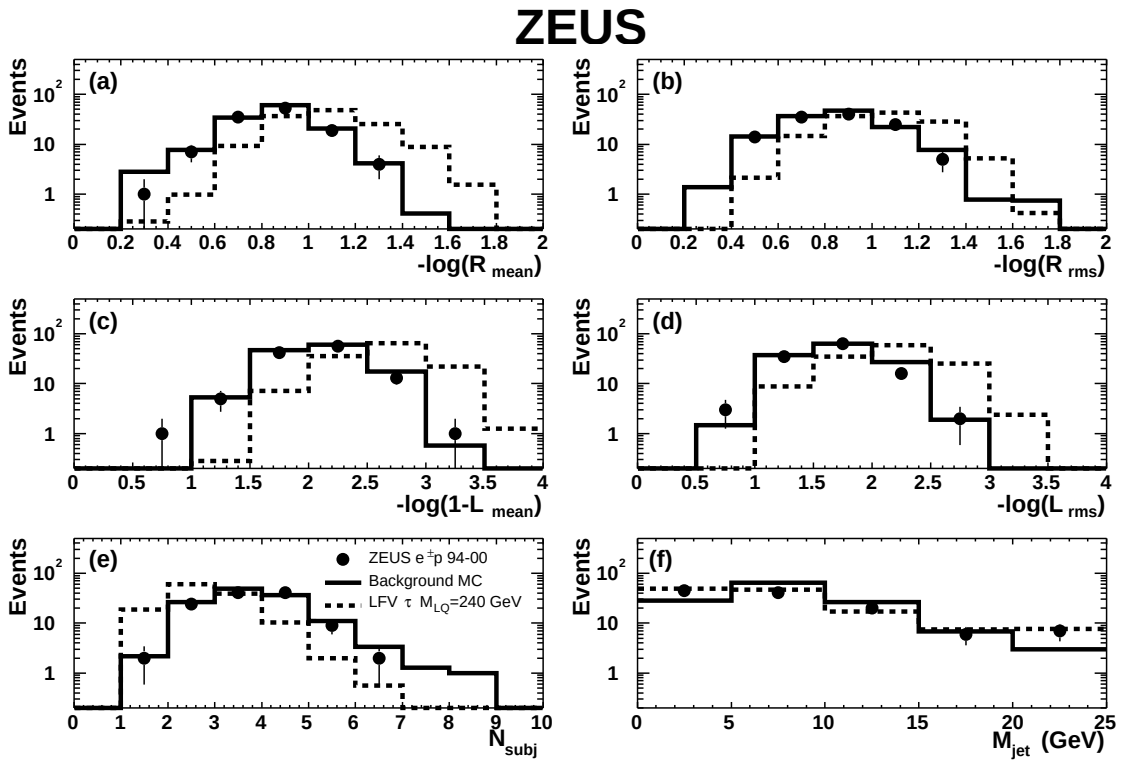

Figure 6.2: Comparison between data (dots) and SM MC (solid line) for the variables used in the τ discriminant: (a) $-\log(R_{\rm mean})$; (b) $-\log(R_{\rm rms})$; (c) $-\log(1-L_{\rm mean})$; (d) $-\log(L_{\rm rms})$; (e) number of sub-jets, $N_{\rm subj}$; (f) jet mass, $M_{\rm jet}$, after the τ-channel preselection (hadronic τ decays). The dashed line represents the LFV signal with an arbitrary normalization.

most energetic track in the jet and the jet energy. The quantity $f_{\rm LT} + f_{\rm EMC}$ is close to 2 for electrons, the main source of background that this cut is designed to reject.

Figure 6.1 shows the distribution of several variables used in the selection after the preselection cuts. Data are compared to the Standard Model expectation (which is a sum of the different SM Monte Carlo contributing to the background) normalized to the luminosity of data and to a simulated LFV signal with an arbitrary normalization. Figure 6.2 shows the comparison, after the preselection, between data and MC for the jet discriminant variables. Figure 6.3 compares the discriminant and the $\Delta\phi$ distributions. Here $\Delta\phi$ is the azimuthal angle between the candidate τ-jet axis and the $\not{P}_t$ vector. After the hadronic preselection, 119 events were found in data, while 131 ± 4 were expected from SM processes, mainly from CC DIS. In Table 6.2 the number of expected events, subdivided into the different background processes, is shown.

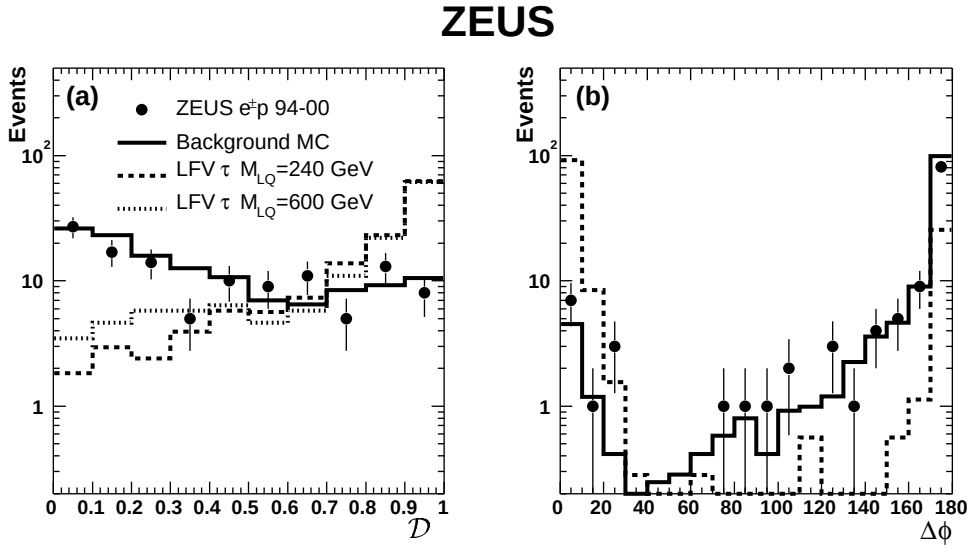

Figure 6.3: Distribution of (a) the discriminant, $\mathcal{D}$ and (b) $\Delta\phi$, after hadronic τ decay preselection. The dots represent the data while the solid line is the SM prediction from MC. The LFV signal distribution for two different LQ masses, 240 GeV (dashed line) and 600 GeV (dash-dotted line), are also shown with an arbitrary normalization. The distribution of $\Delta\phi$ for the $M_{LQ} = 600\,\text{GeV}$ LQ, which is similar to the $M_{LQ} = 240\,\text{GeV}$ LQ $\Delta\phi$ distribution, is omitted.

		Presel.	**Presel. and $\mathcal{D}$ cut**	**Final Selection**
MC	CC DIS $Q^2 > 100\,\text{GeV}^2$	116±3	7.0±0.3	0.017±0.017
	NC DIS $Q^2 > 400\,\text{GeV}^2$	1.9±1.1	1.6±0.5	0.4±0.2
	Di-μ	0.13±0.06	0.03±0.03	0
	Di-τ	0.33±0.09	0.19±0.07	0.08±0.05
	Photoproduction	11.8±1.9	1.4±0.6	0.6±0.4
	Total expected	131±4	10.2±0.9	1.1±0.5
DATA		119	8	0

Table 6.2: Number of events expected from SM process simulations after (first column) the hadronic τ decay channel preselection, (second column) the hadronic τ decay channel preselection and the cut on $\mathcal{D}$, (third column) the hadronic τ decay channel final selection.

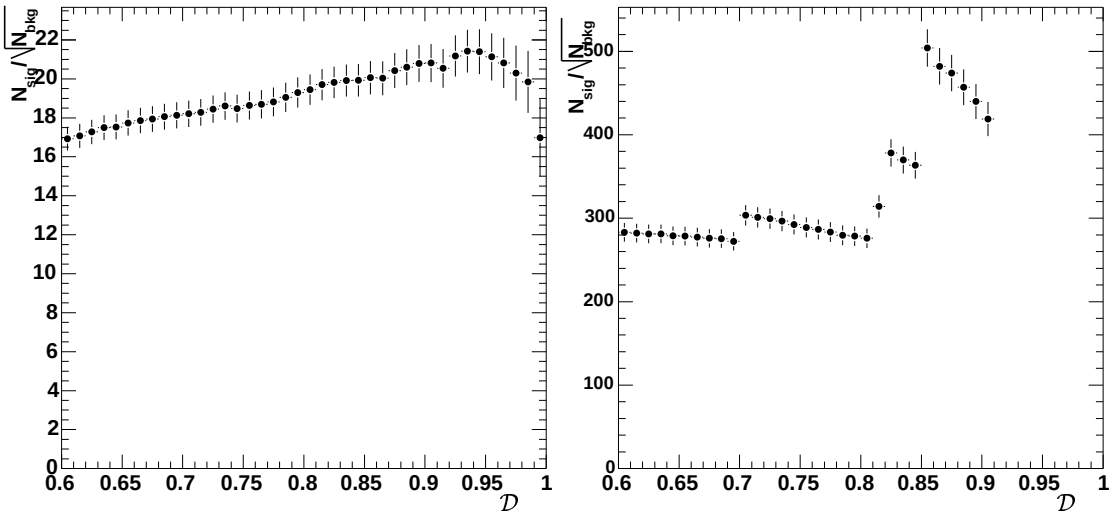

(a) (b)

Figure 6.4: Ratio between the number of selected signal events N_{sig} and the number of background events N_{bkg} after (a) the preselection cuts and (b) the preselection cuts and the cut on $\Delta\phi$. The CC DIS sample, which constituted most of the background after the preselection, has been chosen as representative background. The step distribution of (b) is due to the low statistics in the background sample.

The data distributions in Figs. 6.1, 6.2 and 6.3 generally conform to those expected from SM backgrounds.

6.3.2 Final selection

The final selection cuts are designed to selects jets coming from τ and to reduce the CC DIS background, which dominates after the preselection, to a very low level. Therefore, the following additional cuts were applied to the events in Fig. 6.3:

- $\mathcal{D} > 0.9$;
- the τ-jet candidate was required to be aligned in azimuth with the direction of the $\not{P}_t$ ($\Delta\phi < 20°$).

The discriminant cut was tuned to optimize the separation power, $S = \epsilon_{\text{sig}} \cdot \sqrt{R}$ (where ϵ_{sig} is the signal efficiency and $R = 1/\epsilon_{\text{bg}}$ is the background rejection), for a scalar LQ with a mass of 240 GeV. Figure 6.4 shows the ratio between the number of selected signal events N_{sig} and the number of background events N_{bkg} after the

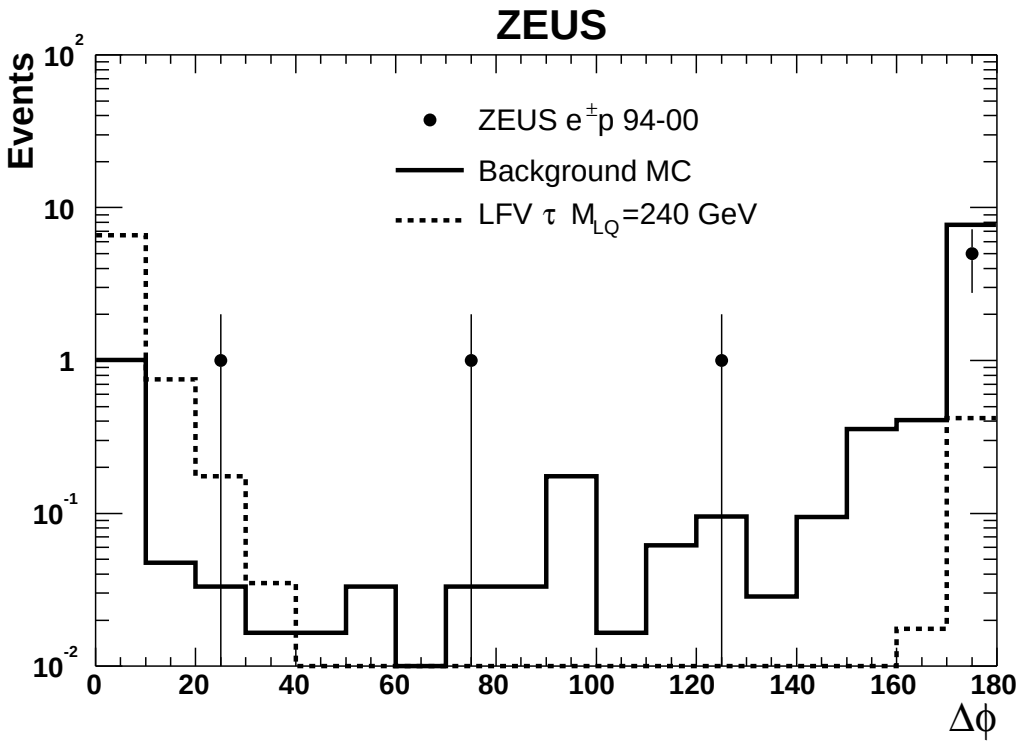

Figure 6.5: $\Delta\phi$ distribution of the events with $\mathcal{D} > 0.9$ after the hadronic τ decay preselection. The dots represent the data while the solid line is the SM prediction from MC. The dashed line represents the LFV signal with an arbitrary normalization.

preselection cuts (Fig. 6.4(a)), and after both the preselection cuts and the cut on $\Delta\phi$ (Fig. 6.4(b)).

In Fig. 6.5, the $\Delta\phi$ distribution of the 8 events with $\mathcal{D} > 0.9$ is shown compared to the SM expectation of 10.2 ± 0.9 events. Details on the number of events expected for the different processes are shown in Table 6.2 (second column). In order to have enough Monte Carlo statistics after the cuts and to compare in a better way the simulation with the data, the number of CC and NC MC events in Fig. 6.5 as well as in the second and third column of Table 6.2 was increased by almost a factor 5 with respect to those listed in Table 3.2. The small fraction of the signal ($\sim 5\%$) with $\Delta\phi > 160^\circ$ is due to events where the τ-jet is outside the CTD acceptance. The two events from data that have $\Delta\phi = 72^\circ$ and $\Delta\phi = 126^\circ$ were also found in a previous ZEUS search for isolated τ lepton events [2] (see Sec. 1.2.3). The event with $\Delta\phi = 22^\circ$ is shown in Fig. 6.6.

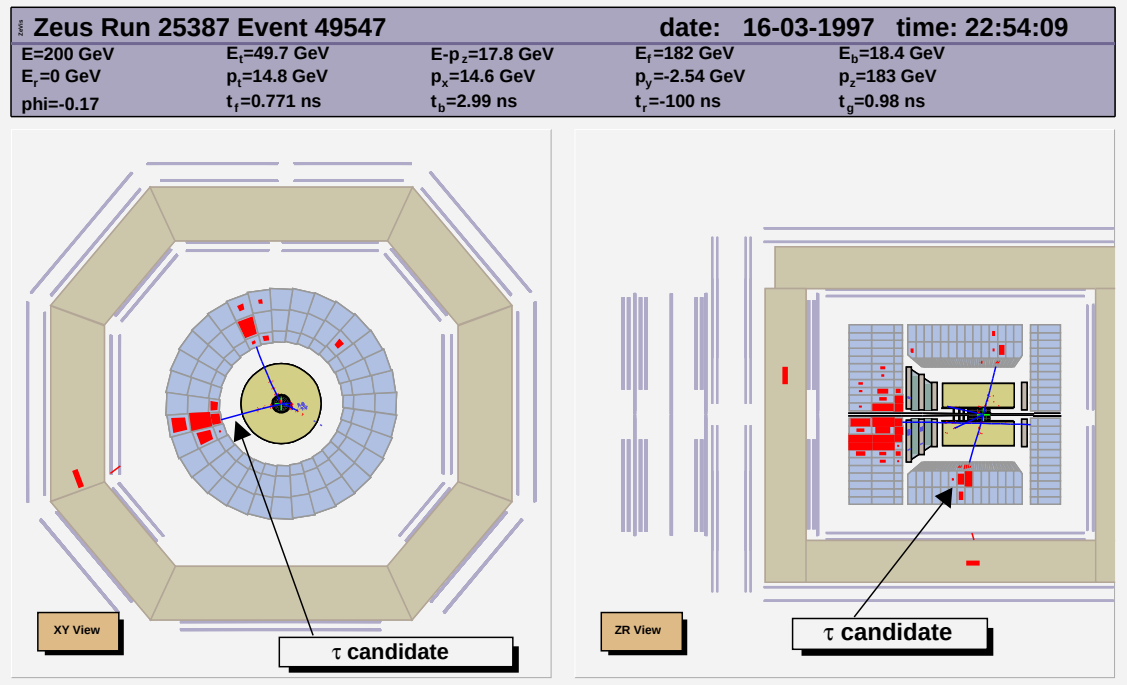

Figure 6.6: Event in 1994–1997 data which passes the preselection cuts and the cut on $\mathcal{D}$. In the figure the candidate jet from τ is indicated. This event is likely a τ pair production, since the second jet visible in the event could come from another τ.

After imposing of the final cut on $\Delta\phi$, no event remained in the hadronic decay channel, while 1.1 ± 0.5 were expected from MC as shown in Table 6.2.

6.4 Signal selection efficiencies

No candidate was found in data for any of the three τ-decay channels, while 2.3 ± 0.5 were predicted by Standard Model simulations. The contribution from the different Standard Model processes is shown in Table 6.3.

Figure 6.7 shows the selection efficiency for low-mass scalar (Fig. 6.7(a)) and vector (Fig. 6.7(b)) leptoquarks as a function of the mass for all the τ decay channels. The combined selection efficiency is also shown. The efficiencies refer to LQs produced at 318 GeV of center-of-mass energy. As in the $e - \mu$ transition case the selection efficiencies for leptoquarks produced at $\sqrt{s} = 300$ GeV are very similar to those reported in Fig. 6.7, as it can be seen in Fig. 6.8, where only the combined efficiencies are shown.

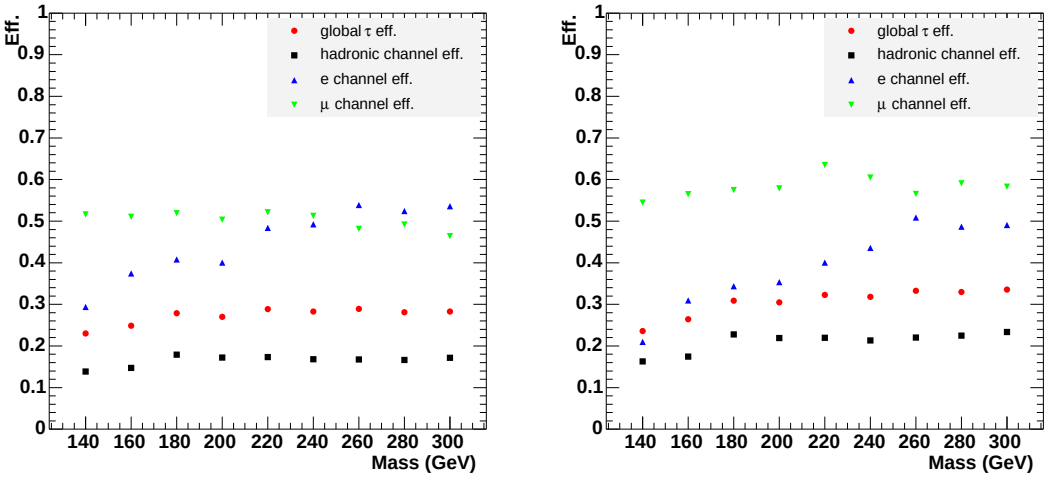

(a) (b)

Figure 6.7: Selection efficiencies for low-mass (a) scalar and (b) vector leptoquarks as a function of the mass for the different τ decay channels: the triangles ▲ represent $\tau \to e\nu_e\nu_\tau$ channel efficiencies; the triangles ▼ the $\tau \to \mu\nu_\mu\nu_\tau$ channel; the squares ■ the $\tau \to$ hadrons ν_τ channel; the dots ● the combined efficiency.

		Events
MC	CC DIS $Q^2 > 100\,\text{GeV}^2$	0.41±0.08
	NC DIS $Q^2 > 400\,\text{GeV}^2$	0.4±0.2
	Di-μ	0.79±0.15
	Di-τ	0.17±0.07
	Photoproduction	0.6±0.4
	Total expected	2.3±0.5
DATA		0

Table 6.3: Number of events expected from SM process simulations in all the τ decay channels after the final selection.

The combined selection efficiency for low-mass ($M_{\text{LQ}} < \sqrt{s}$) scalar (vector) LQs is in the range of $22 - 29\%$ ($23 - 34\%$).

Tables 6.4 and 6.5 show the overall efficiency for LFV $e - \tau$ transitions mediated by high-mass ($M_{\text{LQ}} \gg \sqrt{s}$) LQs. The efficiencies depend on the initial- and final-

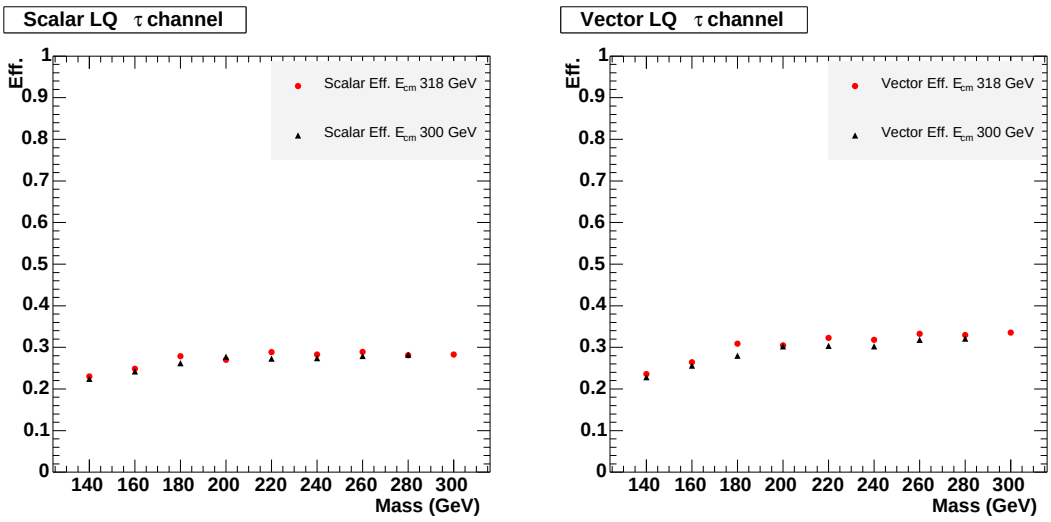

(a) (b)

Figure 6.8: Selection efficiencies for low-mass (a) scalar and (b) vector leptoquarks as a function of the mass. The efficiency for LQs produced in collisions with $\sqrt{s} = 300\,\text{GeV}$ is denoted with triangles ▲, whereas dots ● are used for $\sqrt{s} = 318\,\text{GeV}$.

state quark generations and they are in the range $4-20\%$.

$\alpha\beta$	$S^L_{1/2}$	$S^R_{1/2}$	$\tilde{S}^L_{1/2}$	V^L_0	V^R_0	$\tilde{V}^R_0$	V^L_1
			e^+p $\sqrt{s} = 300\,\text{GeV}$				
1 1	0.18	0.17	0.14	0.12	0.12	0.14	0.14
1 2	0.19	0.17	0.12	0.13	0.13	0.17	0.16
1 3	*	0.12	0.10	0.12	0.12	*	0.12
2 1	0.07	0.08	0.15	0.09	0.09	0.07	0.08
2 2	0.07	0.08	0.10	0.07	0.07	0.05	0.06
2 3	*	0.07	0.09	0.06	0.06	*	0.06
3 1	*	0.07	0.12	0.07	0.07	*	0.07
3 2	*	0.06	0.08	0.05	0.05	*	0.05
3 3	*	0.05	0.06	0.04	0.04	*	0.04
			e^-p $\sqrt{s} = 318\,\text{GeV}$				
1 1	0.17	0.16	0.14	0.16	0.16	0.19	0.19
1 2	0.09	0.11	0.12	0.11	0.11	0.08	0.09
1 3	*	0.10	0.10	0.10	0.10	*	0.10
2 1	0.18	0.17	0.15	0.15	0.15	0.17	0.18
2 2	0.07	0.10	0.10	0.10	0.10	0.07	0.08
2 3	*	0.09	0.09	0.10	0.10	*	0.10
3 1	*	0.12	0.12	0.14	0.14	*	0.14
3 2	*	0.08	0.08	0.09	0.09	*	0.09
3 3	*	0.06	0.06	0.07	0.07	*	0.07
			e^+p $\sqrt{s} = 318\,\text{GeV}$				
1 1	0.20	0.20	0.18	0.15	0.15	0.19	0.18
1 2	0.20	0.19	0.17	0.14	0.14	0.18	0.17
1 3	*	0.14	0.14	0.14	0.13	*	0.13
2 1	0.08	0.10	0.11	0.11	0.11	0.08	0.09
2 2	0.08	0.09	0.10	0.11	0.11	0.07	0.08
2 3	*	0.09	0.09	0.09	0.09	*	0.09
3 1	*	0.09	0.09	0.10	0.10	*	0.10
3 2	*	0.08	0.08	0.09	0.09	*	0.09
3 3	*	0.07	0.07	0.06	0.06	*	0.06

Table 6.4: Selection efficiencies for high-mass $F = 0$ LQs inducing lepton-flavor-violating interactions ($e-\tau$) for different lepton beams and center-of-mass energies. The first column indicates the quark generations coupling to LQ$-e$ and to LQ$-\tau$, respectively.

$\alpha\beta$	S_0^L	S_0^R	$\tilde{S}_0^R$	S_1^L	$V_{1/2}^L$	$V_{1/2}^R$	$\tilde{V}_{1/2}^L$
			e^+p $\sqrt{s} = 300\,\text{GeV}$				
1 1	0.15	0.15	0.11	0.13	0.12	0.14	0.15
1 2	0.07	0.07	0.08	0.09	0.09	0.08	0.07
1 3	*	*	0.07	0.07	0.06	0.06	*
2 1	0.15	0.15	0.11	0.13	0.14	0.16	0.17
2 2	0.07	0.07	0.10	0.08	0.07	0.08	0.08
2 3	*	*	0.06	0.06	0.06	0.06	*
3 1	*	*	0.11	0.10	0.12	0.12	*
3 2	*	*	0.05	0.05	0.07	0.07	*
3 3	*	*	0.04	0.04	0.06	0.06	*
			e^-p $\sqrt{s} = 318\,\text{GeV}$				
1 1	0.20	0.20	0.18	0.19	0.15	0.16	0.19
1 2	0.20	0.20	0.17	0.19	0.14	0.18	0.18
1 3	*	*	0.14	0.14	0.13	0.13	*
2 1	0.08	0.08	0.11	0.11	0.11	0.11	0.08
2 2	0.08	0.08	0.10	0.10	0.11	0.09	0.07
2 3	*	*	0.09	0.09	0.09	0.09	*
3 1	*	*	0.09	0.09	0.10	0.10	*
3 2	*	*	0.08	0.08	0.09	0.09	*
3 3	*	*	0.07	0.07	0.06	0.06	*
			e^+p $\sqrt{s} = 318\,\text{GeV}$				
1 1	0.17	0.17	0.14	0.15	0.16	0.18	0.19
1 2	0.09	0.09	0.12	0.12	0.11	0.10	0.08
1 3	*	*	0.10	0.10	0.10	0.10	*
2 1	0.18	0.18	0.15	0.16	0.15	0.16	0.17
2 2	0.07	0.07	0.10	0.10	0.10	0.09	0.07
2 3	*	*	0.09	0.09	0.10	0.10	*
3 1	*	*	0.12	0.12	0.14	0.14	*
3 2	*	*	0.08	0.08	0.09	0.09	*
3 3	*	*	0.06	0.06	0.07	0.07	*

Table 6.5: Selection efficiencies for high-mass $|F| = 2$ LQs inducing lepton-flavor-violating interactions ($e-\tau$) for different lepton beams and center-of-mass energies. The first column indicates the quark generations coupling to LQ$-e$ and to LQ$-\tau$, respectively.

Chapter 7

Results

As shown in the previous chapters, no evidence of lepton-flavor violation was found in the data collected by ZEUS during the HERA I data taking. This chapter describes how this result has been translated into limits on the coupling constants for beyond-Standard-Model interactions . As already stated in Sec. 3.3, in order to set limits, a particular LFV process, based on a leptoquark model, was considered. However the results can be extended to other kinds of interactions, like for example squark production via R-parity-violating supersymmetry. In the last sections, the limits obtained in this analysis are compared to existing limits from other experiments.

7.1 Limit calculation

As discussed in the previous chapters, the 1994–2000 data, corresponding to an integrated luminosity of $130\,\mathrm{pb}^{-1}$ (see Table 2.1), were analyzed searching for $e-\mu$ or $e-\tau$ transitions. Since no evidence of lepton-flavor-violating interactions was found, limits were set using a Bayesian approach [75] that assumes a flat "prior" probability for the signal cross section on the processes $ep \to \mu X$ and $ep \to \tau X$ mediated by a leptoquark.

7.1.1 Calculation using a Bayesian approach

Given a set of experimental measurements $\vec{m}$, which has a probability distribution that depends on an unknown parameter p, in the Bayesian statistical approach the *a posteriori* probability density function $f(p|\vec{m})$ gives the degree of belief of p to assume a certain value given the dataset $\vec{m}$. According to the Bayes theorem,

$f(p|\vec{m})$ is given by:

$$f(p|\vec{m}) = \frac{L(\vec{m}|p)f'(p)}{\int L(\vec{m}|p')f'(p')dp'}. \tag{7.1}$$

The quantity $L(\vec{m}|p)$ is a likelihood function, which gives the probability to measure $\vec{m}$ given a certain value of the parameter p. The function $f'(p)$ is the "prior" probability for p and it incorporates the knowledge of p before the experiment. The denominator is a normalization factor which assures that $\int f(p|\vec{m})dp = 1$.

In a counting experiment the likelihood function is given by a Poisson distribution:

$$L(N_{\text{obs}}|p) = \frac{(p + N_{\text{bkg}})^{N_{\text{obs}}}}{N_{\text{obs}}!}e^{(p+N_{\text{bkg}})}, \tag{7.2}$$

where N_{obs} is the number of observed events, p represents the beyond-Standard-Model signal and N_{bkg} is the number of background events expected from SM interactions. If the number of observed events is zero or compatible with the background, the limit on the number of signal events N_{lim} with a given credible interval (or confidence level C.L.) can be obtained requiring:

$$\text{C.L.} = \int_0^{N_{\text{lim}}} f(p|\vec{m})dp. \tag{7.3}$$

It can be shown that, for counting experiments, assuming a flat prior probability, this quantity reduces to Eq. (5.1). If no event is found, as in this analysis, Eq. (5.1) can be written in a simpler form that allows for an analytical inversion:

$$1 - \text{C.L.} = e^{-N_{\text{lim}}}, \tag{7.4}$$

which gives $N_{\text{lim}} \simeq 3$ at 95% C.L. The limit on the cross section for a beyond-SM process can be obtained using the formula $N_{\text{lim}} = \sigma_{\text{lim}}\varepsilon L$, where ε is the selection efficiency and L is the integrated luminosity.

The cross-section approximations used for the LQs mediating LFV interactions have been explained in Sec. 1.3.3. As can be seen from Eq. (1.21), in the low-mass case the cross section is proportional to the factor $\lambda_{eq_1}\sqrt{\beta_{\ell q}}$, where λ_{eq_1} is the coupling between the leptoquark, the electron and a first-generation quark, and $\beta_{\ell q}$ is the branching ratio of the leptoquark into a lepton ℓ ($\ell = \mu$, τ) and a quark q (u, d, s, c, b). Therefore limits on the cross section were converted into limits on $\lambda_{eq_1}\sqrt{\beta_{\ell q}}$.

For high-mass leptoquarks, the cross section is proportional to $\lambda_{eq_\alpha}\lambda_{\ell q_\beta}/M^2_{\text{LQ}}$, where α and β are quark generation indices (see Eq. (1.22)). In this case the limits were converted into limits on $\lambda_{eq_\alpha}\lambda_{\ell q_\beta}/M^2_{\text{LQ}}$.

In the low-mass case limits for 1994–1997 e^+p data at $\sqrt{s} = 300\,\text{GeV}$ and for 1999–2000 e^+p data at $\sqrt{s} = 318\,\text{GeV}$ were combined. Defining $L_{94-97}(N_{\text{obs}}, 94|\lambda)$

($L_{99-00}(N_{\rm obs}, 99|\lambda)$), with $\lambda = \lambda_{eq_1}\sqrt{\beta_{\ell q}}$, as the likelihood function relative to the 1994–1997 (1999–2000) data, the combined likelihood function is given by:

$$L(N_{\rm obs,94}; N_{\rm obs,99}|\lambda) = L_{94-97}(N_{\rm obs,94}|\lambda) \cdot L_{99-00}(N_{\rm obs,99}|\lambda). \tag{7.5}$$

In the Bayesian approach Eq. (7.5) can be interpreted using the information gathered from the first experiment, i.e. $L_{94-97}(N_{\rm obs,94}|\lambda)$, as prior knowledge for the second experiment (1999–2000).

Since no event was found in each data set the limits on $F = 0$ leptoquarks at low-mass can be calculated analytically and it can be shown that:

$$\frac{1}{\lambda_{F=0}} = \frac{1}{\lambda_{94-97}} + \frac{1}{\lambda_{99-00}}, \tag{7.6}$$

where

$$\lambda_{94-97} = \frac{3}{L_{94-97}\ \varepsilon_{94-97}\ \sigma(\sqrt{s} = 300\,\text{GeV})}, \tag{7.7}$$

and

$$\lambda_{99-00} = \frac{3}{L_{99-00}\ \varepsilon_{99-00}\ \sigma(\sqrt{s} = 318\,\text{GeV})}. \tag{7.8}$$

The data corresponding to e^-p interactions (1998–1999) were used to set limits on $|F| = 2$ low-mass LQs as described by the formula:

$$\lambda_{|F|=2} = \frac{3}{L_{98-99}\ \varepsilon_{98-99}\ \sigma(\sqrt{s} = 318\,\text{GeV})}. \tag{7.9}$$

In a similar way, limits for high-mass leptoquarks were combined using the whole statistics (1994–2000). The combined limit $\lambda_{\rm Combined}$ on $\lambda_{eq_\alpha}\lambda_{\ell q_\beta}/M^2_{\rm LQ}$ was obtained using the formula:

$$\frac{1}{\lambda_{\rm Combined}} = \frac{1}{\lambda_{94-97}} + \frac{1}{\lambda_{98-99}} + \frac{1}{\lambda_{99-00}}. \tag{7.10}$$

7.1.2 Corrections to the leading-order cross section

The cross sections used in the limit calculation procedure, reported in Eq. (1.21) and Eq. (1.22), were evaluated using the CTEQ5 [62] parton densities, taking into account the QED initial-state radiation, and, for low-mass scalar leptoquarks, NLO QCD corrections.

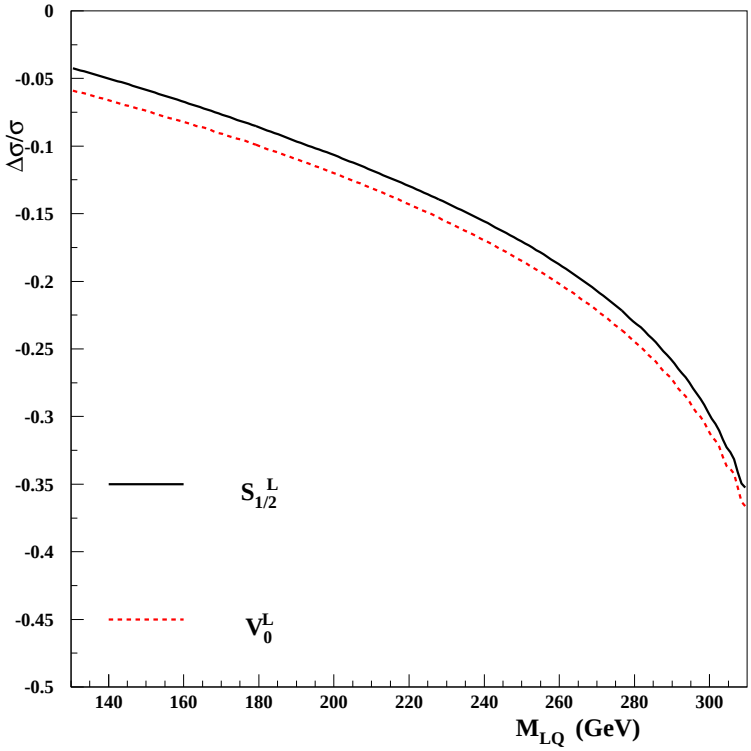

Figure 7.1: Relative correction to the cross section due to the inclusion of the ISR. The solid line represents the correction for a LQ coupling to eu, while the dashed line is the correction for a LQ coupling to ed.

Initial-state radiation

The initial-state electron can radiate a photon losing part of its energy. Therefore, the effect of the QED initial-state radiation (ISR) is to decrease the energy available in the center of mass. The ISR was calculated using the Weiszäcker-Williams formula [76], which gives the energy spectrum of the photons radiated collinearly by the initial-state electron. The flux $g(z)$ of the photons with a fraction z of the incident electron energy is given by:

$$g(z) = \frac{\alpha}{2\pi} \frac{1+(1-z)^2}{z} \log\left(\frac{Q^2}{4m_e}\right), \tag{7.11}$$

where α is the electromagnetic coupling constant, m_e is the mass of the electron and Q^2 was set to M^2_{LQ} in the calculation. The corrected cross section is obtained

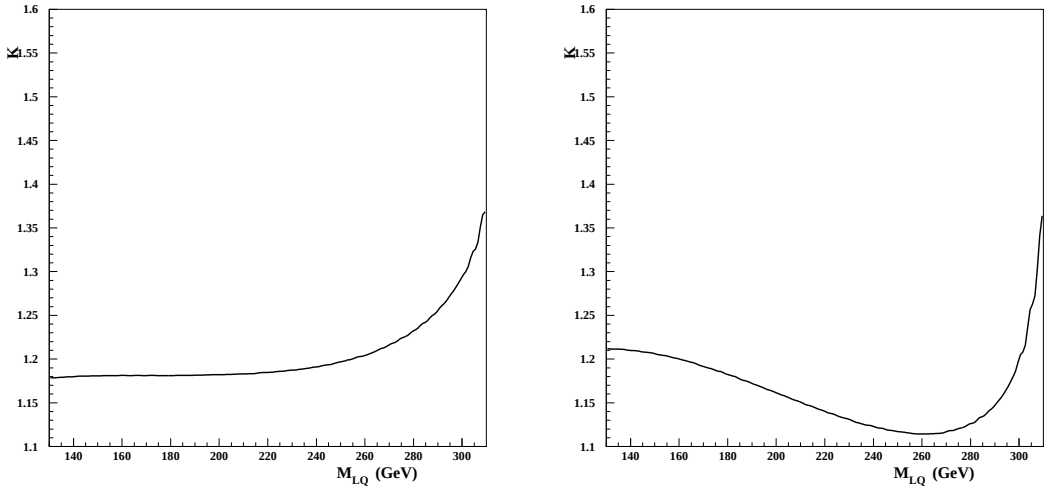

(a) (b)

Figure 7.2: Next-to-leading-order correction factor, K as a function of the LQ mass for a scalar leptoquark coupling to (a) eu and (b) ed.

by the convolution of the LO cross section and the $g(z)$ function. A consequence of the decrease of the center-of-mass energy of the electron-proton system is the increase, for a given LQ mass, of the fraction of the proton momentum carried by the quark, x, needed to produce the LQ. Since the quark density decreases at very high x, the corrected cross section is lower with respect to the LO cross section, especially for low-mass LQs. The correction is shown in Fig. 7.1 for two different $F = 0$ low-mass LQs $S^L_{1/2}$ and V^L_0, coupling to eu and ed respectively (the other cases are linear combinations of these two cases, as can be seen in Table 1.3), and it reaches $\sim 30\%$ at $M_{\mathrm{LQ}} = 300\,\mathrm{GeV}$ with $\sqrt{s} = 318\,\mathrm{GeV}$. The correction is $\sim 5\%$ for high-mass leptoquarks.

Next-to-leading-order corrections

The calculation of the next-to-leading-order corrections has been done only for low-mass scalar LQs [77]. The K factor defined by the ratio between the NLO and the LO cross section has been calculated. Figure 7.2 shows the values of K for a scalar LQ coupling to eu (Fig. 7.2(a)) and to ed (Fig. 7.2(b)) as a function of leptoquark mass. The QCD vertex corrections lead to a running of the coupling constant $\lambda_{\ell q_\alpha}$. This correction, which depends on the LQ mass, has been included

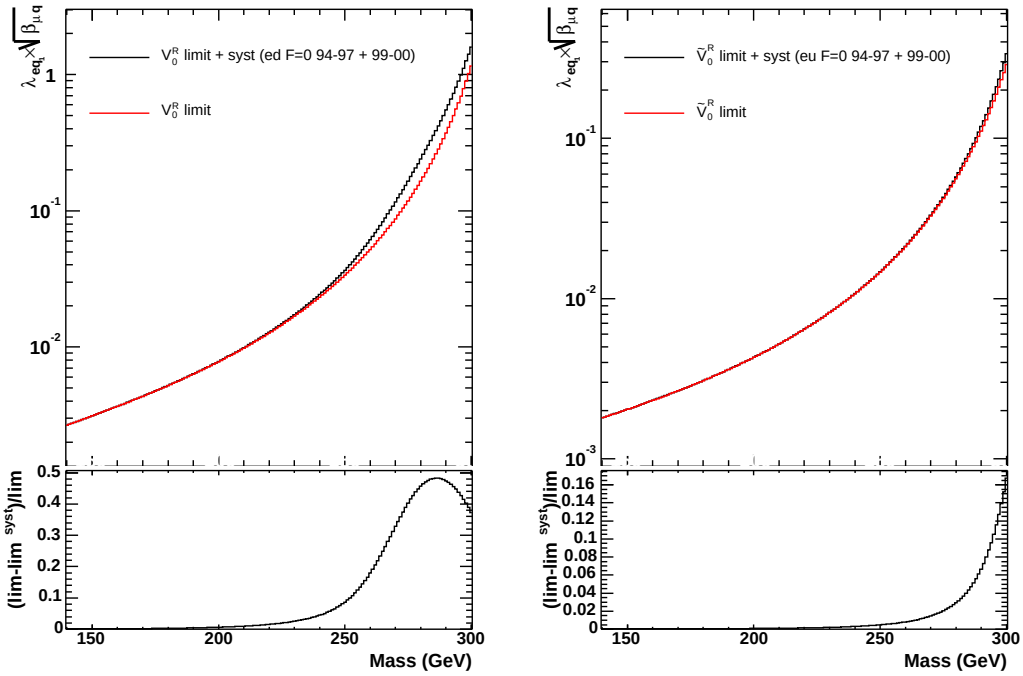

Figure 7.3: Effect of systematic corrections on the limits for the V_0^R LQ coupling to ed (left) and for the $\widetilde{V}_0^R$ LQ coupling to eu (right). The uncorrected limit is shown as a black dashed line in the upper plots. The red continuous line represents the limit obtained including systematic uncertainties. The lower plots show the relative differences.

in the calculation of the cross section and its effect is to increase the cross section by about 30%.

7.1.3 Systematic uncertainties

The following sources of systematic uncertainties have been considered:

- the calorimeter energy-scale uncertainty (2%); the resulting variation in the signal efficiency for the μ (τ) channel is less than 1% (3%) for low-mass leptoquarks and less than 5% for high-mass leptoquarks;
- the luminosity uncertainty: 1.5% for 1994–1997 e^+p data, 1.8% for 1998–1999 e^-p data and 2.2% for 1999–2000 e^+p data;
- uncertainties on the parton-density functions have been calculated using the

LQ type	$\tilde{S}^L_{1/2}$	$S^L_{1/2}$	$S^R_{1/2}$	V^L_0	V^R_0	$\tilde{V}^R_0$	V^L_1
$e-\mu$ limit on M_{LQ}(GeV)	273	293	293	274	278	296	299
$e-\tau$ limit on M_{LQ}(GeV)	270	291	291	271	276	294	298

Table 7.1: 95% C.L. lower limits on M_{LQ} for $F = 0$ LQs mediating $e-\mu$ and $e-\tau$ transitions assuming $\lambda_{eq_1} = \lambda_{\ell q_\beta} = 0.3$.

40 alternative sets of parton density parametrizations provided by CTEQ6.1 [11, 78]; this contributes to the dominant uncertainty for low-mass leptoquarks, especially when a d quark is involved and the LQ mass approaches the HERA kinematic limit.

These systematic uncertainties have been included in the limit calculation assuming a Gaussian distribution for their probability densities. All the uncertainty sources have been treated as independent and they can be summarized defining the quantity $\beta_0 = L\varepsilon\sigma_0$, where σ_0 is the LQ cross section assuming $\lambda = 1$. The Bayesian probability function with the inclusion of the systematic uncertainties then becomes:

$$f(\lambda|N_{\mathrm{obs}}=0) = \frac{\int L(N_{\mathrm{obs}}=0|\lambda,\beta) f'(\lambda) \exp\left(\frac{(\beta-\beta_0)^2}{2\sigma_\beta^2}\right) d\beta}{\iint L(N_{\mathrm{obs}}=0|\lambda',\beta) f'(\lambda') \exp\left(\frac{(\beta-\beta_0)^2}{2\sigma_\beta^2}\right) d\lambda' d\beta}, \tag{7.12}$$

where σ_β is the overall systematic uncertainty on β_0. For low-mass LQs, the effect of the inclusion of systematic uncertainties is the largest at the highest masses and the limit on the coupling increases by less than 7% at 250 GeV as can be seen in Fig. 7.3. The effect is very small for high-mass LQs (below 1%).

7.1.4 Low-mass leptoquark and squark limits

Upper limits on $\lambda_{eq_1}\sqrt{\beta_{\mu q}}$, obtained as described in the previous sections, are shown in Figs. 7.4 and 7.5 for $F = 0$ and $|F| = 2$ scalar and vector LQs, assuming resonantly produced leptoquarks in the BRW model. Since, for sufficiently large LQ masses, the cross section is dominated by electron valence-quark fusion, only e^+p (e^-p) data were used to determine $F = 0$ ($|F| = 2$) LQ production limits. Similar considerations hold for the results shown for the $e-\tau$ case in Figs. 7.6 and 7.7.

For couplings with electromagnetic strength ($\lambda_{eq_1} = \lambda_{\ell q_\beta} = 0.3 \approx \sqrt{4\pi\alpha}$), LQs with masses up to 299 GeV are excluded (see Tables 7.1 and 7.2). Alternatively, for a fixed M_{LQ} of 250 GeV, values of $\lambda_{eq_1}\sqrt{\beta_{\mu q}}$ and of $\lambda_{eq_1}\sqrt{\beta_{\tau q}}$ down to 0.010 and 0.013, respectively, are excluded (see Tables 7.3 and 7.4).

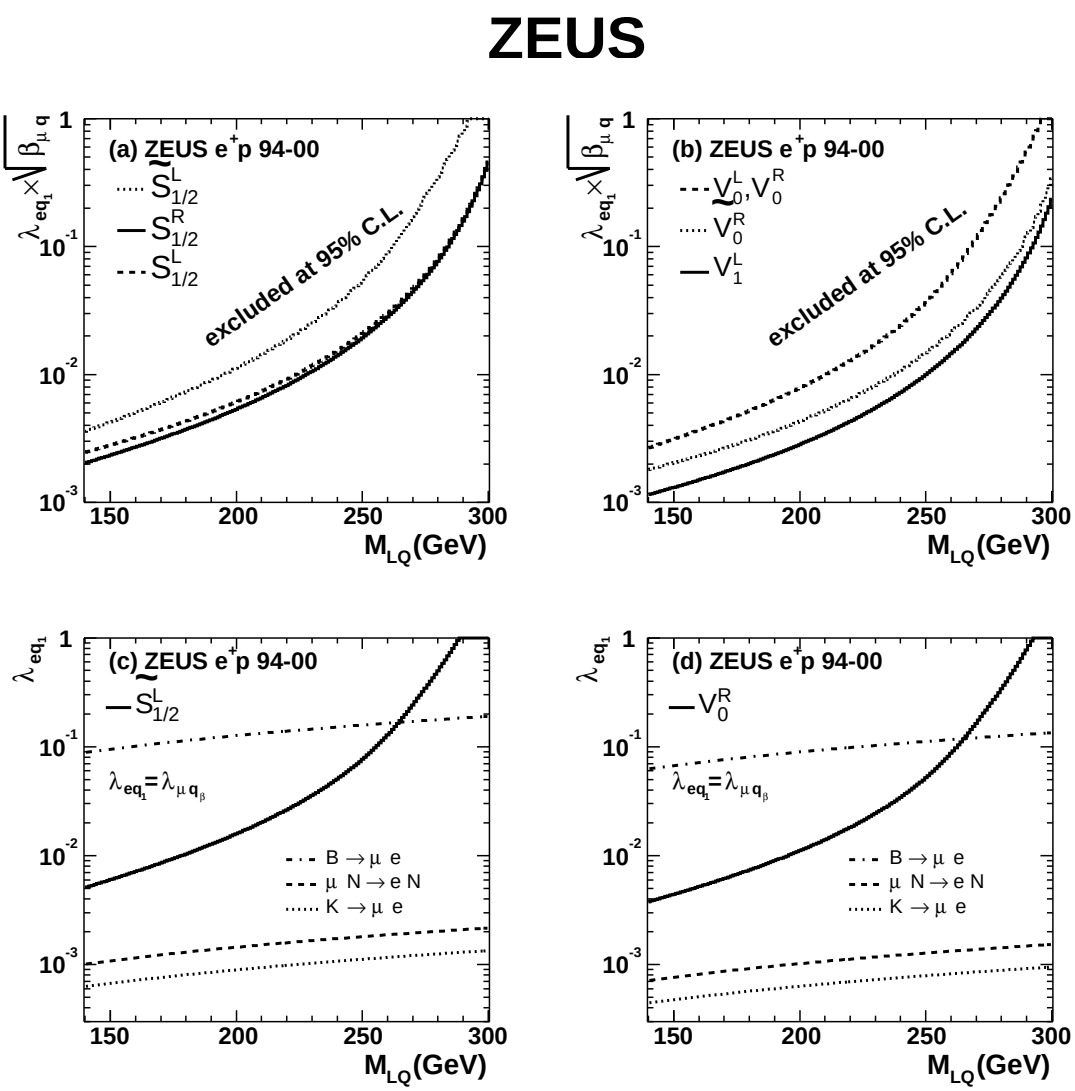

Figure 7.4: Limits for $F = 0$ low-mass LQs in $e - \mu$ transitions obtained from e^+p collisions. The upper plots show 95% C.L. limits on $\lambda_{eq_1}\sqrt{\beta_{\mu q}}$ for (a) scalar and (b) vector LQs. In the lower plots, ZEUS limits on λ_{eq_1} for a representative (c) scalar and (d) vector LQ are compared to the indirect constraints from low-energy experiments [79, 80, 81, 82, 83, 84, 85], assuming $\lambda_{eq_1} = \lambda_{\mu q_\beta}$.

Constraints on $\lambda_{eq_1}\sqrt{\beta_{\ell q}}$ for $\tilde{S}^L_{1/2}$ and for S^L_0 can be interpreted as limits on $\lambda'_{1j1}\sqrt{\beta_{\tilde{u}^j\to\ell q}}$ and $\lambda'_{11k}\sqrt{\beta_{\tilde{d}^k\to\ell q}}$ for $\tilde{u}^j$ and $\tilde{d}^k$ R-Parity-violating squarks of generation j and k, respectively [86].

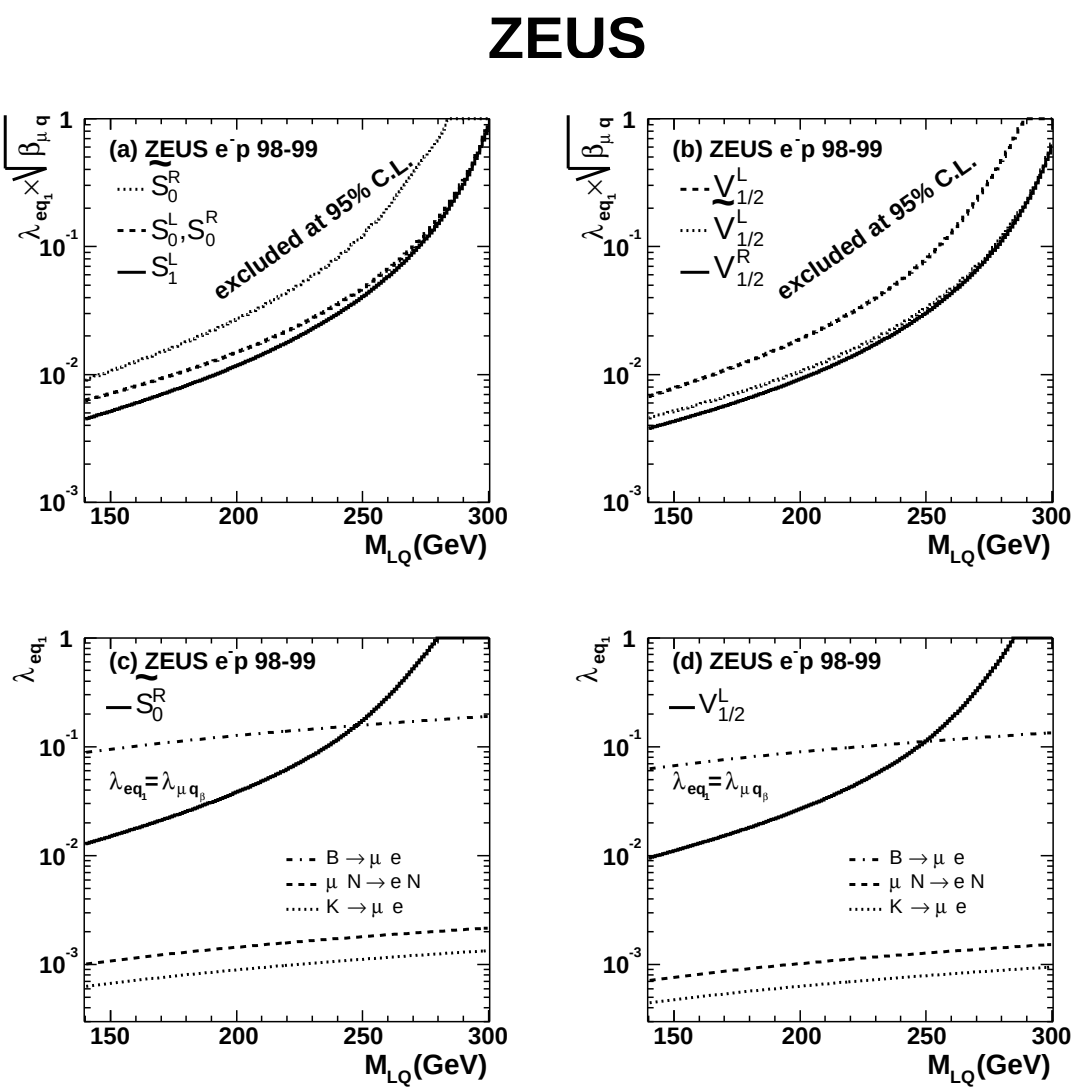

Figure 7.5: Limits for $|F| = 2$ low-mass LQs in $e - \mu$ transitions obtained from $e^- p$ collisions. The upper plots show 95% C.L. limits on $\lambda_{eq_1}\sqrt{\beta_{\mu q}}$ for (a) scalar and (b) vector LQs. In the lower plots, ZEUS limits on λ_{eq_1} for a representative (c) scalar and (d) vector LQ are compared to the indirect constraints from low-energy experiments [79, 80, 81, 82, 83, 84, 85], assuming $\lambda_{eq_1} = \lambda_{\mu q_\beta}$.

7.1.5 High-mass leptoquark and squark limits

Tables 7.5 and 7.6 show the 95% C.L. limits on $\lambda_{eq_\alpha}\lambda_{\mu q_\beta}/M^2_{\mathrm{LQ}}$ (third row of each cell) for $F = 0$ and $|F| = 2$ high-mass leptoquarks coupling to eq_α and μq_β. Limits were evaluated for all combinations of quark generations α, β, except when a coupling

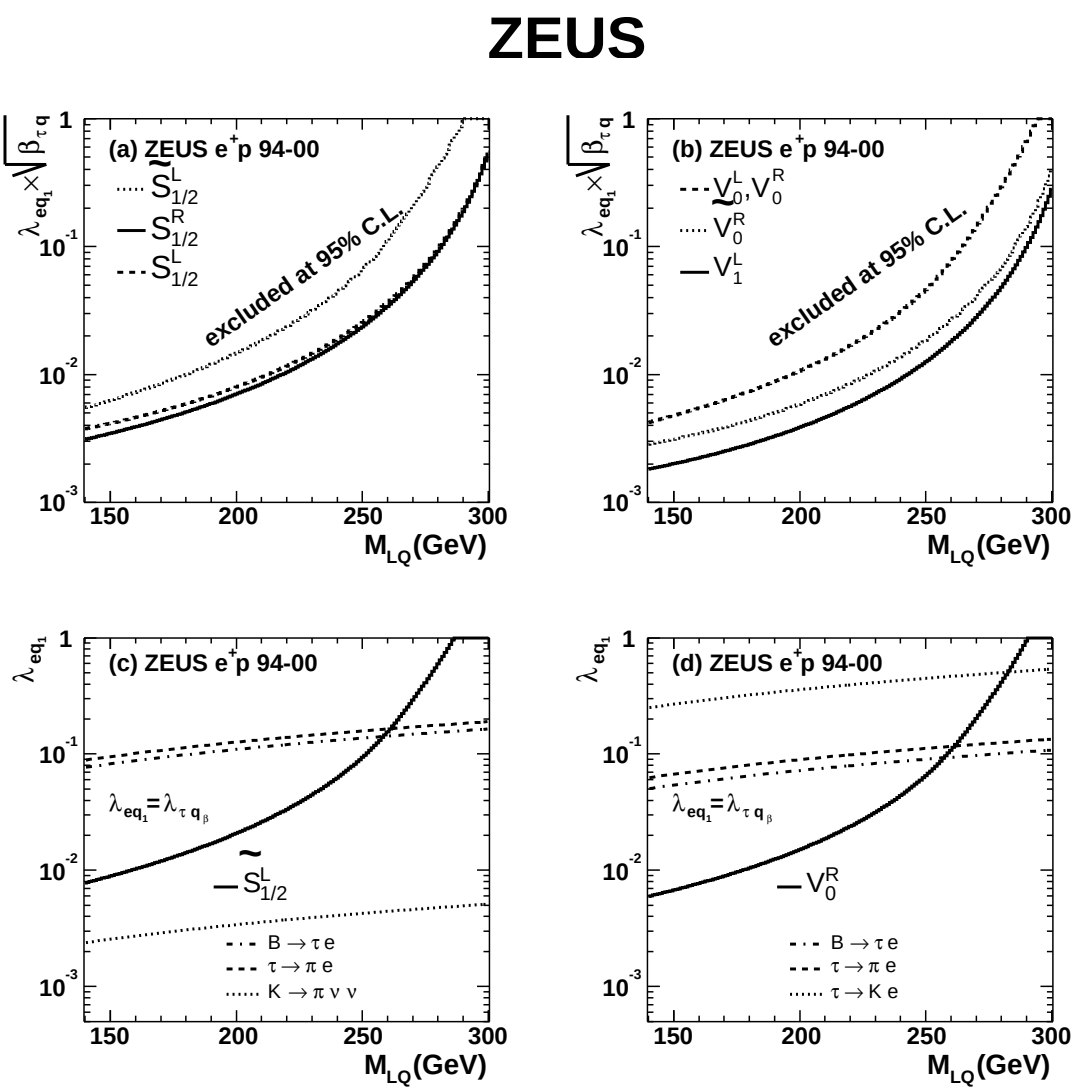

Figure 7.6: Limits for $F = 0$ low-mass LQs in $e - \tau$ transitions obtained from e^+p collisions. The upper plots show 95% C.L. limits on $\lambda_{eq_1}\sqrt{\beta_{\tau q}}$ for (a) scalar and (b) vector LQs. In the lower plots, ZEUS limits on λ_{eq_1} for a representative (c) scalar and (d) vector LQ are compared to the indirect constraints from low-energy experiments [79, 80, 81, 82, 83, 84, 85], assuming $\lambda_{eq_1} = \lambda_{\tau q_\beta}$.

to a t quark is involved. Tables 7.7 and 7.8 show the corresponding limits for LQs coupling to eq_α and τq_β.

Limits for $\tilde{S}^L_{1/2}$ LQs can also be interpreted as limits on $\lambda'_{1j\alpha}\lambda'_{ij\beta}/M^2_{\tilde{u}}$ for a u-type squark of generation j, where $i = 2, 3$ is the generation of the final-state lepton (μ

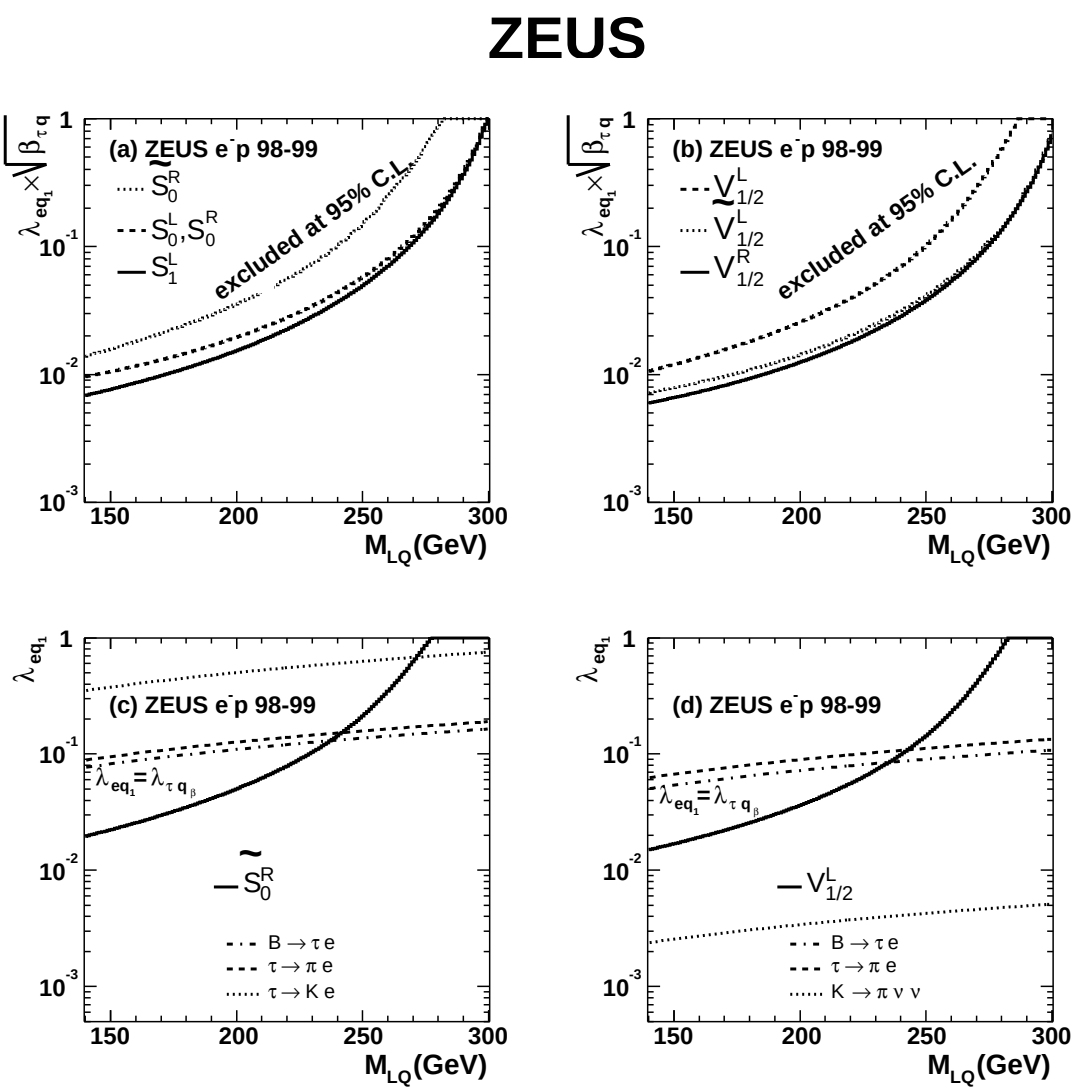

Figure 7.7: Limits for $|F| = 2$ low-mass LQs in $e - \tau$ transitions obtained from $e^- p$ collisions. The upper plots show 95% C.L. limits on $\lambda_{eq_1}\sqrt{\beta_{\tau q}}$ for (a) scalar and (b) vector LQs. In the lower plots, ZEUS limits on λ_{eq_1} for a representative (c) scalar and (d) vector LQ are compared to the indirect constraints from low-energy experiments [79, 80, 81, 82, 83, 84, 85], assuming $\lambda_{eq_1} = \lambda_{\tau q_\beta}$.

or τ). Similarly, limits for S_0^L LQs can also be interpreted as limits on $\lambda'_{1\alpha k}\lambda'_{i\beta k}/M^2_{\tilde{d}}$ for a d-type squark of generation k.

LQ type	S_0^L	S_0^R	$\tilde{S}_0^R$	S_1^L	$V_{1/2}^L$	$V_{1/2}^R$	$\tilde{V}_{1/2}^R$
$e-\mu$ limit on M_{LQ}(GeV)	278	284	261	281	269	289	289
$e-\tau$ limit on M_{LQ}(GeV)	275	281	257	278	265	287	286

Table 7.2: 95% C.L. lower limits on M_{LQ} for $|F| = 2$ LQs mediating $e-\mu$ and $e-\tau$ transitions assuming $\lambda_{eq_1} = \lambda_{\ell q_\beta} = 0.3$.

LQ type	$\tilde{S}_{1/2}^L$	$S_{1/2}^L$	$S_{1/2}^R$	V_0^L/V_0^R	$\tilde{V}_0^R$	V_1^L
$e-\mu$ limit on $\lambda_{eq_1}\sqrt{\beta_{\mu q}}$	0.054	0.021	0.019	0.037	0.015	0.010
$e-\tau$ limit on $\lambda_{eq_1}\sqrt{\beta_{\tau q}}$	0.066	0.026	0.024	0.046	0.019	0.013

Table 7.3: 95% C.L. upper limits on $\lambda_{eq_1}\sqrt{\beta_{\ell q}}$ for $F = 0$ LQs with mass $M_{\mathrm{LQ}} = 250\,\mathrm{GeV}$ mediating $e-\mu$ and the $e-\tau$ transitions.

7.2 Comparison with limits from other experiments

7.2.1 Low-energy experiments

There are many constraints from low-energy experiments on lepton-flavor-violating processes from low-energy experiments on muon scattering and rare lepton or mesons decays [79, 80, 81, 82, 83, 84, 85]. Most of them can be converted into limits on $\lambda_{eq_\alpha}\lambda_{\ell q_\beta}/M_{\mathrm{LQ}}^2$ for massive scalar or vector leptoquark exchange. In Tables 7.5–7.8, limits from such measurements are compared to the constraints from this analysis. For the $e-\mu$ transition, such indirect limits are very stringent and ZEUS limits are better only in a few cases involving the c-quark. In the $e-\tau$ case, ZEUS improves on the existing limits for many initial- and final-state quark combinations, especially when a quark of the second or third generation is involved. Assuming $\lambda_{eq_1} = \lambda_{\ell q_\beta}$, ZEUS limits on low-mass LQs can be compared to limits from low-energy experiments. In Figs. 7.4 and 7.5 limits on λ_{eq_1} as a function of the LQ mass are compared to limits from $e-\mu$ conversion in nuclei and from rare K- and B- meson decays. ZEUS limits are better or competitive with indirect limits up to $\sim 250\,\mathrm{GeV}$ when the quark in the final state is of the third generation. In Figs. 7.6 and 7.7, the corresponding limits for the τ case are shown compared to constraints from rare τ, B or K decays. ZEUS limits improve on low-energy results in most cases.

LQ type	S_0^L/S_0^R	$\tilde{S}_0^R$	S_1^L	$V_{1/2}^L$	$V_{1/2}^R$	$\tilde{V}_{1/2}^R$
$e-\mu$ limit on $\lambda_{eq_1}\sqrt{\beta_{\mu q}}$	0.047	0.12	0.041	0.080	0.030	0.033
$e-\tau$ limit on $\lambda_{eq_1}\sqrt{\beta_{\tau q}}$	0.058	0.15	0.049	0.10	0.038	0.042

Table 7.4: 95% C.L. upper limits on $\lambda_{eq_1}\sqrt{\beta_{\ell q}}$ for $|F| = 2$ LQs with mass $M_{\mathrm{LQ}} = 250\,\mathrm{GeV}$ mediating $e-\mu$ and $e-\tau$ transitions.

7.2.2 LFV and leptoquark searches at colliders

Tevatron limits are complementary to those from HERA since the cross sections at $p\bar{p}$ colliders do not depend on the Yukawa coupling, and LQs are assumed to couple only with one lepton generation. Therefore, such experiments are sensitive to only a subset of the interactions considered here. The CDF and DØ collaborations exclude scalar LQs coupling exclusively to μq with masses up to 202 GeV [87] and 200 GeV [88], respectively. CDF performed an analysis searching for leptoquarks that couple exclusively to the third generation of leptons and excluded LQs with $M_{\mathrm{LQ}} < 99\,\mathrm{GeV}$ if $\beta_{\tau b} = 1$. The DØ collaboration, looking for $\nu\nu bb$ final states, excluded LQs with masses below 94 GeV if $\beta_{\nu b} = 1$. The CDF collaboration also performed a search for a narrow resonance decaying into two charged leptons of different generation [89], observing no deviation from SM expectations.

H1 performed an analysis on lepton-flavor-violating interactions mediated by LQs [90], obtaining limits that are similar to previous ZEUS results [91].

$e \to \mu$	ZEUS $e^{\pm}p$ 1994–2000	$F = 0$

$\alpha\beta$	$S^L_{1/2}$ $e^-\bar{u}$ e^+u	$S^R_{1/2}$ $e^-(\bar{u}+\bar{d})$ $e^+(u+d)$	$\tilde{S}^L_{1/2}$ $e^-\bar{d}$ e^+d	V^L_0 $e^-\bar{d}$ e^+d	V^R_0 $e^-\bar{d}$ e^+d	$\tilde{V}^R_0$ $e^-\bar{u}$ e^+u	V^L_1 $e^-(\sqrt{2}\bar{u}+\bar{d})$ $e^+(\sqrt{2}u+d)$
1 1	$\mu N \to eN$ $5.2 \cdot 10^{-5}$ **1.2**	$\mu N \to eN$ $2.6 \cdot 10^{-5}$ **1.0**	$\mu N \to eN$ $5.2 \cdot 10^{-5}$ **1.7**	$\mu N \to eN$ $2.6 \cdot 10^{-5}$ **1.0**	$\mu N \to eN$ $2.6 \cdot 10^{-5}$ **1.0**	$\mu N \to eN$ $2.6 \cdot 10^{-5}$ **0.8**	$\mu N \to eN$ $0.8 \cdot 10^{-5}$ **0.4**
1 2	$D \to \mu\bar{e}$ 2.4 **1.3**	$K \to \mu\bar{e}$ $2 \cdot 10^{-5}$ **1.0**	$K \to \mu\bar{e}$ $2 \cdot 10^{-5}$ **1.8**	$K \to \mu\bar{e}$ $1 \cdot 10^{-5}$ **1.2**	$K \to \mu\bar{e}$ $1 \cdot 10^{-5}$ **1.2**	$D \to \mu\bar{e}$ 1.2 **1.0**	$K \to \mu\bar{e}$ $1 \cdot 10^{-5}$ **0.5**
1 3	*	$B \to \mu\bar{e}$ 0.4 **1.8**	$B \to \mu\bar{e}$ 0.4 **1.9**	$B \to \mu\bar{e}$ 0.2 **1.5**	$B \to \mu\bar{e}$ 0.2 **1.5**	*	$B \to \mu\bar{e}$ 0.2 **1.5**
2 1	$D \to \mu\bar{e}$ 2.4 **3.6**	$K \to \mu\bar{e}$ $2 \cdot 10^{-5}$ **2.4**	$K \to \mu\bar{e}$ $2 \cdot 10^{-5}$ **3.1**	$K \to \mu\bar{e}$ $1 \cdot 10^{-5}$ **1.3**	$K \to \mu\bar{e}$ $1 \cdot 10^{-5}$ **1.3**	$D \to \mu\bar{e}$ 1.2 **1.2**	$K \to \mu\bar{e}$ $1 \cdot 10^{-5}$ **0.6**
2 2	$\mu N \to eN$ $9.2 \cdot 10^{-4}$ **5.7**	$\mu N \to eN$ $1.3 \cdot 10^{-3}$ **3.1**	$\mu N \to eN$ $3 \cdot 10^{-3}$ **3.8**	$\mu N \to eN$ $1.5 \cdot 10^{-3}$ **1.9**	$\mu N \to eN$ $1.5 \cdot 10^{-3}$ **1.9**	$\mu N \to eN$ $4.6 \cdot 10^{-4}$ **2.8**	$\mu N \to eN$ $2.7 \cdot 10^{-4}$ **1.1**
2 3	*	$B \to \bar{\mu}eK$ 0.3 **4.3**	$B \to \bar{\mu}eK$ 0.3 **4.2**	$B \to \bar{\mu}eK$ 0.15 **2.9**	$B \to \bar{\mu}eK$ 0.15 **2.9**	*	$B \to \bar{\mu}eK$ 0.15 **2.9**
3 1	*	$B \to \mu\bar{e}$ 0.4 **4.4**	$B \to \mu\bar{e}$ 0.4 **4.4**	V_{ub} 0.12 **1.5**	$B \to \mu\bar{e}$ 0.2 **1.5**	*	V_{ub} 0.12 **1.5**
3 2	*	$B \to \bar{\mu}eK$ 0.3 **5.8**	$B \to \bar{\mu}eK$ 0.3 **5.8**	$B \to \bar{\mu}eK$ 0.15 **2.2**	$B \to \bar{\mu}eK$ 0.15 **2.2**	*	$B \to \bar{\mu}eK$ 0.15 **2.2**
3 3	*	$\mu N \to eN$ $1.3 \cdot 10^{-3}$ **7.6**	$\mu N \to eN$ $3 \cdot 10^{-3}$ **7.6**	$\mu N \to eN$ $1.5 \cdot 10^{-3}$ **3.9**	$\mu N \to eN$ $1.5 \cdot 10^{-3}$ **3.9**	*	$\mu N \to eN$ $2.7 \cdot 10^{-4}$ **3.9**

Table 7.5: Limits at 95% C.L. on $\frac{\lambda_{eq_\alpha}\lambda_{\mu q_\beta}}{M^2_{LQ}}$ for $F = 0$ LQs, in units of TeV^{-2}. The first column indicates the quark generations coupling to $LQ-e$ and $LQ-\mu$, respectively. ZEUS results are reported in the third line (bold) of each cell. The low-energy process providing the most stringent constraint and the corresponding limit are shown in the first and second lines. The ZEUS limits are enclosed in a box if they are better than the low-energy constraints. The cases marked with * correspond to processes where the coupling to a t quark is involved.

$e \to \mu$	ZEUS $e^{\pm}p$ 1994–2000						$\lvert F\rvert = 2$
$\alpha\beta$	S_0^L	S_0^R	$\tilde{S}_0^R$	S_1^L	$V_{1/2}^L$	$V_{1/2}^R$	$\tilde{V}_{1/2}^L$
	e^-u $e^+\bar{u}$	e^-u $e^+\bar{u}$	e^-d $e^+\bar{d}$	$e^-(u+\sqrt{2}d)$ $e^+(\bar{u}+\sqrt{2}\bar{d})$	e^-d $e^+\bar{d}$	$e^-(u+d)$ $e^+(\bar{u}+\bar{d})$	e^-u $e^+\bar{u}$
1 1	$\mu N \to eN$ $5.2 \cdot 10^{-5}$ **1.6**	$\mu N \to eN$ $5.2 \cdot 10^{-5}$ **1.6**	$\mu N \to eN$ $5.2 \cdot 10^{-5}$ **2.1**	$\mu N \to eN$ $1.7 \cdot 10^{-5}$ **0.9**	$\mu N \to eN$ $2.6 \cdot 10^{-5}$ **0.9**	$\mu N \to eN$ $1.3 \cdot 10^{-5}$ **0.5**	$\mu N \to eN$ $2.6 \cdot 10^{-5}$ **0.6**
1 2	$K \to \pi\nu\bar{\nu}$ 10^{-3} **2.5**	$D \to \mu\bar{e}$ 2.4 **2.5**	$K \to \mu\bar{e}$ $2 \cdot 10^{-5}$ **2.6**	$K \to \mu\bar{e}$ $1 \cdot 10^{-5}$ **1.2**	$K \to \mu\bar{e}$ $1 \cdot 10^{-5}$ **1.6**	$K \to \mu\bar{e}$ $1 \cdot 10^{-5}$ **1.2**	$D \to \mu\bar{e}$ 1.2 **1.8**
1 3	*	*	$B \to \mu\bar{e}$ 0.4 **2.9**	V_{ub} 0.24 **1.4**	$B \to \mu\bar{e}$ 0.2 **2.2**	$B \to \mu\bar{e}$ 0.2 **2.2**	*
2 1	$K \to \pi\nu\bar{\nu}$ 10^{-3} **2.1**	$D \to \mu\bar{e}$ 2.4 **2.1**	$K \to \mu\bar{e}$ $2 \cdot 10^{-5}$ **2.5**	$K \to \mu\bar{e}$ $1 \cdot 10^{-5}$ **1.1**	$K \to \mu\bar{e}$ $1 \cdot 10^{-5}$ **0.9**	$K \to \mu\bar{e}$ $1 \cdot 10^{-5}$ **0.5**	$D \to \mu\bar{e}$ 1.2 **0.6**
2 2	$\mu N \to eN$ $9.2 \cdot 10^{-4}$ **5.7**	$\mu N \to eN$ $9.2 \cdot 10^{-4}$ **5.7**	$\mu N \to eN$ $3 \cdot 10^{-3}$ **3.8**	$\mu N \to eN$ $2.5 \cdot 10^{-3}$ **1.8**	$\mu N \to eN$ $1.5 \cdot 10^{-3}$ **1.9**	$\mu N \to eN$ $6.7 \cdot 10^{-4}$ **1.6**	$\mu N \to eN$ $4.6 \cdot 10^{-4}$ **2.8**
2 3	*	*	$B \to \bar{\mu}eK$ 0.3 **4.4**	$B \to \bar{\mu}eK$ 0.15 **2.2**	$B \to \bar{\mu}eK$ 0.15 **2.9**	$B \to \bar{\mu}eK$ 0.15 **2.9**	*
3 1	*	*	$B \to \mu\bar{e}$ 0.4 **3.1**	$B \to \mu\bar{e}$ 0.4 **1.5**	$B \to \mu\bar{e}$ 0.2 **0.9**	$B \to \mu\bar{e}$ 0.2 **0.9**	*
3 2	*	*	$B \to \bar{\mu}eK$ 0.3 **5.9**	$B \to \bar{\mu}eK$ 0.15 **3.0**	$B \to \bar{\mu}eK$ 0.15 **2.2**	$B \to \bar{\mu}eK$ 0.15 **2.2**	*
3 3	*	*	$\mu N \to eN$ $3 \cdot 10^{-3}$ **7.7**	$\mu N \to eN$ $2.5 \cdot 10^{-3}$ **3.9**	$\mu N \to eN$ $1.5 \cdot 10^{-3}$ **4.0**	$\mu N \to eN$ $6.7 \cdot 10^{-4}$ **4.0**	*

Table 7.6: Limits at 95% C.L. on $\frac{\lambda_{eq_\alpha}\lambda_{\mu q_\beta}}{M_{LQ}^2}$ for $|F| = 2$ LQs, in units of TeV^{-2}. The first column indicates the quark generations coupling to $LQ-e$ and $LQ-\mu$, respectively. ZEUS results are reported in the third line (bold) of each cell. The low-energy process providing the most stringent constraint and the corresponding limit are shown in the first and second lines. The ZEUS limits are enclosed in a box if they are better than the low-energy constraints. The cases marked with * correspond to processes where the coupling to a t quark is involved.

$e \to \tau$	ZEUS $e^{\pm}p$ 1994–2000					$F = 0$	
$\alpha\beta$	$S^L_{1/2}$ $e^-\bar{u}$ e^+u	$S^R_{1/2}$ $e^-(\bar{u}+\bar{d})$ $e^+(u+d)$	$\tilde{S}^L_{1/2}$ $e^-\bar{d}$ e^+d	V^L_0 $e^-\bar{d}$ e^+d	V^R_0 $e^-\bar{d}$ e^+d	$\tilde{V}^R_0$ $e^-\bar{u}$ e^+u	V^L_1 $e^-(\sqrt{2}\bar{u}+\bar{d})$ $e^+(\sqrt{2}u+d)$
1 1	$\tau \to \pi e$ 0.4 **1.8**	$\tau \to \pi e$ 0.2 **1.5**	$\tau \to \pi e$ 0.4 **2.7**	$\tau \to \pi e$ 0.2 **1.7**	$\tau \to \pi e$ 0.2 **1.7**	$\tau \to \pi e$ 0.2 **1.3**	$\tau \to \pi e$ 0.06 **0.6**
1 2	**1.9**	$\tau \to Ke$ 6.3 **1.6**	$K \to \pi\nu\bar{\nu}$ $5.8 \cdot 10^{-4}$ **2.9**	$\tau \to Ke$ 3.2 **2.1**	$\tau \to Ke$ 3.2 **2.1**	**1.6**	$K \to \pi\nu\bar{\nu}$ $1.5 \cdot 10^{-4}$ **0.8**
1 3	*	$B \to \tau\bar{e}$ 0.3 **3.2**	$B \to \tau\bar{e}$ 0.3 **3.3**	$B \to \tau\bar{e}$ 0.13 **2.6**	$B \to \tau\bar{e}$ 0.13 **2.6**	*	$B \to \tau\bar{e}$ 0.13 **2.6**
2 1	**6.0**	$\tau \to Ke$ 6.3 **4.1**	$K \to \pi\nu\bar{\nu}$ $5.8 \cdot 10^{-4}$ **5.2**	$\tau \to Ke$ 3.2 **2.3**	$\tau \to Ke$ 3.2 **2.3**	**2.1**	$K \to \pi\nu\bar{\nu}$ $1.5 \cdot 10^{-4}$ **0.9**
2 2	$\tau \to 3e$ 5 **10**	$\tau \to 3e$ 8 **5.6**	$\tau \to 3e$ 17 **6.5**	$\tau \to 3e$ 9 **3.4**	$\tau \to 3e$ 9 **3.4**	$\tau \to 3e$ 3 **5.5**	$\tau \to 3e$ 1.6 **2.1**
2 3	*	$B \to \tau\bar{e}X$ 14 **8.1**	$B \to \tau\bar{e}X$ 14 **7.8**	$B \to \tau\bar{e}X$ 7.2 **5.5**	$B \to \tau\bar{e}X$ 7.2 **5.5**	*	$B \to \tau\bar{e}X$ 7.2 **5.5**
3 1	*	$B \to \tau\bar{e}$ 0.3 **7.8**	$B \to \tau\bar{e}$ 0.3 **7.2**	V_{ub} 0.12 **2.5**	$B \to \tau\bar{e}$ 0.13 **2.5**	*	V_{ub} 0.12 **2.5**
3 2	*	$B \to \tau\bar{e}X$ 14 **11**	$B \to \tau\bar{e}X$ 14 **10**	$B \to \tau\bar{e}X$ 7.2 **4.2**	$B \to \tau\bar{e}X$ 7.2 **4.2**	*	$B \to \tau\bar{e}X$ 7.2 **4.2**
3 3	*	$\tau \to 3e$ 8 **15**	$\tau \to 3e$ 17 **14**	$\tau \to 3e$ 9 **8.1**	$\tau \to 3e$ 9 **8.1**	*	$\tau \to 3e$ 1.6 **8.1**

Table 7.7: Limits at 95% C.L. on $\frac{\lambda_{eq_\alpha}\lambda_{\tau q_\beta}}{M^2_{LQ}}$ for $F = 0$ LQs, in units of TeV^{-2}. The first column indicates the quark generations coupling to $LQ-e$ and $LQ-\tau$, respectively. ZEUS results are reported in the third line (bold) of each cell. The low-energy process providing the most stringent constraint and the corresponding limit are shown in the first and second lines. The ZEUS limits are enclosed in a box if they are better than the low-energy constraints. The cases marked with * correspond to processes where the coupling to a t quark is involved.

$e \to \tau$			ZEUS $e^{\pm}p$ 1994–2000			$\lvert F\rvert = 2$	
$\alpha\beta$	S_0^L e^-u $e^+\bar{u}$	S_0^R e^-u $e^+\bar{u}$	$\tilde{S}_0^R$ e^-d $e^+\bar{d}$	S_1^L $e^-(u+\sqrt{2}d)$ $e^+(\bar{u}+\sqrt{2}\bar{d})$	$V_{1/2}^L$ e^-d $e^+\bar{d}$	$V_{1/2}^R$ $e^-(u+d)$ $e^+(\bar{u}+\bar{d})$	$\tilde{V}_{1/2}^L$ e^-u $e^+\bar{u}$
	G_F	$\tau \to \pi e$	$\tau \to \pi e$	$\tau \to \pi e$	$\tau \to \pi e$	$\tau \to \pi e$	$\tau \to \pi e$
1 1	0.3 **2.5**	0.4 **2.5**	0.4 **3.5**	0.1 **1.4**	0.2 **1.4**	0.1 **0.8**	0.2 **1.0**
1 2	$K \to \pi\nu\bar{\nu}$ $5.8 \cdot 10^{-4}$ **4.0**	**4.0**	$\tau \to Ke$ 6.3 **4.4**	$K \to \pi\nu\bar{\nu}$ $2.9 \cdot 10^{-4}$ **1.9**	$K \to \pi\nu\bar{\nu}$ $2.9 \cdot 10^{-4}$ **2.8**	$\tau \to Ke$ 3.2 **2.0**	**3.1**
1 3	*	*	$B \to \tau\bar{e}$ 0.3 **5.1**	V_{ub} 0.12 **2.6**	$B \to \tau\bar{e}$ 0.13 **4.0**	$B \to \tau\bar{e}$ 0.13 **4.0**	*
2 1	$K \to \pi\nu\bar{\nu}$ $5.8 \cdot 10^{-4}$ **3.2**	**3.2**	$\tau \to Ke$ 6.3 **4.3**	$K \to \pi\nu\bar{\nu}$ $2.9 \cdot 10^{-4}$ **1.8**	$K \to \pi\nu\bar{\nu}$ $2.9 \cdot 10^{-4}$ **1.4**	$\tau \to Ke$ 3.2 **0.8**	**1.0**
2 2	$\tau \to 3e$ 5 **10**	$\tau \to 3e$ 5 **10**	$\tau \to 3e$ 17 **6.5**	$\tau \to 3e$ 14 **3.2**	$\tau \to 3e$ 9 **3.5**	$\tau \to 3e$ 4 **2.8**	$\tau \to 3e$ 3 **5.1**
2 3	*	*	$B \to \tau\bar{e}X$ 14 **8.3**	$B \to \tau\bar{e}X$ 7.2 **4.1**	$B \to \tau\bar{e}X$ 7.2 **5.4**	$B \to \tau\bar{e}X$ 7.2 **5.4**	*
3 1	*	*	$B \to \tau\bar{e}$ 0.3 **5.3**	$B \to \tau\bar{e}$ 0.13 **2.7**	$B \to \tau\bar{e}$ 0.13 **1.6**	$B \to \tau\bar{e}$ 0.13 **1.6**	*
3 2	*	*	$B \to \tau\bar{e}X$ 14 **11**	$B \to \tau\bar{e}X$ 7.2 **5.5**	$B \to \tau\bar{e}X$ 7.2 **4.1**	$B \to \tau\bar{e}X$ 7.2 **4.1**	*
3 3	*	*	$\tau \to 3e$ 17 **15**	$\tau \to 3e$ 14 **7.6**	$\tau \to 3e$ 9 **7.6**	$\tau \to 3e$ 4 **7.6**	*

Table 7.8: Limits at 95% C.L. on $\frac{\lambda_{eq_\alpha}\lambda_{\tau q_\beta}}{M_{LQ}^2}$ for $|F| = 2$ LQs, in units of TeV^{-2}. The first column indicates the quark generations coupling to $LQ-e$ and $LQ-\tau$, respectively. ZEUS results are reported in the third line (bold) of each cell. The low-energy process providing the most stringent constraint and the corresponding limit are shown in the first and second lines. The ZEUS limits are enclosed in a box if they are better than the low-energy constraints. The cases marked with * correspond to processes where the coupling to a t quark is involved.

Chapter 8

HERA and ZEUS upgrade

As anticipated in chapter 2, during a long shutdown started in 2000 and ended in 2001, both the HERA collider and the ZEUS detector were upgraded. The upgrade has also triggered new software projects, the main one being the new event display for ZEUS, called ZeVis. In this chapter, after an overview of the HERA and ZEUS upgrade, ZeVis is described. During this thesis work, the implementation of the BAC detector and of the trigger bits in ZeVis has been performed. The last section of the chapter is dedicated to the data quality monitor, which has also been part of my activity in ZEUS.

8.1 The HERA upgrade

After several years of operation HERA reached a luminosity of $1.4 \cdot 10^{31}\,\mathrm{cm}^{-2}\mathrm{s}^{-1}$, which is very close to the design luminosity of the accelerator. The luminosity collected by the H1 and ZEUS experiments permitted to achieve many physics goals. An upgrade was carried out during the years 2000–2001 in order to increase the luminosity and, thus, to improve the sensitivity to new physics and to high-Q^2 phenomena. The aim of HERA II is to reach a luminosity a factor 5 higher with respect to HERA I.

As it can be seen from Eq. (2.2) the luminosity can be increased either injecting bunches with higher number of particles, which means higher currents, or reducing the size of the beam cross section. Four super-conducting focusing magnets installed during the 2000–2001 shutdown permitted to reduce the size of the beam ($\sigma_x \times \sigma_y$) from 190 μm $\times$ 50 μm to 112 μm $\times$ 30 μm. The maximum luminosity reached during the 2004 data taking is $3.8 \cdot 10^{31}\,\mathrm{cm}^{-2}\mathrm{s}^{-1}$. Figure 8.1 shows the luminosity delivered by HERA in the 2002–2004 years and collected by ZEUS. During the shutdown two spin rotators were installed before the H1 and ZEUS interaction points (Fig. 8.2) in order to polarize longitudinally the electron beam. Since the weak interaction

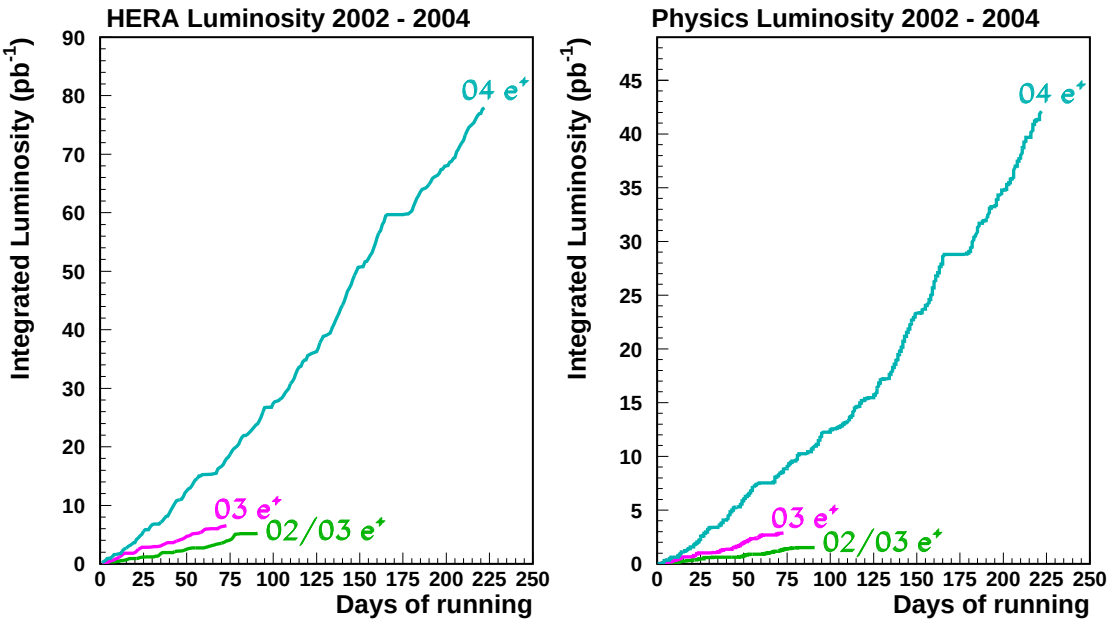

(a) (b)

Figure 8.1: (a) Integrated luminosity delivered by HERA in the 2002–2004 years; (b) integrated luminosity collected by ZEUS during the HERA II data taking.

depends on the helicity of the particles, the polarization of electrons provides a new tool to study and test the Standard Model. The dependence of the NC and CC DIS cross section on the polarization of the electron beam, for example, is significant and it has been already mentioned in Sec. 1.1.3.

8.2 The ZEUS upgrade

During the shutdown two additional detector components were installed in order to improve the track and the vertex reconstruction: the micro-vertex detector (MVD) and the straw tube tracker (STT). An upgrade of the luminosity detector was also performed.

8.2.1 The micro-vertex detector

As already stated in Sec. 2.2, since the 1995, when the VTX was removed, ZEUS lacked of a dedicated vertex detector and the reconstruction of the primary vertex relied mainly on the CTD tracking information. During the shutdown for the HERA

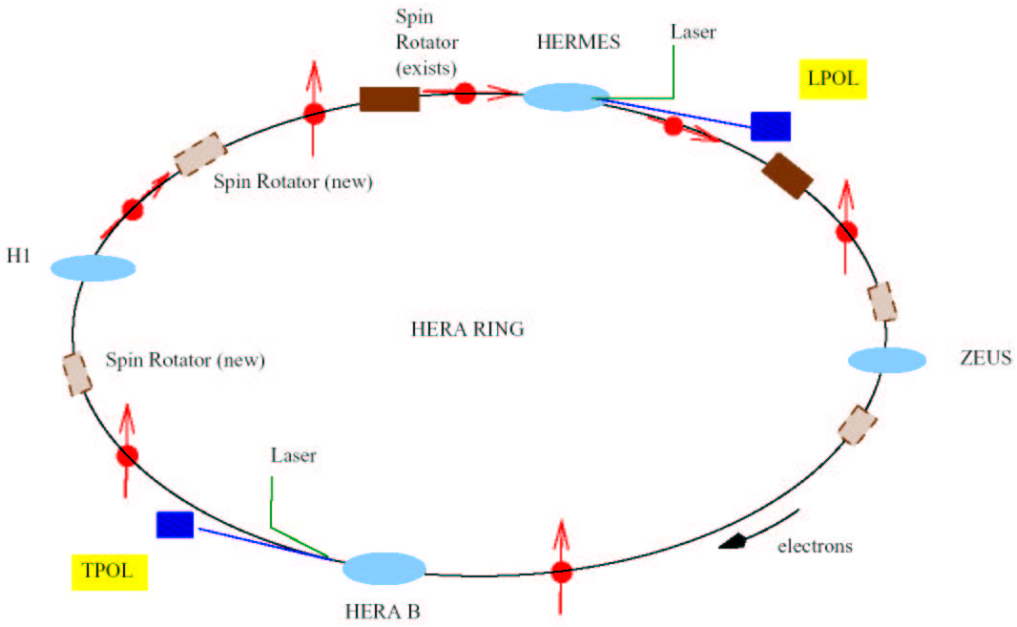

Figure 8.2: Location of the spin rotators on the HERA ring.

upgrade, a new vertex detector, the MVD, was installed between the CTD and the beam pipe. The MVD [92], which covers the polar-angle region $10° < \theta < 160°$, is a single-sided silicon micro-strip detector and it consists of two parts: the barrel and the forward detector. The detector provides a better reconstruction of the primary vertex and of the tracks and the determination of the secondary vertices, which is of particular interest for the tagging of heavy-flavored particle decays.

Barrel MVD layout

The MVD barrel section is about 640 mm long; it is composed of three layers in order to have the possibility to measure the track momenta. The first layer follows the elliptical shape of the beam pipe and it is placed with a radial coordinate $r \sim 3 - 5$ cm from the CTD axis[1]. The second and the third layers have a circular shape and they are placed at $r \sim 8.6$ cm and $r \sim 12.3$ cm, respectively. A cross section in the $X - Y$ plane of the barrel MVD is shown in Fig. 8.3(a).

The basic element of the detector is the sensor which is made by a n-type silicon 300 μm thick with a 64×64 mm^2 section. One side of the sensor is n^+ doped, while the opposite face is covered by p^+ doped strips. The strips are separated at a

[1]After the 2000 shutdown the x and y coordinates of the interaction point do not coincide with the position of the CTD axis, but they are slightly shifted ($x \sim 1.8$ cm and $y \sim 0.16$ cm).

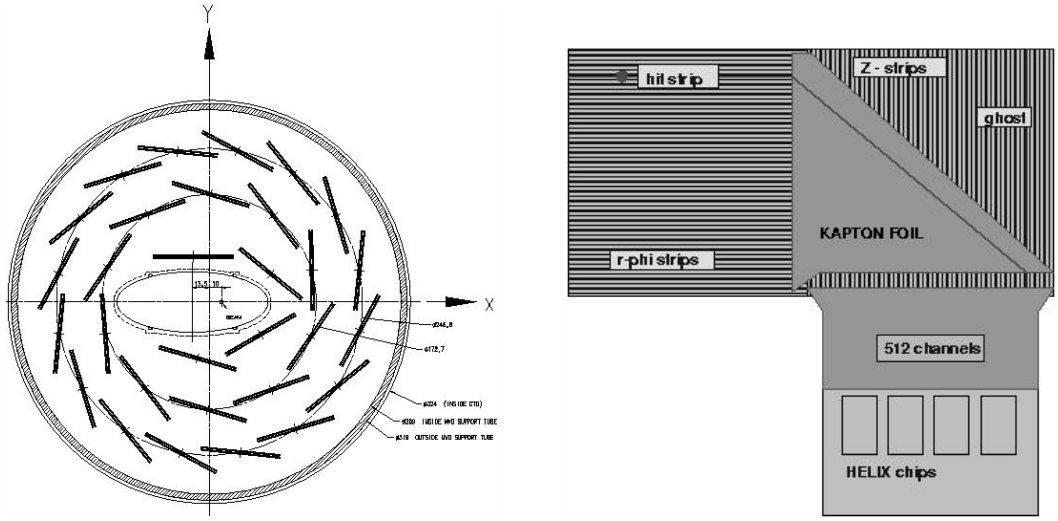

(a) (b)

Figure 8.3: (a) Schematic view of the barrel MVD in the $X-Y$ projection; (b) schematic view of a MVD barrel half module.

pitch of 20 μm and one every sixth strip is AC coupled with an aluminum readout line. The total number of readout channels is 512. Two sensors are glued together orthogonally to form a half module (shown in Fig. 8.3(b)) and their readout strips are connected. In order to reduce the dead area, the two detectors have a small overlap. Two half modules placed on top of each other form a module, allowing for the reconstruction of the two coordinates $r-\phi$ and $r-z$ as their strips are orthogonal to each other. Five modules are placed on a support ladder, for a total of 30 ladders as shown in the transverse plane in Fig. 8.3(a).

Forward MVD layout

The forward MVD detector is made of four wheels. Each wheel (see Fig. 8.4(a)) consists of two planes of 14 sensors. Each sensor has a trapezoidal shape and contains 480 readout strips. The two planes have strips tilted with respect to each other in order to reconstruct two coordinates. The sensors are slightly overlapping to reduce the dead regions. The wheels are placed at $z = 32$, 45, 47 and 75 cm.

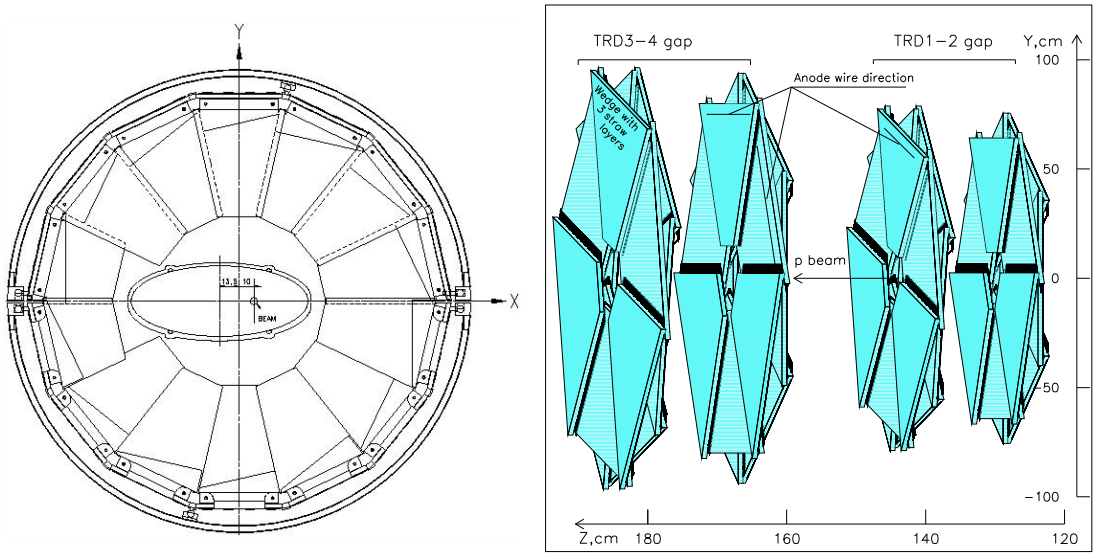

(a) (b)

Figure 8.4: (a) View of one forward MVD wheel in the $X - Y$ projection; (b) schematic view of the STT detector.

8.2.2 The STT detector

With the increased HERA II luminosity a larger number of NC high-Q^2 events, in which the electron is scattered in the forward direction, is expected. Moreover, the decay products of heavy particles in beyond-Standard-Model theories are boosted into the forward direction, due to the beam energy asymmetry. Therefore, it is important to have a good track reconstruction in low polar angle regions. For this reason, during the 2000 shutdown, a new tracking detector, the STT, shown in Fig. 8.4(b), has been installed in the forward region. The STT consists of four superlayers of straw drift tubes. Each superlayer contains two planes and each plane is made of 6 sectors. A sector consists of three layers of straw tubes. In a sector there are between 196 and 280 straws oriented in the azimuthal direction providing a good reconstruction of the radial coordinate of the tracks. The polar angle acceptance of the STT is $5° < \theta < 25°$.

8.2.3 The luminosity monitor

The luminosity measurement at HERA II has to cope with an increased amount of synchrotron radiation with respect to HERA I, making it necessary an upgrade of the luminosity monitor. The new components, which replaced the old ones, give

complementary measurements and checks on the luminosity:

- a new photon calorimeter, shielded from the synchrotron radiation by an active filter;
- an electromagnetic calorimeter placed at 6 meters from the interaction point which can be used to check the acceptance of the photon calorimeter;
- a spectrometer which provides an independent measurement of the luminosity.

8.3 The ZeVis event display

Event displays are an important tool for large experiments in high energy physics. They help in understanding the physics behind the events, and to visualize the geometrical arrangement of the detectors and the topology of physical processes. Moreover they are indispensable to diagnose the apparatus and to monitor the data taking. In order to fulfill these different requirements the program should be versatile and offer both 2-dimensional and 3-dimensional representations. The application must be able to let the user access the events whatever the workstation is, on site or in some other place of the world. The installation of two new detectors during the shutdown, the MVD and the STT, made it necessary the inclusion of these new component in the ZEUS event display. The old event display had a monolithic structure, and it was not well portable on the new Linux machines. Therefore it was decided to write a new and more flexible program, ZeVis (ZEUS visualization) [93], which is written in C++ and makes use of the ROOT [94] libraries.

8.3.1 The program structure

The program is based on a client-server concept that is schematically shown in Fig. 8.5. The server is a software running on a machine with a fast access to the event storage and it is provided with all the libraries and databases needed to perform the reconstruction of the events. The client is mainly a graphical application, which displays to the final user the data obtained from the server. Such application is independent of the internal ZEUS libraries and it can be thus easily installed on any Linux platform. The information needed to visualize an event can be divided into a persistent one, which contains the geometry of the ZEUS detector, and into an event-dependent one, which contains all the physical objects. The file with the geometry is loaded from the server only at the start-up of the client, while the event data can be accessed by exploiting the different server functionalities shown in Fig. 8.5. The communication between the client and the server is done by the HTTP protocol and the files are in the ROOT format.

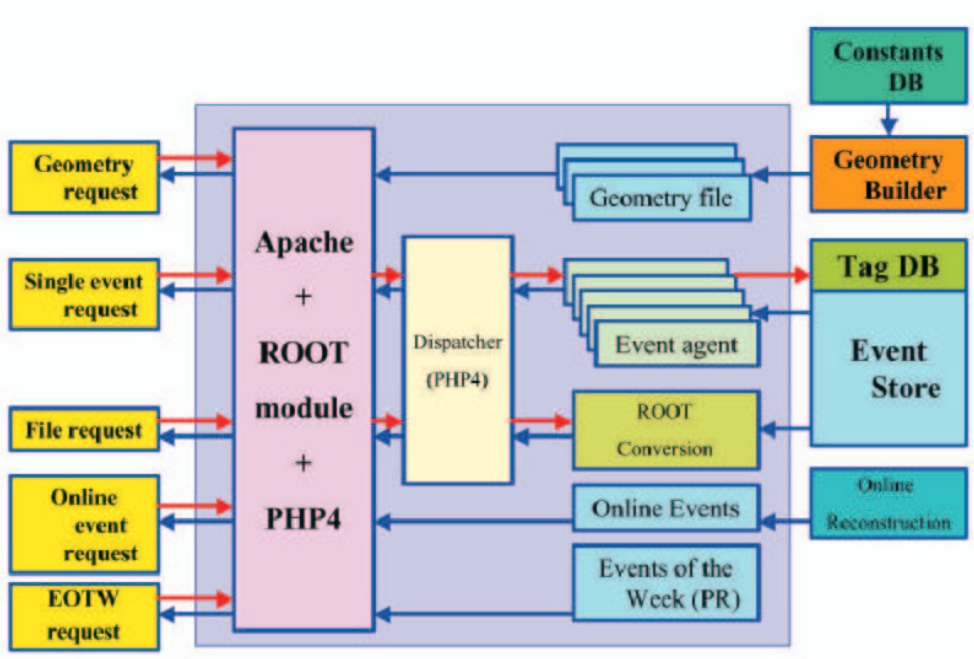

Figure 8.5: Internal structure of the ZeVis server.

For example, when the user asks for an event specifying the run and event number ("single event request" in Fig. 8.5), the request is sent to an event agent, which makes use of the ZEUS database [95] to retrieve the selected event. The event agent is a standard analysis program, which is pre-initialized to reduce the time needed for the event reconstruction. Several event agents run in parallel waiting for possible requests from many users, thus allowing for a faster response of the program. The produced file, containing the event information, is then sent back to the client and visualized. Besides run number and event number the user can also select events by cutting on physical quantities using all the functionalities of the ZEUS event database.

In addition the server offers other useful services as shown in Fig. 8.5:

File request. The client can also download a file from the event store. The server provides the on-the-fly conversion into the ROOT format of the requested file which can be in one of the various ZEUS formats, including raw data.

Online event request. During the data taking it is possible to monitor the data quality using also the event display; random events are sent to a dedicated machine for the reconstruction and the output file can be periodically loaded and visualized by the client.

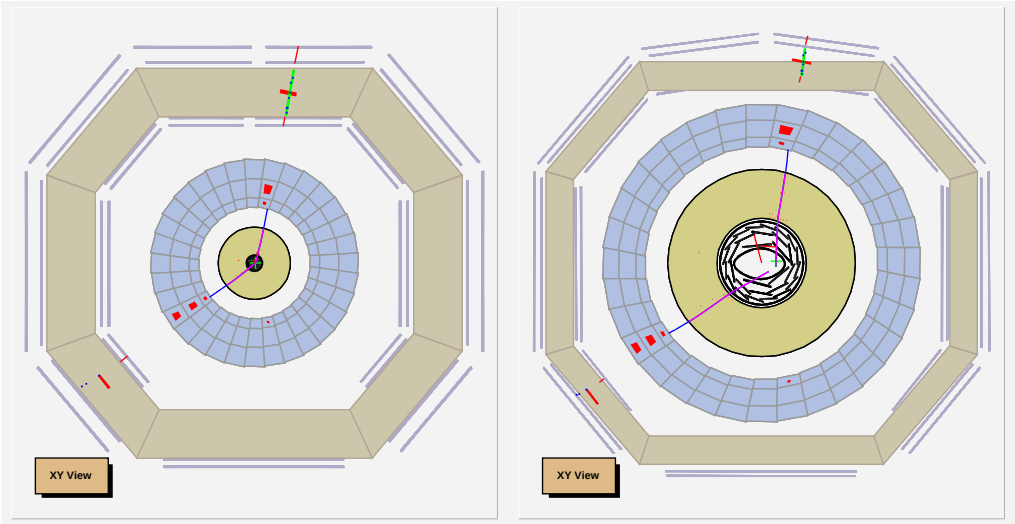

Figure 8.6: Comparison between the linear and the fish-eye view for the XY projection. The event is a muon pair production.

EOTW request. This service permits to access to a collection of events of physical interest selected by the event of the week (EOTW) team. The EOTW is part of the high-Q^2 group data quality monitor described at the end of this chapter (Sec. 8.4).

The client can work also in a stand-alone mode; in this case the file with the geometry and the file with the events need be loaded manually by the user.

The client provides different visualization modes for the geometry and for the events: one 3-dimensional view and two 2-dimensional layered projections, XY and ZR.[2] Layered projections are the most suitable for the analysis since all the relevant physical information is displayed on top of the geometry shapes without being hidden by the detector surfaces. The "fish-eye" view (see Fig. 8.6), which is a non-linear transformation of the coordinates, allows for a simultaneous inspection of the micro-vertex detector and the outer muon chambers, both in the XY and the ZR view. The geometry and the event information for the different detectors can be activated and deactivated independently. These and other visualization options can be saved by the user and (automatically) restored at the next startup of the program.

During this work, the BAC detector geometry and its various readouts (see Sec. 2.5) were implemented from scratch in ZeVis, at both the server and the client

[2]The R coordinate is defined as $R = \sqrt{X^2 + Y^2}$. The sign of R is positive for the azimuthal region selected by the user (default $0° - 180°$), negative in the complementary region.

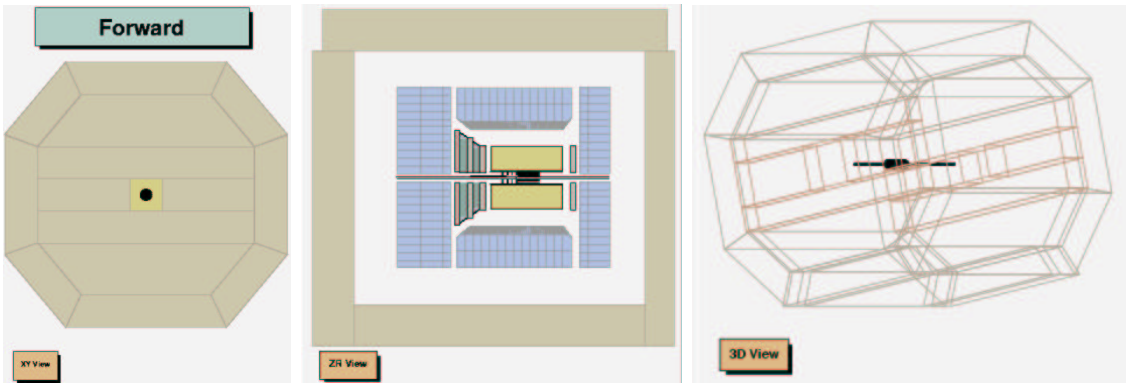

(a) (b) (c)

Figure 8.7: BAC geometry according to the (a) XY, and (b) ZR view projections and (c) in the 3D view.

level. Moreover, the SLT and TLT trigger bit information has been added in the ZeVis header.

8.3.2 The BAC implementation in ZeVis

The BAC geometry

The 3-dimensional BAC geometry is stored in ADAMO [64] tables using a volume description based on the standard primitives of GEANT [63]. The standard way to access these tables is to use calls to a dedicated FORTRAN library. The first step was the realization of an interface class for reading the geometry data and building the 3-dimensional graphical objects corresponding to the BAC geometry. The visualization of the 3D shapes is performed at the client level using standard facilities provided by the ROOT framework. The XY and ZR 2-dimensional projections of ZeVis (which are custom views not included in the standard ROOT geometry package) have been implemented building for each 3D BAC entity the corresponding 2D projections. The resulting BAC geometry is shown in Fig. 8.7.

Visualization of BAC energy and position readouts

As a difference to with the geometry implementation, the BAC energy and position readouts are not a static information, but they need to be loaded and visualized on event-by-event basis.

Figure 8.8 shows the schematic view of a BAC pad tower. As anticipated in

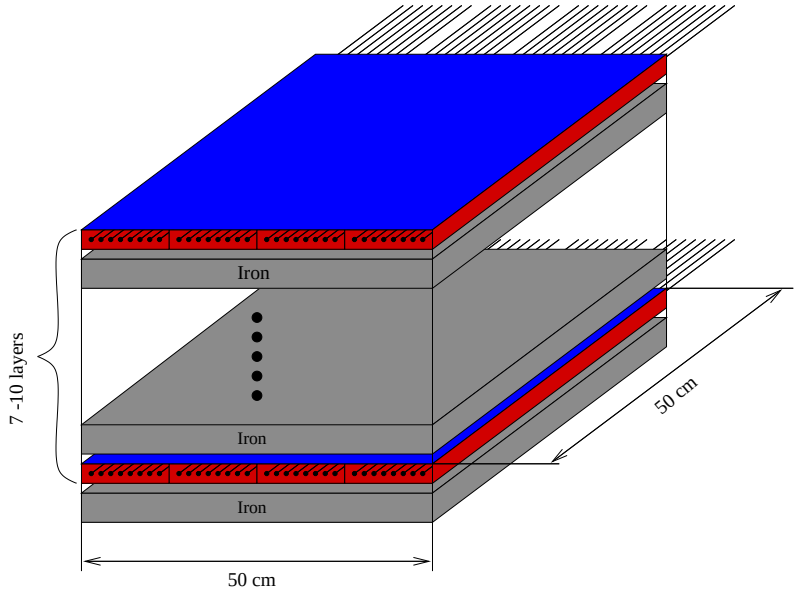

Figure 8.8: Structure of a basic BAC module.

Sec. 2.5, the BAC chambers provide both position and energy information from layer hits and pad towers, respectively. The layer hits are the signal from the wires (anodes) while the pad towers are the sums of the signals from the cathodes on top of three or four layers. These quantities can also be used for the reconstruction of the muon tracks. Different strategies have been adopted for the visualization:

Pad towers. The energy signal from the pad towers is read from the data tables and stored in arrays of pad-tower C++ objects. Each object contains its position in the 3D space, obtained from the data tables, and the energy information. A pad tower with an energy deposit is drawn in the 3D view as a 3-dimensional box with the dimension orthogonal to the pad-tower section proportional to the energy deposit. In order to show all the event information in the XY view all the energies of the pad towers having the same X and Y coordinates are summed and displayed as a bar with a height proportional to the total energy. In the ZR view the energy of pads with the same Z and R coordinate are summed. In this case the sums are re-calculated (using the information from the pad-tower objects in 3D) each time the ϕ range, which determines the R sign, is changed by the user. In Fig. 8.9 the visualization of the pad-tower energies in the XY and ZR view is shown.

Layer hits. Each BAC chamber contains 7 or 8 wires. The hit pattern of each chamber is stored in the data tables, but the position of the chambers and of

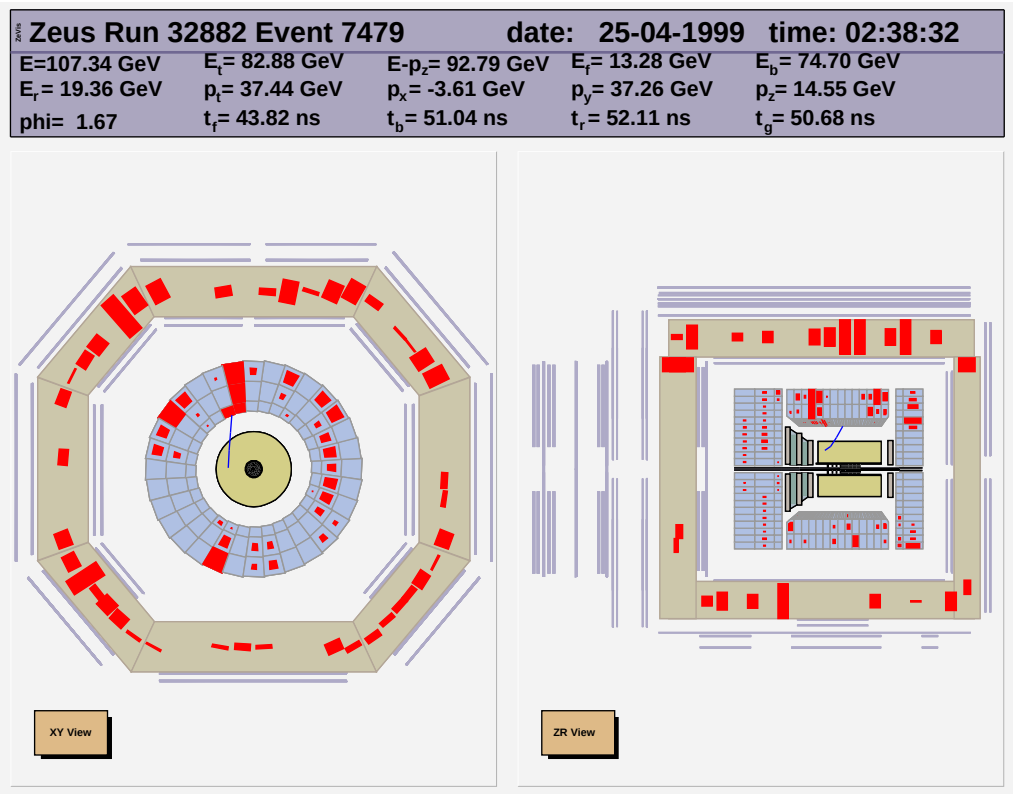

Figure 8.9: Display of pad-tower energies in the XY and ZR view. The event is, probably, a cosmic shower.

the wires has to be taken from the geometry. For this reason the position and the number of wires in each BAC chamber is loaded with the geometry file at the ZeVis start-up. If a chamber has one or more wires fired, the position of the chamber and, thus, of the wires is taken from the geometry file. Wires in the barrel BAC are typically ~ 5 meters long and run along the Z coordinate. Therefore it is not possible to reconstruct the Z coordinate of the hit from the anode signal only. Signals from adjacent anodes and cathodes form a cluster. If a wire is associated to a cluster it is possible to obtain the Z coordinate information from the pad towers associated to the same cluster. In a similar way the X coordinate can be reconstructed for wires in the forward and rear cap. As it can be seen in Fig. 8.10 the hit wires are displayed with a line as long as the length of the wires. For wires associated to a cluster the length is equal to the dimension of the corresponding pad towers.

Muon tracks. The position of the muon tracks, reconstructed from the anode and

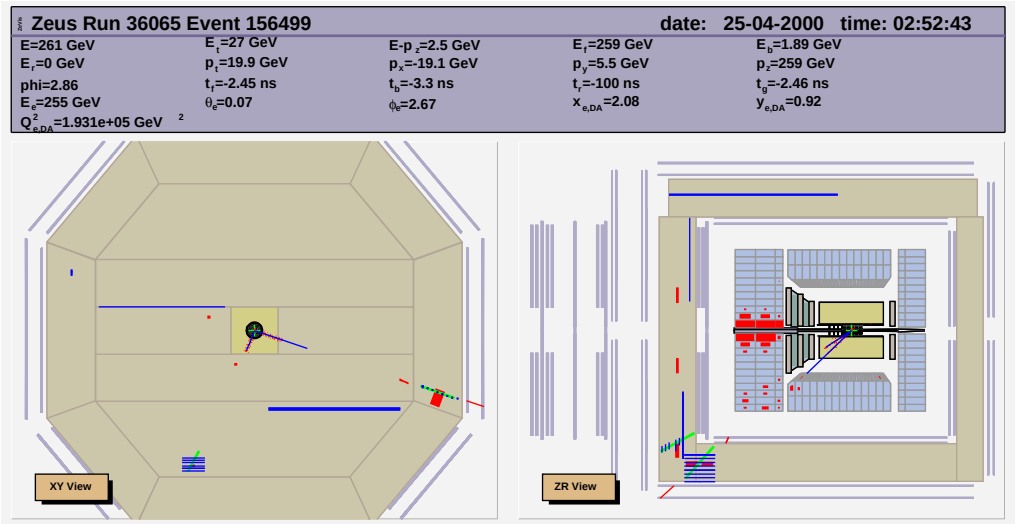

Figure 8.10: Muon pair production. The BAC hits are displayed as blue lines. In the event hits both associated and not associated to a clusters are present. In the figure it is possible to see also the reconstructed muons in the BAC (green segments).

cathode signal information, can be obtained from the data tables. The muons are visualized as a segment as shown in Fig. 8.10.

8.4 Data quality monitor for the High-Q^2 group

During the 2002–2004 data taking each physics group in ZEUS has organized a data quality monitor (DQM), in order to check the quality of the collected data. Part of this thesis work consisted in the coordination of the high-Q^2 group DQM. The aim of the DQM was to highlight as soon as possible problems related to the detectors (like noisy cells in the calorimeter), to the calibration and to the reconstruction of the data. Moreover, events of particular interest for beyond-Standard-Model searches have been selected every week without waiting for the results of dedicated and complex analyses. For these purposes, the DQM was organized in three parts:

- check of relevant variable distributions for CC and NC DIS events;
- visual scan of events selected according to several different criteria, called "Event of the week" (EOTW);
- trigger-rate check.

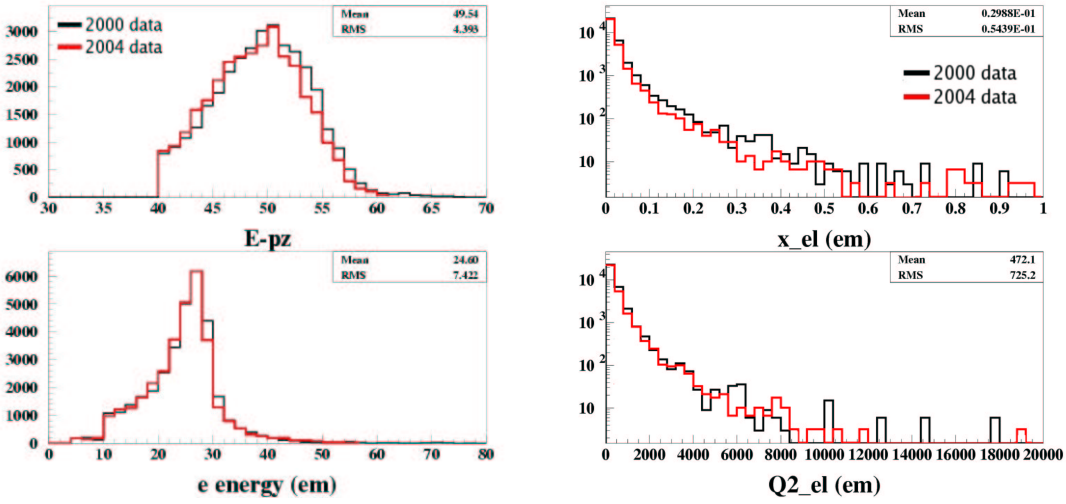

(a) (b)

Figure 8.11: (a)Comparison between 2000 and 2004 distributions for $E - P_Z$ (in GeV) and the energy of the electron (in GeV); (b) comparison between 2000 and 2004 distributions for the reconstructed x and Q^2 (in GeV^2) of the NC events.

Every week a selection of NC and CC DIS events with $Q^2 > 200\,\text{GeV}^2$ was performed on the latest reconstructed runs. Histograms with the distribution of several variables were plotted and loaded on a web page, to be compared to the corresponding distributions relative to a reference sample of runs taken in 2000. In Figs. 8.11 and 8.12 several DQM plots relative to NC DIS selection are shown. In Figs. 8.11(a) and 8.11(b) various examples of NC DIS distributions are reported for data taken in the 2004 year. For comparison the histograms are superimposed on top of the corresponding distributions from the sample of 2000 data and normalized to the number of events in the 2000 sample. The energies are not corrected for dead-material effects, and therefore the $E - P_Z$ distribution, which should peak at 55 GeV for NC DIS events, peaks at lower values as shown in Fig. 8.11(a). The uncorrected 2004 energy distributions are usually slightly shifted to lower values with respect to the 2000 distributions, because of the increased amount of dead material before the calorimeter due to the installation of the MVD. In Figure 8.12(a) the distribution of the energy of the candidate electrons within the CTD acceptance is compared to the distribution of the electrons having a matching track in the CTD, in order to monitor the central-tracking-detector track-reconstruction efficiency. In Fig. 8.12(b) the ratio between NC selected events and the integrated luminosity as a function of the

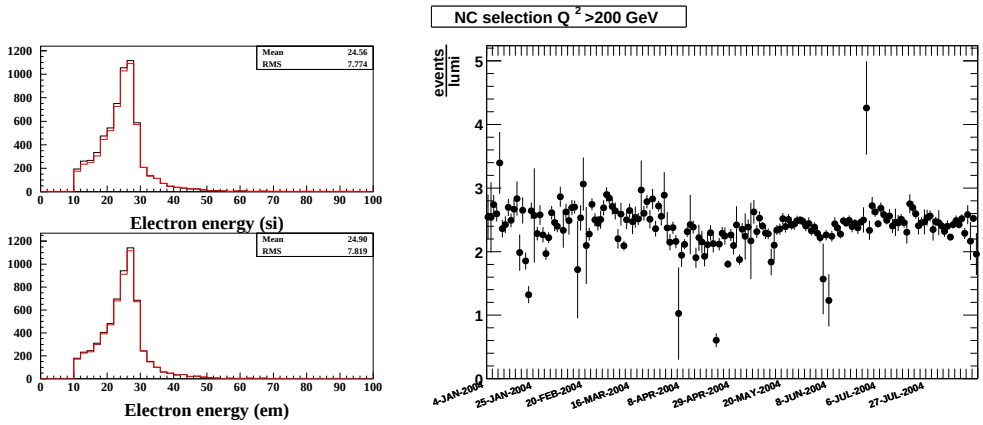

(a) (b)

Figure 8.12: (a) Distribution of the energy (in GeV) of the candidate electrons found by two different electron finders (black line) in the central tracking detector acceptance. The red line is the distribution of the energy of the electrons having a CTD track matching to the calorimeter energy deposit; (b) ratio of the number of NC DIS selected events and the corresponding luminosity as a function of the days of data taking.

days of data taking is shown. This quantity is proportional to the cross section and it should be constant during the data taking.

In the EOTW different event typologies were selected using dedicated analyses:

- high-Q^2 NC events;
- high-Q^2 CC events;
- events with two muons and high invariant di-muon mass;
- multi-electron events;
- excited electron candidates (there are beyond-SM theories in which quarks and electrons are composed by more fundamental particles [96]);
- high-E_t events;
- W boson production with $W \to e\nu_e$ or $W \to \mu\nu_\mu$ decays;
- events with two or more jets with high invariant mass;
- MSSM SUSY candidates.

The events are then visually scanned, using ZeVis, by people on shift and a selection of the most interesting ones is made. In Figs. 8.13–8.18 several interesting examples are shown.

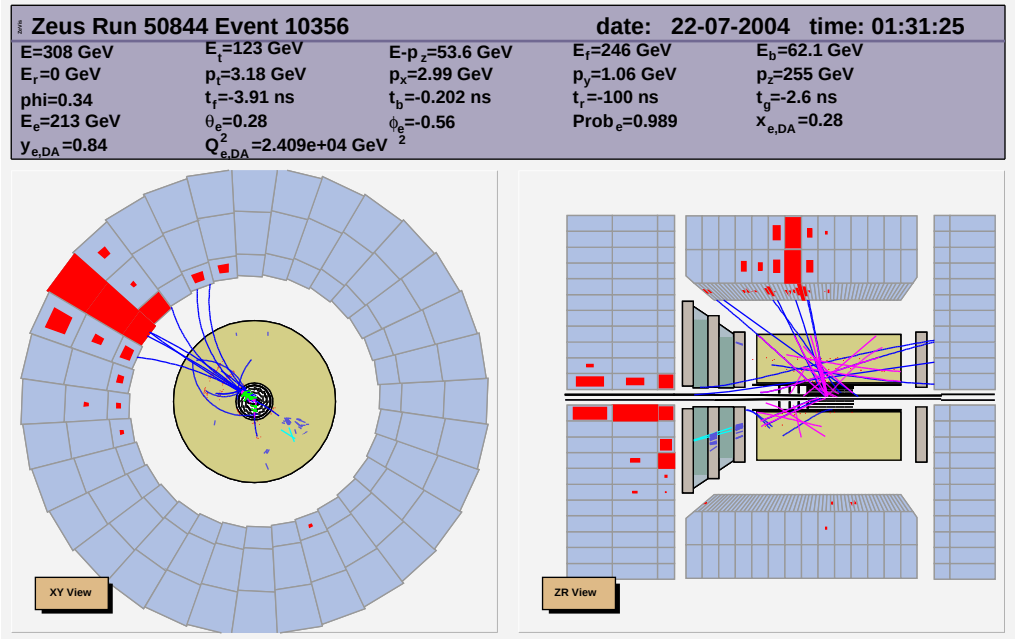

Figure 8.13: Neutral current DIS event with a reconstructed $Q^2 \sim 24000\,\mathrm{GeV}^2$.

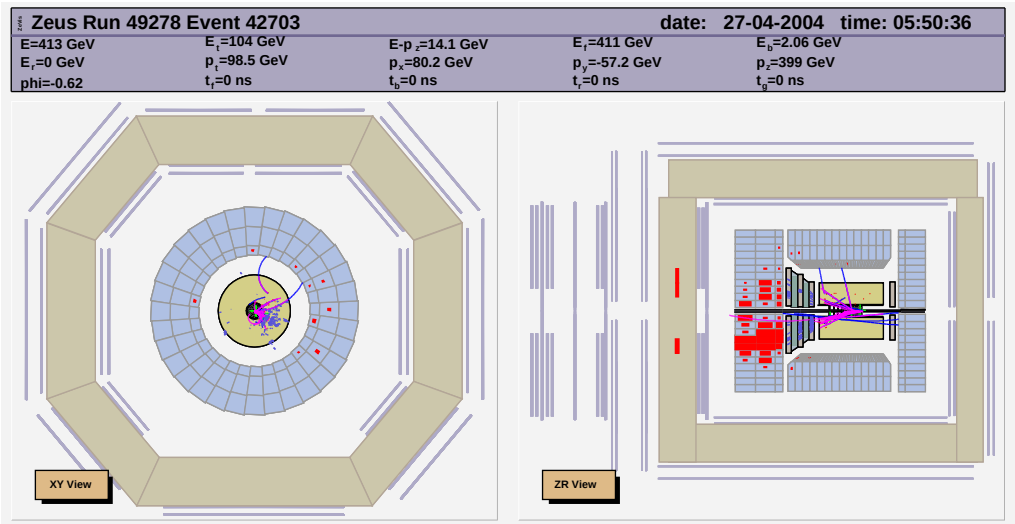

Figure 8.14: Charged current DIS event with $\not{P}_t = 98\,\mathrm{GeV}$ and a reconstructed $Q^2 \sim 18000\,\mathrm{GeV}^2$.

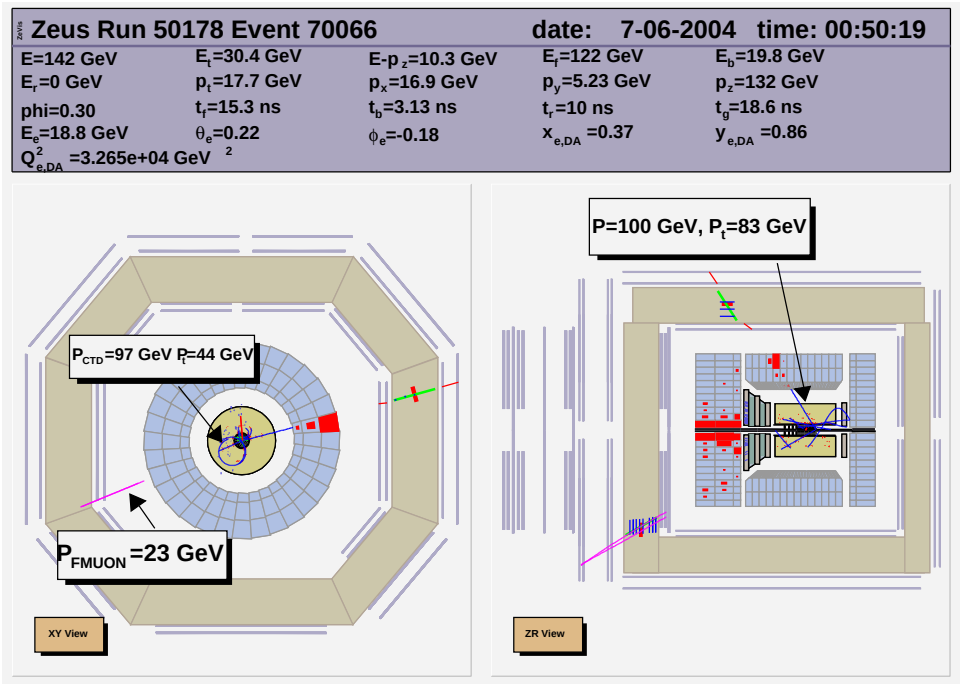

Figure 8.15: Event with two high transverse momentum muons and high invariant mass.

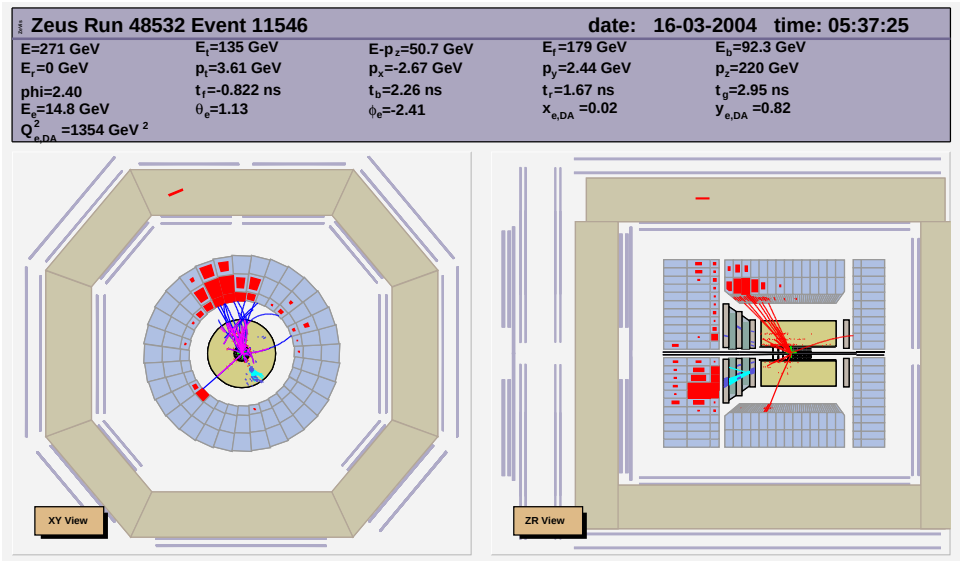

Figure 8.16: Event with two high-energy jets.

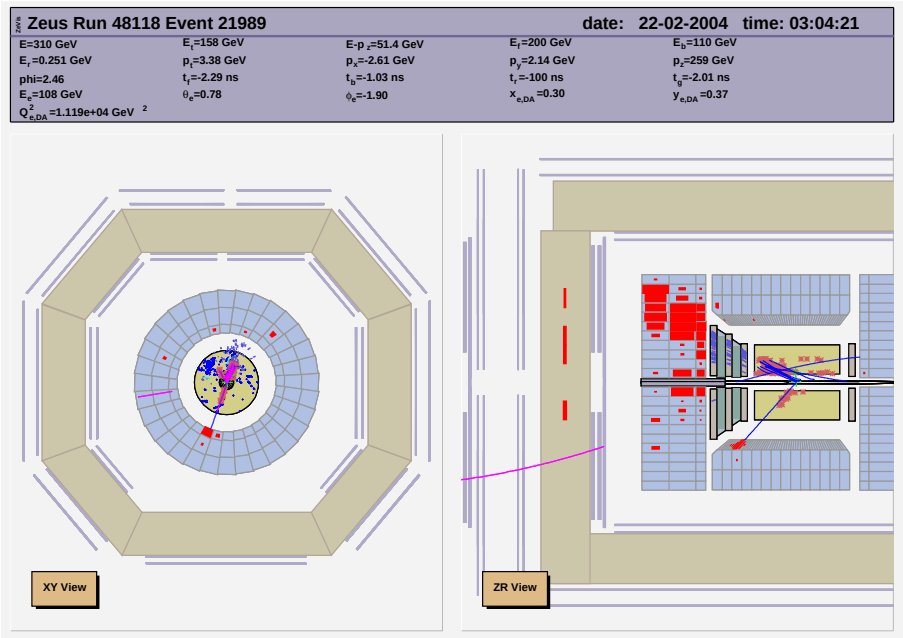

Figure 8.17: Neutral current DIS event with high transverse energy (158 GeV) and high Q^2 (11000 GeV^2).

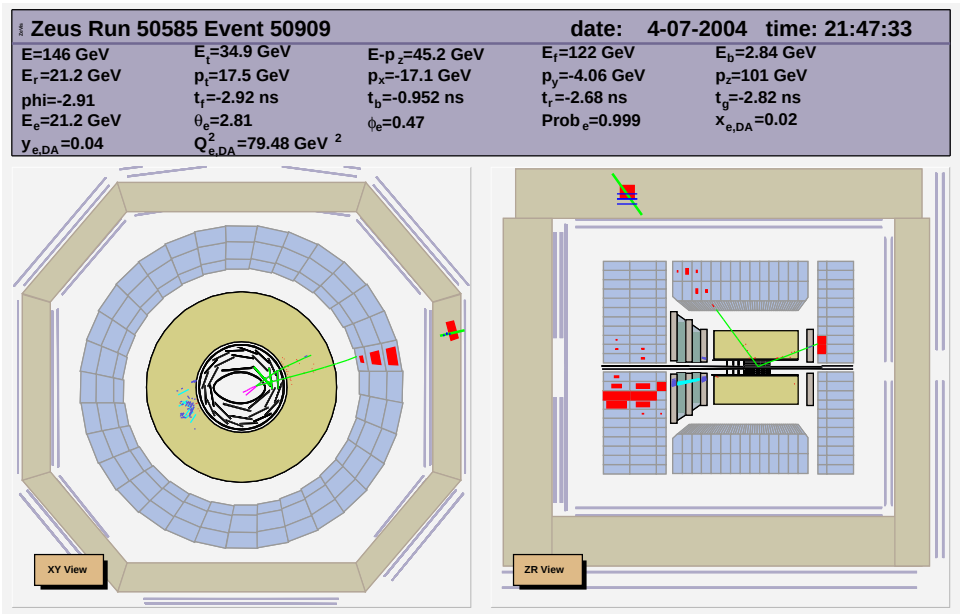

Figure 8.18: Event with an electron, a muon, a jet and missing transverse momentum.

Chapter 9

Conclusions

In this work the data taken by the ZEUS experiment at HERA in e^+p and e^-p interactions, at center-of-mass energies of 300 GeV and 318 GeV, during the years 1994–2000, corresponding to an integrated luminosity of 130 pb^{-1}, were analyzed for lepton-flavor violation. Searches for both $e-\mu$ and $e-\tau$ transitions were performed. Lepton-flavor violating interactions would have a peculiar signature at HERA therefore they could be detected with high efficiency and with a low expected background. Lepton-flavor-violating events are characterized by an isolated μ or a τ replacing the electron in the final state. Events with missing P_t and high transverse momentum leptons in the final state are possible sources of background. In the analysis neutral current and charged current deep inelastic interactions, lepton-pair production and photoproduction were taken into account in the background simulation. Lepton-flavor-violating events have been simulated in the framework of the Buchmüller-Rückl-Wyler model.

Improvements have been done with respect to the previous ZEUS analyses [91, 97]. In the $e-\mu$ transition search an optimization of the cuts was performed, while in the $e-\tau$ transition search a τ finder based on a multivariate discriminant technique was employed in order to separate QCD jets from jets due to hadronic decays of the τ. The parameters of the τ finder have been tuned for this analysis.

In the $ep \to \mu X$ processes search an isolated high-transverse-momentum muon was required. Additional cuts on the kinematics of the events and on the missing P_t were applied. In $e-\tau$ transitions all the τ decay channels were considered and they were treated separately. For $\tau \to \mu\nu_\mu\nu_\tau$ the same selection as in the $e-\mu$ case was applied since the event topologies are very similar. In the $\tau \to e\nu_e\nu_\tau$ channel a high-energy electron aligned in the transverse plane with the $\not{P}_t$-vector direction was required. In the hadronic τ-decay channel the events with a τ-jet candidate in the $\not{P}_t$-vector direction with high value of the discriminant were selected.

No evidence of lepton-flavor-violating interactions was found. The Buchmüller-

Rückl-Wyler leptoquark (LQ) model, with LQ of any mass coupling to different lepton generations, has been used to give a quantitative description of the results. For leptoquark masses lower than the HERA center-of-mass energy, limits at 95% C.L. were set on the LQ coupling $\lambda_{eq_1}\sqrt{\beta_{\ell q}}$ as a function of the mass, using the narrow-width approximation for the cross section. For a coupling constant of electromagnetic strength ($\lambda_{eq_1} = \lambda_{\ell q_\beta} = 0.3$), mass limits between 257 and 299 GeV were set, depending on the leptoquark type. For $M_{\mathrm{LQ}} = 250\,\mathrm{GeV}$, upper limits on $\lambda_{eq_1}\sqrt{\beta_{\mu q}}$ ($\lambda_{eq_1}\sqrt{\beta_{\tau q}}$) in the range $0.010-0.12$ ($0.013-0.15$) were set.

For LQs with $M_{\mathrm{LQ}} \gg \sqrt{s}$, upper limits on $\lambda_{eq_\alpha}\lambda_{\mu q_\beta}/M^2_{\mathrm{LQ}}$ and $\lambda_{eq_\alpha}\lambda_{\tau q_\beta}/M^2_{\mathrm{LQ}}$ were calculated for all combinations of initial- and final-state quark generations. In this case the calculation of the LQ cross section was performed using a contact-interaction approximation.

Next-to-leading-order corrections to the LQ cross section were applied when the theoretical calculation was available (scalar low-mass LQs). All the calculated cross sections were corrected for initial-state QED radiation effects. Systematic uncertainties were taken into account and included in the limit calculation using a Bayesian approach.

Some of the obtained limits for the LQ coupling also apply to R-Parity violating squarks. In many cases, especially for the $e-\tau$ transition, ZEUS limits are more stringent than any other limit published to date.

The results obtained in this work have been presented to various conferences [98, 99, 18, 100, 93, 101, 102] and will soon appear on two papers to be published [103, 104].

Appendix A

Search for high-invariant-mass multi-muon events

Within this thesis work a search of multi-muon events in 1997–2000 data, corresponding to an integrated luminosity of 104.0 ± 1.5 pb^{-1}, has been performed using the first muon finder described in Sec. 4.4. This search was motivated by the excess of events with two or three electrons with high invariant mass ($M > 100$ GeV) found by H1 and described in Sec. 1.2.3. One possible explanation of such excess is the production and the subsequent decay of a heavy particle. If the heavy particle decays into lepton pairs, discrepancies from the SM could be found also in the muon pair production.

The trigger used in this analysis was based on the barrel and rear muon chamber trigger. A cut on the calorimeter timing (as described in Sec. 5.1) was applied in order to reject the huge background due to cosmic muons. Moreover, the reconstructed vertex was required to have $|Z| < 40$ cm and $R = \sqrt{X^2 + Y^2} < 0.5$ cm. The background from halo muons was suppressed excluding the events with energy deposits in the calorimeter aligned with the Z coordinate. In order to reduce the background from proton beam-gas interactions, a cut on the quality of the tracks (described in Sec. 5.1) was applied. The final selection of high invariant mass multi-muon events required:

- at least two muons in the polar-angle range $20^\circ < \theta < 160^\circ$ with transverse momentum – measured from the CTD tracks – above 5 GeV; the polar angle region was chosen to ensure a good reconstruction of the tracks; in addition the muon tracks were required to cross at least three CTD superlayers;
- $D_{\text{trk}} > 1$ (see Sec. 5.2), to select only well isolated muons;
- $M_{\mu\mu} > 5$ GeV, where $M_{\mu\mu}$ is the invariant mass of the two muons with highest momentum;

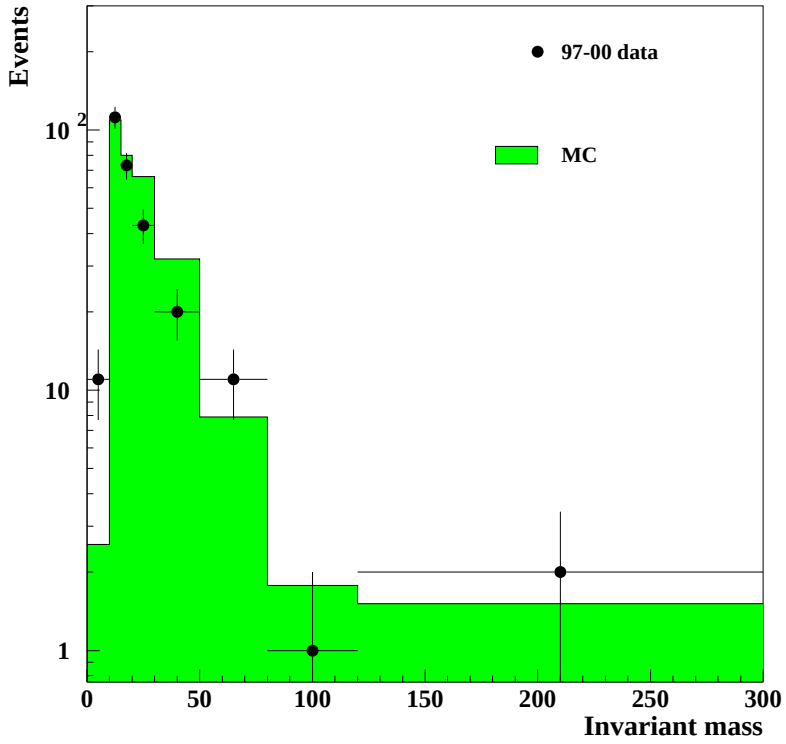

Figure A.1: Invariant mass distribution of the di-muons. The histogram binning has been chosen according to the invariant mass resolution.

- $\cos\Omega > -0.996$, where Ω is the opening angle of the two muons.

After the selection 273 events were found in data while 301 ± 3 were expected from the SM Monte Carlo. No event with more than two muons was found in data. In Fig. A.1 the invariant mass distribution of the di-muon events is shown. The MC expectation is normalized to the luminosity of data. The efficiency of the BMUON trigger, which is not included in the detector simulation, was taken into account. The MC used to simulate 1998–2000 data was GRAPE (Tables 3.4 and 3.5), while muon pair production for 1997 was simulated using LPAIR.

Two events with $M_{\mu\mu} > 100\,\text{GeV}$ were found in data in agreement with the SM expectation of 2.3 ± 0.3. The two events are shown in Figs. A.2 and A.3.

These results have been included in a conference presentation and a contributed paper [18].

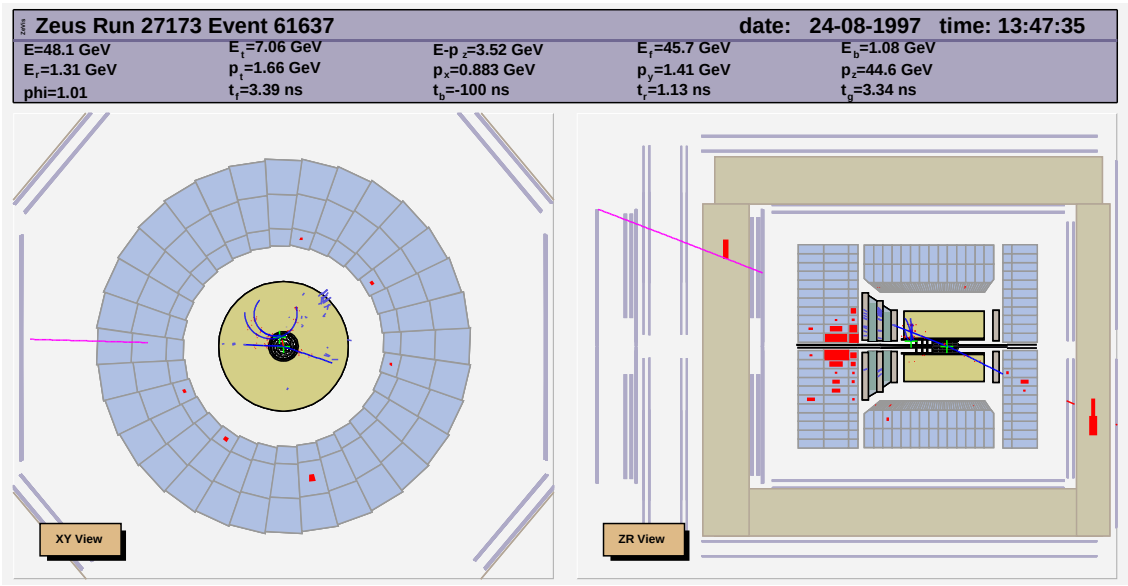

Figure A.2: Di-muon event with high invariant mass ($M_{\mu\mu} = 270\,\text{GeV}$)

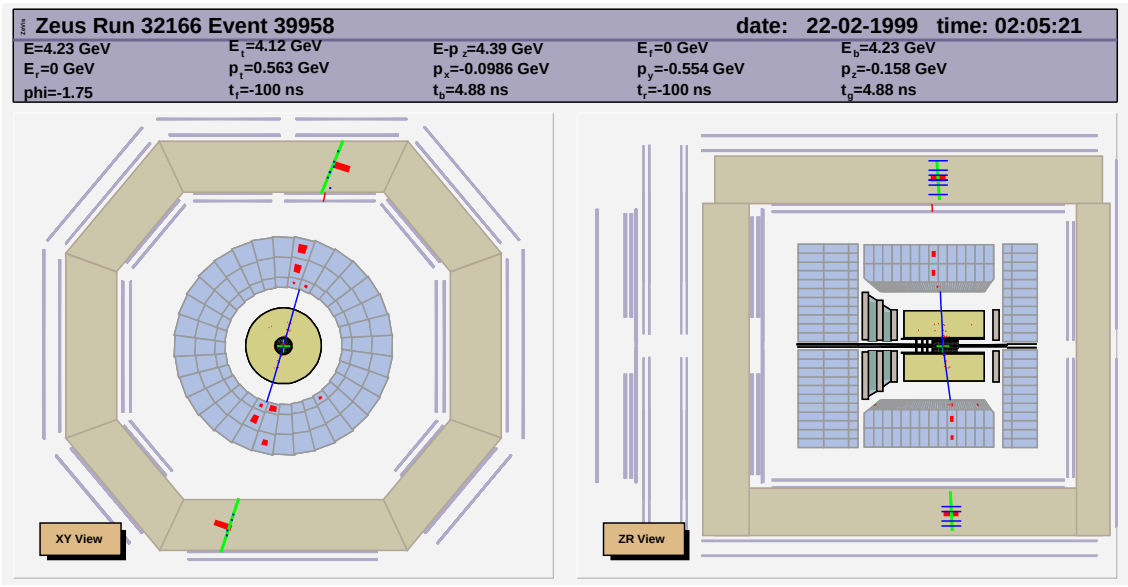

Figure A.3: Di-muon event with high invariant mass ($M_{\mu\mu} = 200\,\text{GeV}$)

Appendix B

DST bit definition

In this appendix the trigger logic used for the selection of LFV events (both $e-\mu$ and $e-\tau$ transitions) is described. Events were accepted if the DST bits 10 and 34 were fired.

DST10. This bit requires at least one vertex correctly reconstructed from the CTD tracks;

DST34. This bit is used to select CC DIS events or events with high $\not{P}_t$. The events are accepted if all the following conditions are fulfilled:

- ExoTLT(2) OR ExoTLT(6)OR $P_t^{\mathrm{ex1IR}} > 6\,\mathrm{GeV}$, where P_t^{ex1IR} is the missing momentum measured in the calorimeter cells that are not in the inner ring of FCAL;
- $\not{P}_t > 7\,\mathrm{GeV}$;
- Events that satisfy the following conditions are rejected to suppress the background from proton beam-gas events:
  * NOT (ExoTLT(2))
  * $P_t^{\mathrm{ex1IR}} < 10\,\mathrm{GeV}$
  * $\not{P}_t < 25\,\mathrm{GeV}$
  * $\not{P}_t/E_t < 0.7$
  * $E - P_Z < 10\,\mathrm{GeV}$
  * $\not{P}_t/P_Z < 0.08$
  * $P_X < 0\,\mathrm{GeV}$
  * $|P_Y| < 4\,\mathrm{GeV}$

The ExoTLT is a branch of the third level trigger and the ExoTLT(2) and ExoTLT(6) bits, which are designed to select CC events, are defined by:

ExoTLT(2). All the following conditions have to be satisfied:

- $\not{P}_t > 6\,\mathrm{GeV}$;
- at least one good track ($p_t^{\mathrm{trk}} > 0.5\,\mathrm{GeV}$ and pointing to the interaction vertex);
- good reconstructed vertex ($|Z| < 60$ cm AND $R = \sqrt{X^2 + Y^2} < 10$ cm);
- $|t_u - t_d| < 8$ ns, where t_u and t_d are the global timing of the upper and lower part of the calorimeter; this cut is introduced to exclude the background from cosmic muons and showers.

ExoTLT(6). This bit is fired if the event fulfills all these conditions:

- $\not{P}_t > 8\,\mathrm{GeV}$;
- EXOSLT(4) fired;
- $E_{\mathrm{FCAL}} > 10\,\mathrm{GeV}$ or a good reconstructed track from FLT, $N^{\mathrm{FLT}}_{\mathrm{goodtrk}}$ (the projection of the CTD hits to the Z direction has to point to the interaction vertex);
- events with more than 5 tracks must not have a vertex with $Z < -80$ cm, in order to reject proton beam-gas interactions;
- (number of CTD hits < 2500) OR ($P_t^{\mathrm{ex1IR}} > 10\,\mathrm{GeV}$);
- $|t_u - t_d| < 8$ ns.

The EXOSLT(4) is the second level trigger bit dedicated to CC events and it is defined by requiring an AND of the following conditions:

- $|t_g| < 7$ ns where t_g is the calorimeter global timing;
- ($\not{P}_t > 6\,\mathrm{GeV}$ AND $E_t^{\mathrm{ex1IR}} > 6\,\mathrm{GeV}$ AND $N^{\mathrm{FLT}}_{\mathrm{goodtrk}} \geq 1$) OR
  ($\not{P}_t > 9\,\mathrm{GeV}$ AND $P_t^{\mathrm{ex1IR}} > 8\,\mathrm{GeV}$ AND $E_{\mathrm{FCAL}} > 20\,\mathrm{GeV}$) OR
  ($\not{P}_t > 9\,\mathrm{GeV}$ AND $\not{P}_t/\sqrt{E_t} > 2.1\,\mathrm{GeV}^{1/2}$ AND $E_{\mathrm{FCAL}} > 80\,\mathrm{GeV}$).

Bibliography

[1] H1 Coll. V. Andreev *et al.*, Phys. Lett. **B 561** (2003) 241.

[2] ZEUS Coll.S. Chekanov *et al.*, Phys. Lett. **B 583** (2004) 41.

[3] H1 Coll. A. Aktas *et al.*, Eur. Phys. J. **C 31** (2003) 17.

[4] E.D. Bloom *et al.*, Phys. Rev. Lett. **23**, (1969) 930;
M. Breidenbach *et al.*, Phys. Rev. Lett. **23**, (1969) 935.

[5] J.D. Bjorken, Phys. Rev. **179**, (1969) 1547.

[6] R.P. Feynmann, *Photon–Hadron Interactions*, W.A. Benjamin (1972).

[7] M. Gell–Mann, Phys. Lett. **8**, (1964) 214.

[8] J.C. Collins, D.E. Soper and G. Sterman, Nucl. Phys. **B 261**, (1985) 104.

[9] V.N. Gribov and L.N. Lipatov, Sov. J. Nucl. Phys. **15** (1972) 438;
G. Altarelli and G. Parisi, Nucl. Phys. **B 126** (1977) 298;
Y.L. Dokshitzer, Sov. Phys. JETP **46** (1977) 641.

[10] ZEUS Coll., abstract 5-0263, submitted to the ICHEP04 conference, Beijing, China, August 2004.

[11] J. Pumplin, D.R. Stump, J. Huston, H.L. Lai, P. Nadolsky and W.K. Tung, JHEP **0207**, (2002) 012.

[12] A.D. Martin, R.G. Roberts, W.J. Stirling and R.S. Thorne, Eur. Phys. J. **C 28**, (2003) 455.

[13] ZEUS Coll., abstract 4-0256, submitted to the ICHEP04 conference, Beijing, China, August 2004;
H1 Coll., abstract 4-0756, submitted to the ICHEP04 conference, Beijing, China, August 2004.

[14] H. Bethe and W. Heitler, Proc. Roy. Soc. Lond. **A 146** (1934) 83;
L.D. Landau and E. Lifshitz, Physikalishe Zeitschrift der Sowjetunion **6** (1934) 244.

[15] U. Baur, J. Vermaseren and D. Zeppenfeld, Nucl. Phys. **325** (1989) 253;
U. Baur, J. Vermaseren and D. Zeppenfeld, Nucl. Phys. **375** (1992) 3.

[16] ZEUS Coll., Phys. Lett. **B 559** (2003) 153, addendum: DESY-03-188 (2003).

[17] H1 Coll., abstract 188 submitted to the ICHEP04 conference, Beijing, China, August 2004.

[18] ZEUS Coll., abstract 910 submitted to the ICHEP02 conference, Amsterdam, The Netherlands, July 2002.

[19] H1 Coll. A. Aktas *et al.*, Eur. Phys. J. **C 33** (2004) 9.

[20] H1 Coll. A. Aktas *et al.*, Phys. Lett. **B 583** (2004) 28.

[21] ZEUS Coll., abstract 230 submitted to the ICHEP04 conference, Beijing, China, August 2004.

[22] H1 Coll., abstract 104 submitted to the EPS03 conference, Aachen, Germany, July 2003.

[23] Q.R. Ahmad *et al.* SNO Coll., Phys. Rev. Lett. **87** (2001) 071301.

[24] S. Fukuda *et al.* Super-Kamiokande Coll., Phys. Rev. Lett. **85** (2000) 3999.

[25] J.I. Illana and M. Masip, Acta Phys. Polon. **B 34**, (2003) 5413.

[26] H.B. Nilles, Phys. Rep. **110** (1984) 1;
H.E. Haber and G.L. Kane, Phys. Rep. **117**, (1985) 75.

[27] C. Pati and A. Salam Phys. Rev. **D 10**, (1974) 275;
H. Georgi, S.L. Glashow, Phys. Rev. Lett. **32** (1974) 438;
P. Langacker, Phys. Rep. **72**, (1981) 185.

[28] B.T. Cleveland *et al.*, Astrophys. J. **496** (1998) 505.

[29] KAMIOKANDE-II Coll. K.S. Hirata *et al.*, Phys. Rev. Lett. **65** (1990) 1297;
Kamiokande-II Coll. K.S. Hirata *et al.*, Phys. Rev. **D 44** (1991) 2241. Erratum-ibid. **D 45** (1992) 2170;
Kamiokande Coll. Y. Fukuda *et al.*, Phys. Rev. Lett. **77** (1996) 1683.

[30] J.N. Abdurashitov *et al.* SAGE Coll., Phys. Rev. **C 60** (1999) 055801.

[31] GALLEX Coll. W. Hampel *et al.*, Phys. Lett. **B 447** (1999) 127.

[32] Super-Kamiokande Coll. S. Fukuda *et al.*, Phys. Rev. Lett. **86** (2001) 5651.

[33] GNO Coll. M. Altmann *et al.*, Phys. Lett. **B 490**, (2000) 16.

[34] J.N. Bahcall, M.H. Pinsonneault and S. Basu, Astrophys. J. **555**, (2001) 990.

[35] A.S. Brun, S. Turck-Chieze and J.P. Zahn, Astrophys. J. **525**, (1999) 1032.

[36] SNO Coll. Q.R. Ahmad *et al.*, Phys. Rev. Lett. **89** (2002) 011301.

[37] R.N. Mohapatra and G. Senjanovic, Phys. Rev. Lett. **44** (1980) 912.

[38] G. Jungman, M. Kamionkowski and K. Griest, Phys. Rept. **267**, (1996) 195.

[39] V.D. Barger, G.F. Giudice and T. Han, Phys. Rev. **D 40**, (1989) 2987.

[40] W. Buchmüller, R. Rückl and D. Wyler, Phys. Lett. **B 191**, (1987) 442. Erratum in Phys.Lett. **B 448**, (1999) 320.

[41] B. Schrempp, *Physics at HERA*, proceedings of the workshop **2**, (1991) 1034.

[42] ZEUS Coll., *The ZEUS Detector, Status Report 1993* (unpublished), DESY (1993) available on `http://giroz.desy.de/bluebook/bluebook.html`.

[43] N. Harnew *et al.*, Nucl. Inst. Meth. **A 279**, (1989) 290;
B. Foster *et al.*, Nucl. Phys. Proc. Suppl. **B 32**, (1993) 181;
B. Foster *et al.*, Nucl. Inst. Meth. **A 338**, (1994) 254.

[44] M. Derrick *et al.*, Nucl. Inst. Meth. **A 309**, (1991) 77;
A. Andresen *et al.*, Nucl. Inst. Meth. **A 309**, (1991) 101;
A. Caldwell *et al.*, Nucl. Inst. Meth. **A 321**, (1992) 356;
A. Bernstein *et al.*, Nucl. Inst. Meth. **A 336**, (1993) 23.

[45] G. Abbiendi *et al.*, Nucl. Instrum. Meth. A **333**, (1993) 342.

[46] W.H. Smith *et al.*, Nucl. Instrum. Meth. A **355**, (1995) 278.

[47] B. Andersson *et al.*, Z. Phys., **C 43**, (1989) 625.

[48] B. Andersson *et al.*, Phys. Rep., **97**, (1983) 31.

[49] R.D. Field and S. Wolfram, Nucl. Phys. **B 213**, (1983) 65;
B.R. Webber, Nucl. Phys. **B 238**, (1984) 492.

[50] L. Bellagamba, Comput. Phys. Commun. **141**, (2001) 83.

[51] T. Sjöstrand, Comp. Phys. Comm. **82**, (1994) 74.

[52] G. Marchesini*et al.*, Comp. Phys. Comm. **67**, (1992) 465.

[53] H.L. Lai *et al.*, Phys. Rev. **D 55**, (1997) 1280.

[54] M. Gluck, E. Reya and A. Vogt, Phys. Rev. **D 46**, (1992) 1973.

[55] G. Ingelman, A. Edin and J. Rathsman, Comp. Phys. Comm. **101**, (1997) 108;

[56] A. Kwiatkowski, H. Spiesberger and H.J. Möhring, Comp. Phys. Comm. **69**, (1992) 155.

[57] H. Spiesberger, *An Event Generator for ep Interactions at HERA Including Radiative Processes (Version 4.6)*, 1996, available on `http://www.desy.de/~hspiesb/heracles.html`.

[58] H. Spiesberger, HERACLES *and* DJANGOH*: Event Generation for ep Interactions at HERA Including Radiative Processes*, 1998, available on `http://www.desy.de/~hspiesb/djangoh.html`.

[59] L. Lönnblad, Comput. Phys. Commun. **71**,(1992) 15.

[60] T. Sjøstrand, Comput. Phys. Commun. **39**, (1986) 347; T. Sjøstrand and M. Bengtsson, Comput. Phys. Commun. **43**, (1987) 367; T. Sjøstrand, Comput. Phys. Commun. **82**, (1994) 74.

[61] T. Abe, Comput. Phys. Commun. **136**, (2001) 126.

[62] CTEQ Coll. H.L. Lai *et al.*, Eur. Phys. J. **C 12**, (2000) 375.

[63] R. Brun *et al., GEANT 3.13*, CERN DD/EE/84-1 (1987).

[64] S.M. Fisher and P. Palazzi, *ADAMO Programmers Manual–Version 3.2*. CERN ECP and RAL, available on `http://adamo.web.cern.ch/Adamo/`

[65] G.F. Hartner, *VCTRAK (3.07/04): Offline Output Information* (unpublished). ZEUS-97-064, Internal ZEUS note, 1997;
G.F. Hartner, *VCTRAK Briefing: Program and Math* (unpublished). ZEUS-97-064, Internal ZEUS note, 1997.

[66] ZEUS Coll. J. Breitweg *et al.*, Eur. Phys. J. **C 11** (1999) 427.

[67] S. Catani *et al.*, Nucl. Phys. **B 406**, (1993) 187;
S.D. Ellis and D.E. Soper, Phys. Rev. **D 48**, (1993) 3160;
M.H. Seymour, Nucl. Phys. **B 513**, (1998) 269.

[68] O. Gonzalez, PhD Thesis, Univ. of Madrid, Madrid (Spain), Report DESY-THESIS-2002-020, 2002;
O. Gonzalez, H. Raach and J. Terron, *Measurements of the inclusive jet cross section in NC DIS in the Breit Frame* (unpublished) ZEUS-02-007, Internal ZEUS note, 2002;
M. Vazquez Acosta, PhD Thesis, Univ. of Madrid, Madrid (Spain), Report DESY-THESIS-2003-006, 2003.

[69] J.R. Forshaw and M.H. Seymour, JHEP **9909**, (1999) 009.

[70] M.H. Seymour, Nucl. Phys. **B 421**, (1994) 545.

[71] C.N. Nguyen. Diploma Thesis, Universität Hamburg, Hamburg, Germany, Report DESY-THESIS-2002-024, 2002.

[72] T. Carli and B. Koblitz. *Proceedings of the VII International Workshop on Advanced Computing and Analysis Techniques in Physics Research*, P. Bath and M. Kasemann (ed.), American Institute of Physics (2000) 110. Also in hep-ph/0011224, 2000.

[73] T. Carli and B. Koblitz, Nucl. Inst. Meth. **A 501**, (2003) 576.

[74] J.F. Grivaz and F. Le Diberder, LAL-92-37.

[75] M. Corradi, *Proceedings of the Workshop on Confidence Limits*, F. James, L. Lyons, Y. Perrin (ed.), Geneva, Switzerland, CERN (2000) 237. Also in preprint CERN 2000-005, available on `http://cern.web.cern.ch/CERN/Divisions/EP/Events/CLW/PAPERS/PS/corradi.ps`;
G. D'Agostini, *Probability and measurement uncertainty in physics: a bayesian primer.* DESY 95–242.

[76] C.F. Weizsäcker, Z. Phys.,**88**, (1934) 612;
E.J. Williams, Phys. Rev.,**45** (1934) 729.

[77] T. Plehn, H. Spiesberger, M. Spira and P.M. Zerwas, Z. Phys. **C 74**, (1997) 611.

[78] D. Stump *et al.*, JHEP **0310**, (2003) 046.

[79] S. Davidson, D. Bailey and B.A. Campbell, Z. Phys. **C 61**, (1994) 613.

[80] E. Gabrielli, Phys. Rev. **D 62**, (2000) 055009.

[81] Particle Data Group, K. Hagiwara *et al.*, Phys. Rev. **D 66**, (2002) 010001.

[82] M. Herz. Diploma Thesis, Universität Bonn, Bonn, Germany, Report hep-ph/0301079, 2002.

[83] Babar Coll., B. Aubert *et al.*, Phys. Rev. Lett. **92**, (2004) 121801.

[84] Belle Coll., Y. Yusa *et al.*, Phys. Lett. **B 589**, (2004) 103.

[85] CLEO Coll, A. Bornheim *et al.*, Phys. Rev. Lett. **93**, (2004) 241802.

[86] J. Butterworth and H. Dreiner, Nucl. Phys. **B 397**, (1993) 3.

[87] CDF Coll., F. Abe *et al.*, Phys. Rev. Lett. **81**, (1998) 4806.

[88] DØ Coll., B. Abbott *et al.*, Phys. Rev. Lett. **84**, (2000) 2088.

[89] CDF Coll., D. Acosta *et al.*, Phys. Rev. Lett. **91**, (2003) 17160.

[90] H1 Coll, C. Adloff *et al.*, Eur. Phys. J. **C 11**, (1999) 447. Erratum in Eur. Phys. J. **C 14**, (2000) 553.

[91] ZEUS Coll., S. Chekanov *et al.*, Phys. Rev. **D 65**, (2002) 92004.

[92] ZEUS Coll., *A microvertex Detector for ZEUS* (unpublished). ZEUS-97-006, Internal ZEUS note, 1997, DESY-PRC 97/01.

[93] O. Kind, C. Genta, O. Gutsche, R. Mankel *et al.*, eConf **C0303241**, MOLT002 (2003).

[94] The ROOT analysis framework, web page: `http://root.cern.ch`.

[95] L.A.T. Bauerdick, A. Fox-Murphy, T.M. Haas, S. Stonjek and E. Tassi, Comput. Phys. Commun. **137**, (2001) 236;
U. Fricke, *Upgrade of the ZEUS OO Tag Database for Physics Analysis at HERA*, Proceedings of the CHEP01 Conference, Beijing 2001, 252.

[96] B. Schrempp and F. Schrempp, Phys. Lett. **B 153**, (1985) 101;
J. Wudka, Phys. Lett. **B 167**, (1986) 337.

[97] ZEUS Coll., M. Derrick *et al.*, Z. Phys. **C 73**, (1997) 613.

[98] C. Genta for the H1 and ZEUS Collaborations, Acta Phys. Polon. **B 33**, (2002) 3905.

[99] ZEUS Coll., abstract 906 submitted to the ICHEP02 conference, Amsterdam, The Netherlands, July 2002.

[100] ZEUS Coll., abstract 498 submitted to the EPS03 conference, Aachen, Germany, July 2003.

[101] ZEUS Coll., abstract 255 submitted to the ICHEP04 conference, Beijing, China, August 2004.

[102] C. Genta for the H1 and ZEUS Collaborations, to appear in the proceedings of 10th International Symposium on Particles, Strings and Cosmology (PASCOS 04 and Pran Nath Fest), Boston, Massachusetts, August 2004.

[103] L. Bellagamba, G. Barbagli, C. Genta *Lepton Flavor Violation at HERA*, accepted by Progress in Experimental High Energy Physics Research, Nova Science Publishers, Happauge, NY (USA).

[104] ZEUS Coll., S. Chekanov *et al.*, DESY 05-016, (2005), submitted to the Eur. Phys. J.